An investigation of the imaging performance of CCD based x-ray detectors for digital mammography

Ian Ho

University College London

Submitted for

The Degree of Doctor of Philosophy

University Of London

April 1996

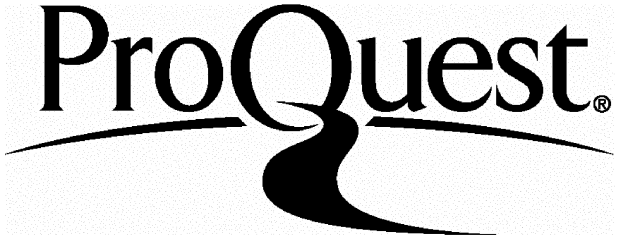

Abstract

This thesis describes the imaging performance of a prototype digital mammography system based upon charge coupled devices (CCDs). The imaging performance of these detectors is dependent upon the configuration of the detector. In this thesis the performance of 14 different detector configurations are studied for use in digital mammography.

Experimental evaluations of factors which affect the performance of imaging systems such as quantum detection efficiency, dynamic range, modulation transfer function (MTF(f)) and Noise power spectrum (NPS) were performed. The use of spatial frequency dependent detective quantum efficiency DQE(f) to characterise the detectors in terms of signal to noise ratio transfer is described.

It is shown that direct interactions of x-rays in the CCD act to reduce DQE(f) at high spatial frequencies and severely impair the detectors ability to detect small objects (250μm in diameter). The use of a sufficient thickness of fibre optic faceplate to couple the phosphor layer to the CCD is shown to remove these interactions and shows a corresponding increase in DQE(f) (at higher spatial frequencies) and the detector's ability to image smaller objects

A subjective comparison of images of a breast phantom shows that images of superior quality were obtained with the prototype system compared with images produced using a conventional film-screen system, for a slight increase in dose. Improvements to the system and detector design are presented and will act to try to produce the same image quality for equivalent doses used in conventional mammography.

Contents

Contents

Contents

Contents

Contents

Figures

Chapter 1

Chapter 2

Chapter 3

Figures

Chapter 4

Figures

Figures

Chapter 5

Figures

Chapter 6

Tables

Chapter 2

Chapter 3

Chapter 4

Chapter 5

Acknowledgements

I would like to thank all my supervisors for their advice and support during this project. A big thank you also goes out to all my colleagues at Medical Physics, UCL and SIRA for their help and friendship.

Special thanks goes to Fiona for everything.

Finally I would like to thank The EPSRC for funding me over the last three years

CHAPTER 1

1. Introduction

Cancer of the breast causes 15000 deaths each year in the UK. There are 24000 new cases of breast cancer each year making it the most common form of cancer to affect females in the UK. A number of controlled trials have shown that breast cancer screening reduces breast cancer mortality rates. Currently it is recommended that women between the ages of 50 and 64 years of age attend breast screening every three years.

Mammography is currently the most sensitive technique for the detection of early breast cancer, and film screen imaging is the most common mammographic technique used. However there exists several fundamental limitations on the quality of images produced from film-screen imaging. Yaffe and Nishikawa(1988) have shown that the replacement of the film-screen combination with a CCD based detector system can overcome these limitations. Recent research has shown that a CCD based digital mammography system can produce images of comparable quality to those obtained with conventional film screen systems (Maidment et al 1993).

The quality of images produced from a detector is strongly dependent upon factors such as x-ray sensitivity, dynamic range and signal and noise transfer characteristics. This thesis is an investigation into the effect these factors have upon the image quality. The thesis also includes prescriptions for improving the design of detectors for use in digital mammography systems. The first chapter includes a description of mammographic precursors to breast cancer , a review of conventional film-screen

mammography and the limitations involved. The advantages of using digital detectors are discussed The design, and theory of operation is then discussed.

Chapter 2 details the design and construction of a prototype CCD based digital imaging system and chapter3 concerns the initial testing and calibration of this system. The signal and noise transfer characteristics of the available detectors are evaluated in chapter 4. Chapter 5 discusses the use of the system for mammography and includes quantitative analysis of breast phantom images obtained with the detectors. Chapter 6 presents conclusions and some suggestions for future work. The final chapter describes the use of the imaging system for microtomography and its merits are compared with other systems available.

1.1 Conventional mammography

Around 60-80% of breast carcinomas have associated with them small deposits of calcium hydroxyapetite or calcium phosphate known as microcalcifications (Sickles 1982). Biopsy studies have shown that conventional film-screen mammography only detects 30-50% of microcalcifications present. Analysis of the size number and distribution of the detected microcalcifcations can lead to a high level of diagnostic accuracy.

The risk of radiation induced carcinogenisis in mammography is a prime concern. State of the art mammography systems are designed to minimise patient dose whilst providing highest quality images. Figure 1.1 shows a schematic diagram of a conventional mammography system. It consists of

- X-ray tube- uses a molybdenum target to produce characteristic low energy x-ray spectrum necessary for high contrast imaging.
- Compression plates - to spread the breast to increase x-ray penetration through the breast also reduces scattered radiation and prevents patient motion artefacts.

- Anti-scatter grid- removes scattered radiation which would otherwise be detected in the image and add significantly to the image noise.
- film -screen system- detects x-rays in the fluorescent screen and stores the image upon a photographic emulsion/film.
- Automatic exposure control- used to ensure correct exposure of the film avoiding over and under exposure.

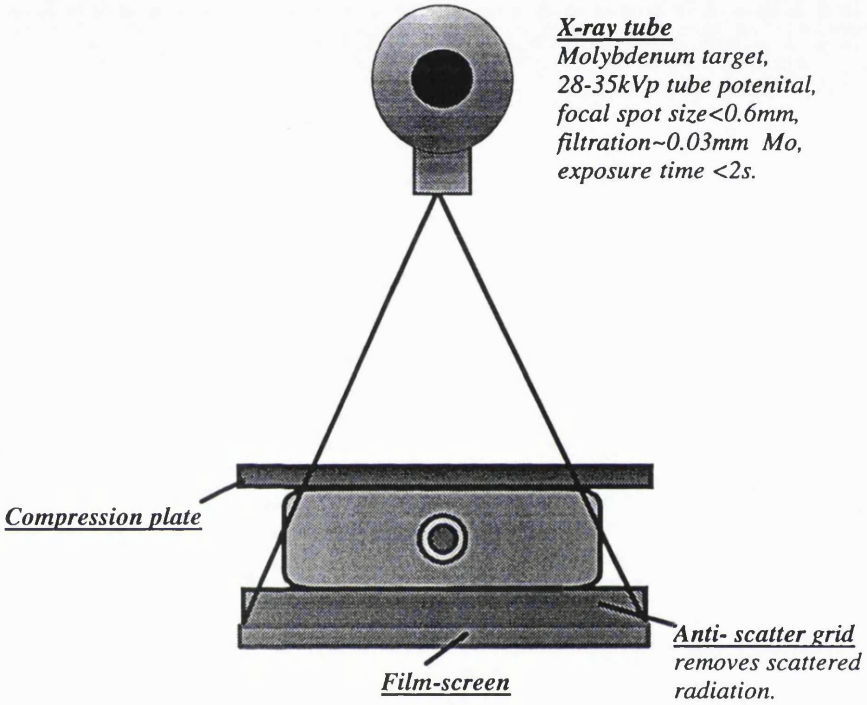

Figure 1.1 diagram of typical mammography system.

1.2 Limitations of film/screen systems

The modern mammographic detector consists of a single intensifying screen in contact with a high contrast film or emulsion. x-rays incident upon the screen are converted into optical photons which are then easily detected by the film. The intensifying screen increases the x-ray absorption efficiency of the detector and provides a gain in the number of quanta incident upon the film.

Figure 1.2 shows a typical film characteristic curve. In order to maximise the display contrast in the film it is necessary to ensure that all relevant radiological information is contained in the linear section of the characteristic curve. The automatic exposure control (AEC) attempts to do this and also prevents over and under exposure of the film. The use of the AEC combined with an anti-scatter grid results in an increase in dose to the patient.This arises because, with the removal of scattered radiation, more x-rays are required to lift the film density out of region 1 of the characteristic curve.

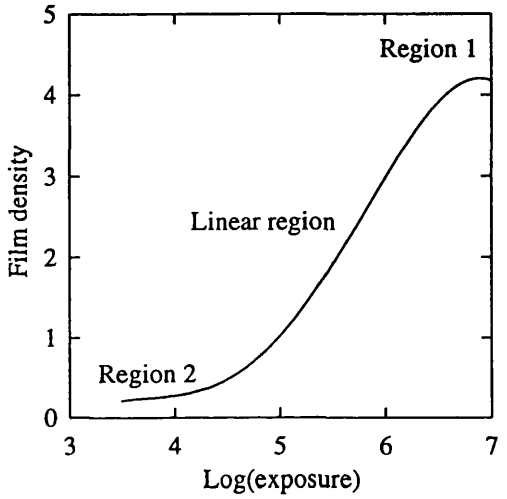

Figure 1.2 a typical film characteristic curve.

Another result of the film characteristic curve is that low contrast objects such as tumours may fail to be displayed in thick/thin areas of the breast corresponding to region2/region1 in the curve.

The spatial resolution of the film/screen system is a major factor in determining the minimum size of object that can be resolved. Because mammography is a dose restricted procedure there exists a compromise between spatial resolution and x-ray sensitivity. The x-ray sensitivity could be increased by using thicker or double screens but this leads to a consequent lose of resolution. Current guidelines require a spatial resolution in excess of 10 lp/mm.

The main sources of image noise are:

- X-ray quantum noise - caused by fluctuations in the number of detected x-rays per unit area.
- screen structure noise - caused by fluctuations in x-ray sensitivity and optical light output across the surface of the screen.
- film granularity caused by fluctuations in the number of sensitive grains per unit area in the film.

Film granularity is the dominant noise source at high spatial frequencies which can severely inhibit the system's ability to display micro-calcifications (Nishikawa and Yaffe 1987)

1.3 Advantages of digital mammography

The effectiveness of film screen systems for the detection of minimal breast cancer suffers from a number of fundamental limitations. These are summarised as follows:

- Compromise between displayed contrast and system latitude (dynamic range) which arises from the shape of the film characteristic curve.
- Film granularity which inhibits the systems ability to display micro-calcifications.

Digital detectors, such as CCDs, with a linear response of over a large dynamic range do not have these limitations. Images from CCDs contain a fixed pattern noise arising from screen structure noise and dark current noise which could produce effects similar to film granularity. However this can be virtually eliminated completely by using simple software algorithms upon the detected image This algorithm is discussed further in chapter 3.

Besides overcoming the limitations of film screen systems digital mammography has a number of other benefits. These include the use of tele-diagnosis where images can be passed between screening sites allowing further evaluation, and the use of image processing to aid diagnosis. Research into computer aided detection and classification

detection of microcalcifications (Jiang et al. 1992, Lefebvre et al. 1995, Nishikawa et al. 1994, Suckling et al. 1995) has been both popular and successful and emphasises the need for a digital imaging system.

At the time of writing of this thesis clinical testing of a prototype digital mammography system in Toronto, Canada was due to begin. This prototype has been shown to produce images which exceed the requirements of the American College of Radiology (Maidment et al. 1993).

1.4 Theory and operation of CCDS

Charged coupled devices (CCDs) were first proposed in 1970 by Boyle and Smith in an attempt to produce an electrical equivalent of magnetic bubble memory devices. Their application to imaging was quickly realised and it is in this field that the greatest effort has been concentrated. These devices have the following advantageous properties:

- Linear response
- Large dynamic range
- High quantum efficiency for optical wavelengths
- Broad range of spectral response
- Low readout noise
- High spatial resolution

The fundamental building block of the CCD is based on the MIS capacitor (metal, insulator, semiconductor capacitor). The MIS capacitor can be fabricated on p-type (boron doped) epitaxial silicon on which an insulator layer of the order 1000Å is grown (usually composed of silicon dioxide or silicon dioxide and silicon nitride - a dual insulating system). This layer is followed by a conductive gate deposition (typically doped poly-silicon). The CCD is composed of these closely spaced MIS capacitors which can be arranged in a number of different architectures. The brief description of the theory of operation of CCDs and various design architectures is given below for a fuller description the reader is referred to a volume by Benyon and Lamb (McGraw-Hill 1980).

1.4.1 Charge storage.

When a positive voltage is applied to the gate, majority carriers (holes in a p-type semiconductor) in the silicon are repelled from the region beneath the silicon-insulator interface leaving a depletion region shown in Figure 1.3. As the gate voltage is increased, the depletion region extends further into the substrate and as one might expect the potential of the silicon-insulator interface (known as the surface potential) becomes increasingly positive.

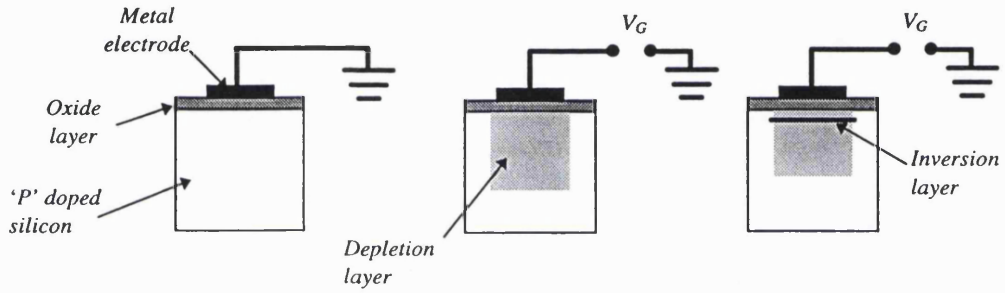

Figure 1.3 Diagram of CCD electrode.

The potential variation within the depleted region is such that a potential well for electrons forms at the surface. The depth of the well and hence its capacity to store charge is governed by the magnitude of the gate voltage and the insulating layer thickness. The area of the gate electrode determines the cross sectional area of the well.

If minority carriers (electrons) are subsequently made available, the depletion layer will shrink and the surface potential will fall as the electrons are attracted to the surface to form an extremely thin and very dense inversion layer. The idea of looking upon a CCD storage site as a potential well is invaluable as long as one remembers that the potential well is a hypothetical concept in which charge is represented as a liquid , the volume of which is proportional to the amount of charge present in the inversion layer.

1.4.2 Charge coupling.

To understand how a potential well can be moved from one location to another in a CCD structure consider the arrangement of four closely spaced electrode gates shown in Figure 1.4. It is assumed that some charge is stored initially in the potential well under the second electrode biased to 10V. The potential well under the 10V electrode will be much deeper than those under the 0V electrodes and so providing it is not "over filled", it will be only in this well where the charge will be stored shown in Figure 1.4(a).

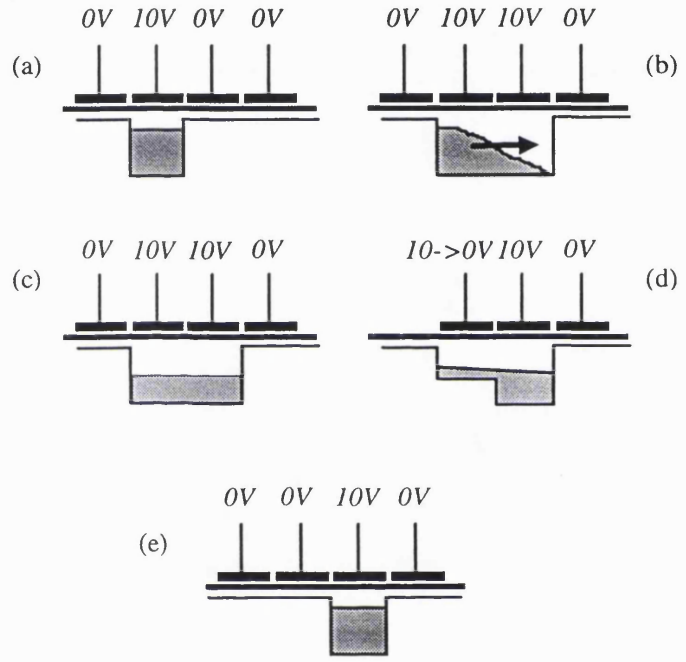

Figure 1.4a)-e) Movement of potential well and associated charge packet. Diagram from Benyon and Lamb.

If the second and third electrode are sufficiently close together then as the bias of the third electrode is increased to 10V, Figure 1.4(b). their respective potential wells will merge and so the charge packet originally under the second electrode becomes shared between the wells under the second and third electrodes, as in Figure 1.4(c). If the potential on the second electrode becomes reduced to 2V the remaining contents of its potential well will be shifted into the third well Figure 1.4(d). The final situation is similar to Figure 1.4(a). but with the deep potential well and it's associated charge packet moved one place to the right.

It is clear that by applying a succession of varying voltages to the CCD electrodes a charge packet can be propagated in a controlled manner just beneath the surface of the semiconductor.

1.4.3 Buried channel devices.

The last discussion described a surface channel CCD, because charge packets are stored and transferred along the surface of the semiconductor i.e at the Si-SiO_2 interface. A major problem exists with surface channel CCD's in that charge can become trapped in interface traps found at the surface which severely limits charge transfer efficiency (CTE) performance (the first CCD had a CTE of 98% which is far too low for scientific applications).

The bulk/buried channel CCD eliminates the deleterious effect of surface states by causing the potential wells to form, not at the semiconductor-insulator interface, but some distance into the bulk semiconductor where the surface states have no effect. This also has the effect of reducing temporal noise and provides highest readout rates. Buried channel CCDs have a region of n-type material (typically a phosphorus implant) forming the buried channel. In comparison to the surface channel structure, the extra n-dopant reshapes the potential well so that electrons are found to collect below the Si-SiO_2 interface (see Figure 1.5).

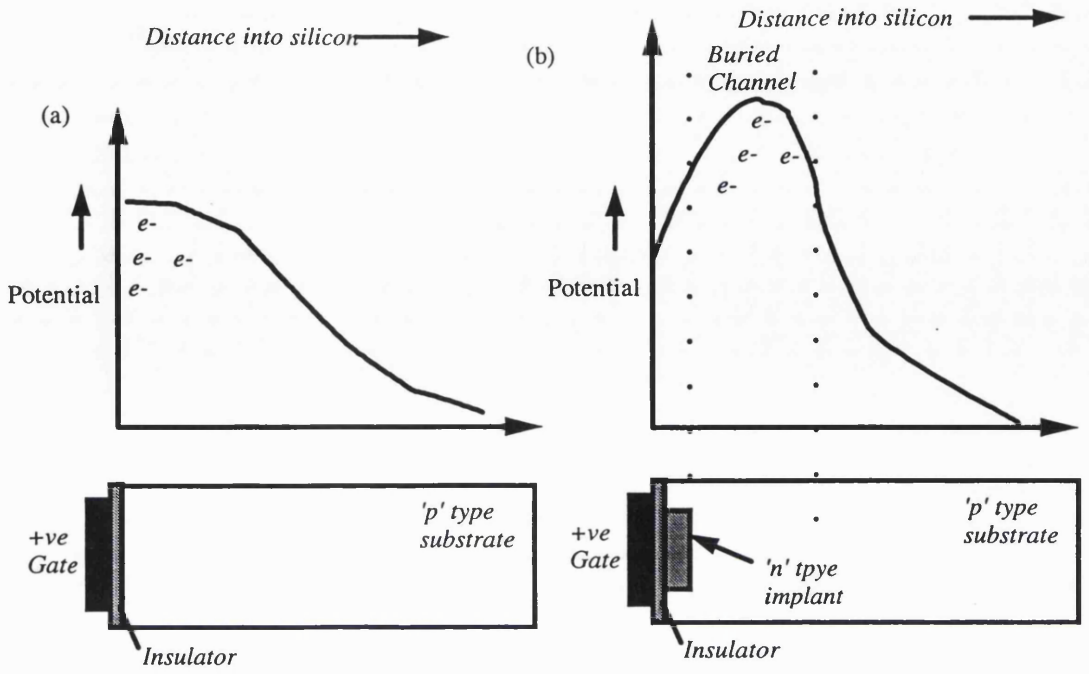

Figure 1.5 potential profiles across (a)surface channel CCD (b) buried channel CCD.

1.4.4 Principles of CCD imaging.

As an optical imaging device the CCD analogue shift register may be used to collect and read out optically generated signals. Incident light forms an image on the front face of the CCD. Initially, any one set of electrodes, is held at a positive clock voltage, thus creating a potential well under each of these electrodes; the other electrodes are held at zero volts or a small resting potential. Photons entering the silicon substrate, either through or between the electrodes (depending on the electrode material), generate electrons by virtue of the photoelectric effect. The electrons generated within the depletion regions are collected under each high electrode. The number of electrons collected under a given electrode within a given period is proportional to the local light intensity. Thus the pattern of charge that collects under the electrodes is an analogue replica of the light intensity across the original image. At the end of the integration period the charge pattern is read out by clocking the area in a conventional manner, care being taken to ensure that the clocks run long enough to clear out every charge packet. At the end of the readout period the device is again switched to integration mode and the cycle is repeated.

1.4.5 Frame transfer (FT) devices.

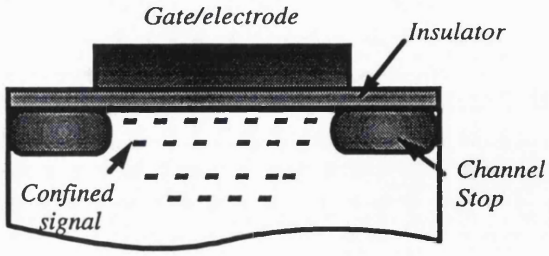

Figure 1.6 the use of channel stop diffusions to produce columns in the CCD.

The FT organisation is shown schematically in Figure 1.7. The array is divided into vertical columns by channel stop diffusions while electrodes running across the array at right-angles to the channel stops divide the array into horizontal lines. Channel stop diffusion are heavily doped P type regions which lower the potential in their vicinity, thereby confining generated signal electrons and defining columns in the CCD (see Figure 1.6).

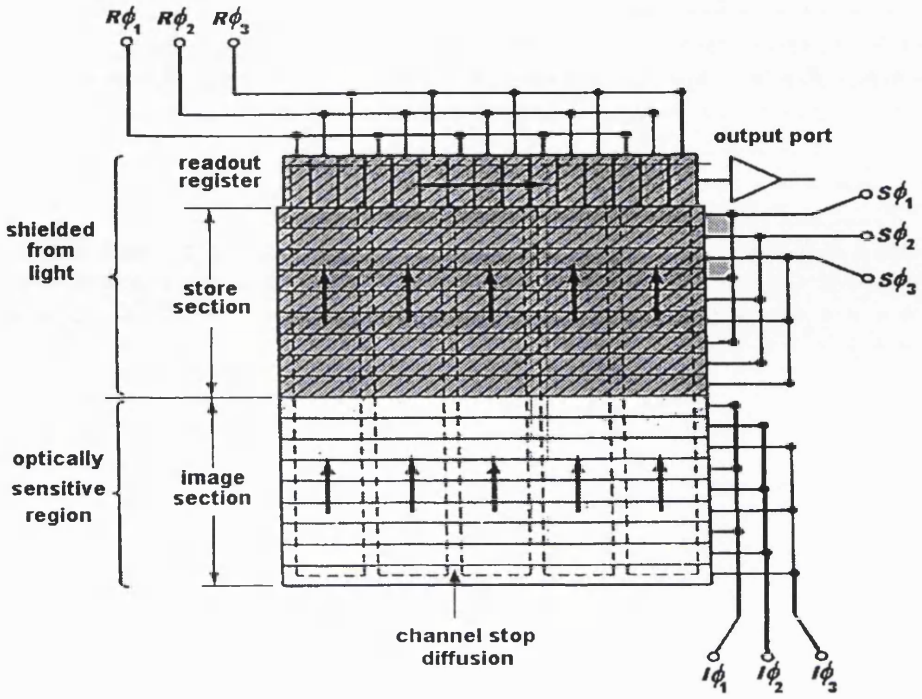

Figure 1.7 Schematic diagram of the FT-CCD detector architecture (Benyon and Lamb).

The electrodes are grouped into two sections; a lower optical integration section and an upper storage section. A horizontal readout register allows serial readout of data from the store, the direction of charge transfer being indicated by arrows. Both store and readout registers are shielded from the incident illumination either by using a metal overlay on the device or by masking the device externally.

At the end of the integration period the collected charges are transferred into the store by applying clock pulses to the electrodes of both integration (Iϕ) and storage sections.(Sϕ) Then by means of appropriate clocking of the store and readout sections (Rϕ), the whole frame of information is moved one line at a time up the storage section. A second frame of information is collected as the first is being read out. Once readout of the first frame is complete, the second frame is transferred to the store for subsequent readout, and so on.

1.4.6 Time delayed integration (TDI) devices.

The TDI image sensor is organised into an array of photosensitive elements consisting of n columns and m rows, with charges transferred along the columns (y direction). In a static situation, such an arrangement would produce an image only along rows (x direction), since spatial resolution in the y direction would be lost due to charge smearing down columns. However, if relative motion between object and detector is introduced, it is possible to produce a two-dimensional image. If charge is transferred along columns with a speed V_c, and the image is stationary in the detector plane, TDI implementation requires that the detector be translated with a speed V_d equal to V_c but in the opposite direction see Figure 1.8. This allows the charge generated in one portion of the image to integrate in the detector during image acquisition, eventually providing a signal m times larger than that accumulated in any individual element. Since the CCD readout noise contributes only once to the integrated signal , the signal-to-noise ratio using the TDI approach is greater than devices which use off chip integration. With the TDI approach the length of the image produced is not limited by the size of the CCD.

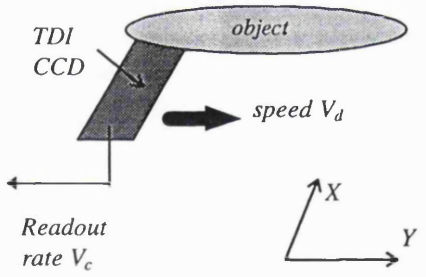

Figure 1.8 Diagram to show TDI operation

1.4.7 CCD charge output

When a charge packet has been clocked to the output node of the CCD it is converted to a voltage by means of an output circuit. The output circuit consists of 2 field effect transistors (FETs); a reset FET and an output FET shown in Figure 1.9. The main steps in the readout are as follows:

- The reset FET is pulsed high to charge the gate of the reset FET to the reset drain potential.
- a charge packet is then clocked on to the CCD output node which causes the potential across the capacitance to drop by an amount given by $\Delta V=Q/C$ where Q is the charge and C is the associated capacitance. This potential drop is translated into a voltage signal through the output FET for amplification.
- The reset FET is pulsed high again the charge drains out through a resistor at the rest drain, resetting the output node for the next charge packet.

Monitoring of the potential across the reset drain allows a direct measurement of the average number of electrons present in each pixel. This technique is used for calibration of the system as detailed in chapter 3.

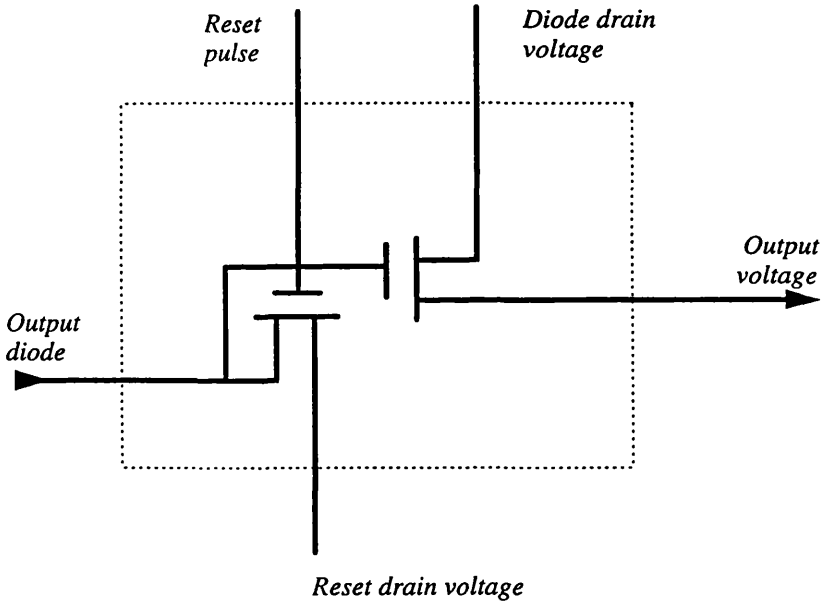

Figure 1.9 schematic of typical CCD output charge amplifier.

1.4.8 X-ray imaging using CCDs.

The useful photoelectric effect for silicon extends over a large spectral range (1.1eV to 10keV). The cut off for near infra-red photons occurs because the photon does not have sufficient energy to elevate a valence band electron to the conduction band. For energies above 10keV the probability of an interaction is small so CCDs have a low detection

efficiency for energies in the diagnostic x-ray range (10 to 100 keV). Figure 1.10 shows the interaction probability of a 0μm thickness of silicon as a function of incident photon energy. As can be seen for 0μm thick silicon only 5% of incident 20keV x-rays interact (0μm is the typical thickness of a CCD epitaxial layer).

Increasing the thickness of the epitaxial layer of the CCD will increase the x-ray response but because there is a limit the depth of depletion, the thicker device will not be fully depleted. Consequently any signal carriers produced by a interaction in the undepleted region will diffuse causing an increase in split events and will degrade spatial resolution.

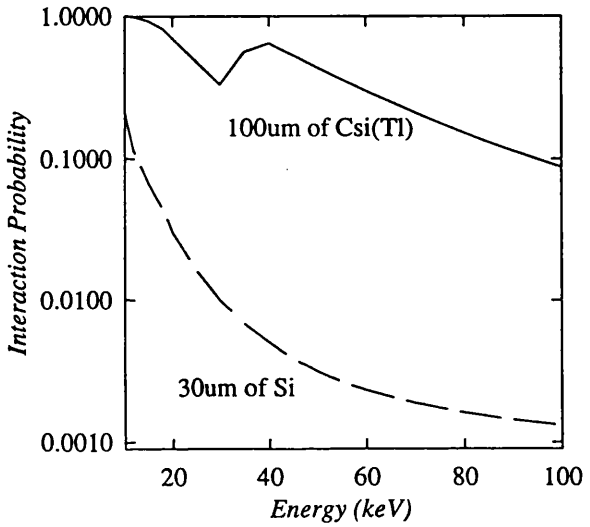

Figure 1.10 Interaction probabilities for silicon and CsI(Tl).

Another method of increasing the x-ray response is to deposit intensifying screens upon the surface of the CCD such as CsI(Tl). These screens convert the x-rays into optical photons which is more easily detected by the CCD. The interaction probabilities for 100μm thickness of CsI(Tl) is shown in Figure 1.10. In principle the interaction probability can be increased by increasing the thickness of deposited layer. As the screen thickness is increased however there is a degradation in the spatial resolution caused by spreading of the optical photons which is illustrated in Figure 1.11.

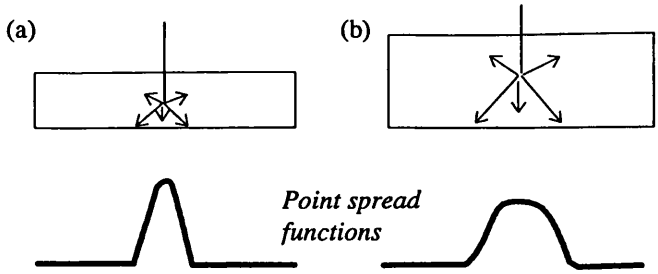

Figure 1.11 light spread in (a) thin screen (b) thick screen and their associated point spread functions.

For a dose restricted imaging procedure such as mammography the detector system must have both, high quantum detection efficiency and high spatial resolution. The choice of screen and screen thickness must be chosen to maximise quantum detection efficiency and give the required spatial resolution. In this project 3 different screens were available for testing detailed as follows:

- CsI(Tl)- good spectral matching between screen emission and CCD response, high low energy absorption efficiency, transparent.30-120μm thickness' available.
- GdO_2S_2(Tb) used in current mammography screens good spectral matching between screen emission and CCD response, high low energy absorption efficiency, increased spatial resolution due to semi opaque nature.50μm thickness
- GdO_2S_2(Tb,Eu) added dopent of Europium shifts the emission spectrum towards higher wavelengths improving the spectral matching. 200 μm thickness

The use of the modulation transfer function (MTF) to characterise the spatial response of a detector is widespread. The definition of MTF requires it to be measured under noiseless conditions. Consequently any measure of limiting spatial resolution inferred from the MTF may not be realised in dose restricted examinations/images.

Spatial frequency dependent detective quantum efficiency DQE(f) provides a measure of the detectors ability to transfer signal to noise which has a close relationship with the quality of images (Rose 1970). In this project the relationship between MTF, DQE(f) and image quality and other factors effecting were investigated.

1.4.9 Noise source associated with CCDs

The 4 main sources of noise associated with CCDs are discussed below:

1.4.9.1 Dark current noise

All silicon imaging devices suffer from the presence of dark current. It arises from the thermal generation of charge carriers which takes place in any semiconductor. In CCD image sensors the dark current causes the potential wells to be slowly filled with dark-generated charges, with the result that there is a maximum useful light integration time. A more serious limitation, however, is that dark current generation tends not to be uniform over the whole array and this fixed pattern noise is often a major factor in determining the sensitivity of the device. In addition, some devices may show exceptionally high dark current generation for some elements of the array;-the so-called dark current spikes.

Dark current is highly temperature dependent, decreasing by a factor of 2 for every 10°C fall in temperature. The cooling of an array is thus a possibility for decreasing the dark current to a suitable value.

1.4.9.2 Fixed pattern noise

As discussed in a previous section fixed pattern noise arises due to fluctuations in dark current generation and pixel responsively. It can be the dominant noise source at high illumination levels but can almost be completely removed by the use of a simple algorithm described in chapter 3.

1.4.9.3 Reset noise

During pixel readout there is an uncertainty associated with the potential to which the output node of the CCD is reset. This noise source can be eliminated using a technique known as correlated double sampling (CDS) described in detail in chapter 2.

1.4.9.4 Electronic noise

Background electronic noise arises from noise produced in the analogue components and power supplies in the system. Electronic noise must be kept to a minimum if the images produced are not to be degraded, this can be done by the use of low noise circuits.

1.4.9.5 Noise due to direct hits in the silicon

CCDs with directly coated screens are susceptible to direct hits in the CCD, that is x-rays which penetrate the screen interacting in the CCD. The large signal associated with each direct hit (~5500 electrons for a 20keV x-ray) may introduce a significant source of noise and reduce the detector dynamic range.

In order to remove direct hits in the CCD, a fibre optic coupling can be used between the phosphor and the CCD. Any x-rays which penetrate the screen will be absorbed in the fibre optic. The high transmission efficiencies associated with fibre optic couplings compared with lenses also favours their use (Lui et al).

The size mismatch between CCDs and the area of interest in mammography can be overcome by using CCDs operated in TDI mode scanned across the Breast (Maidment 1994). The system uses fibre optic tapers to de-magnify the image onto the CCD and also provide a means of butting together several detectors at the screen fibre interface. This butting procedure is successful with only a single fibre mismatch in the image.

CsI(Tl) is known to grow in columnar structures during vapour deposition (Stevels 1974). To take advantage of this intagliated fibre optics have been developed (Ito et al

1982). These fibre optics consist of a face-plate with the cladding of each fibre etched to leave the core of the fibres exposed. CsI(Tl) is then grown to form columns upon the cores. Optical light generated from an x-ray interaction in one of the columns is confined by internal reflection so that spatial spreading is reduced. In this project an intagliated fibre optic face-plate manufactured by Hamamatsu is investigated.

1.5 Summary and discussion

This chapter has discussed how the limitations associated with film/screen mammography may be overcome by exploiting the linear response of digital detectors over a wide dynamic range. Other advantages of digital mammography have been discussed such as computer aided detection/diagnosis and tele-diagnosis.

Previous research has shown that a CCD based digital mammography system can produce images comparable with film/screen. This thesis is an investigation into the effects factors such as phosphor thickness, transmission efficiency, MTF and DQE(f) have upon the quality of images produced from such a system.

The aims of this thesis include:

- To investigate the relationship between detector DQE(f) and image quality.
- Investigate the effects of direct hits in directly coated CCDs.
- Investigate the properties of intagliated fibre optics.
- To prescribe optimum detector parameters such as phosphor thickness , transmission efficiency for use in mammography.

CHAPTER 2

2. A CCD based imaging system

This chapter describes the design and construction of a prototype charge coupled device based x-ray imaging system. The prototype was constructed for the purpose of testing and comparing various different detector configurations. Although images produced from the system are limited to a maximum size of around 28mm × 7mm, it is possible to measure relevant system factors such as modulation transfer function (MTF) and noise power spectrum (NPS). It was also possible to obtain images of a breast phantom to provide direct comparisons of image quality between the various detectors. The use of a scanning system to move the detector across a larger image area with the CCDs operated in TDI mode is discussed in a parallel piece of work (Court 1995).

2.1 System Description

The CCD based x-ray imaging system is PC controlled and consists of a CCD camera, a timing generator, a digitising CDS unit, a video frame grabber and an x-ray tube. A schematic diagram of the system is shown in Figure 2.1.

The camera board and x-ray tube were housed in a lead lined room for radiation safety precautions.

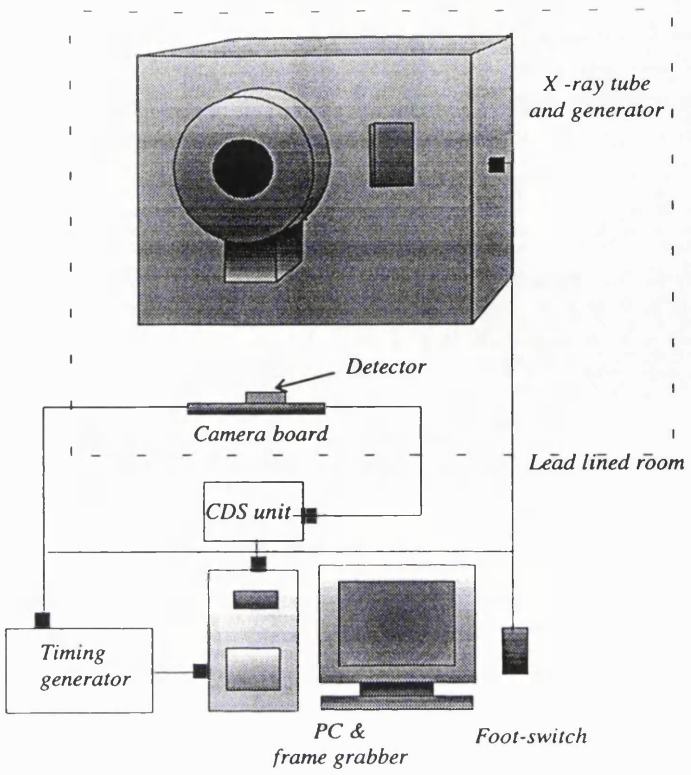

Figure 2.1 diagram of CCD based imaging system

2.1.1 SIRA timing generator

The SIRA (Scientific Instrumentation research association) timing generator allows the generation of variable CCD clock sequences. The sequence files are down-loaded from the computer into the RAM in the timing generator PCB using a program that accepts a text file of simple commands. A total of 23 TTL outputs are available from the unit. Some of these are used to provide frame, line and pixel synchronisation signals to the digitising / video frame grabbing system. The rest of the output lines are available as level clocks, which are used as inputs to CCD drive converters to produce actual clocks.

Each of the output lines can be set to TTL HIGH or LOW at any of the master clock transitions by the information which is entered into the sequence file. The time for which the output remains constant is set by specifying the number of cycles of the master clock. This clock runs at up to 32 Mhz, allowing pixel rates of 10.67 Mhz for a three phase CCD. The timing generator signals are summarised below:

to CCD

- i1,i2 i3 clocks to move charge packets down the columns.

- r1,r2,r3 clocks to move charge packets along the readout register.

- Reset pulse to the CCD drain circuit.

to CDS/digitiser unit

- Pixel and Clamp signals

to Frame-grabber board

- End of line synchronisation.

- End of frame synchronisation.

All timing sequences were programmed to match the sequences supplied in the CCD specification sheets, the timing regime for the EEV's frame transfer CCD 02-06 device is shown in Figure 2.2.

A range of integration times can be obtained by holding all clocking signals constant for the required period.

*All measurements were performed at 298K for the 15_11 CCD and 288K for the 02_06 CCD.

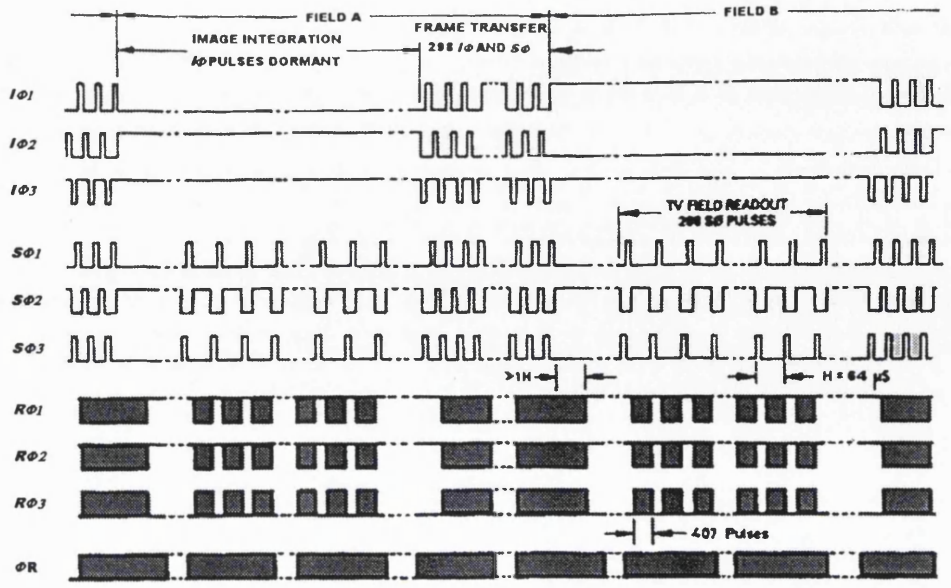

Figure 2.2 Clock timing sequences for EEVs CCD02-06 frame transfer device (EEV Ltd).

2.1.2 CCD camera.

The CCD camera controls the CCD and amplifies the signal to be sent to the CDS unit. The camera was custom made using a 'speed-wire' board . It contains line drivers to convert the TTL pulses from the timing generator and provides the correct operating voltages for the CCD. The analogue video signal from the CCD is amplified using a low noise circuit and is sent to the CDS unit for digitisation. The CCD camera layout is shown in Figure 2.3. The camera also contains an electronic Peltier cooling system to cool the CCD to reduce dark current.

The camera has two separate CCD sockets, one was set up with correct voltages to drive the 15_11 type CCD device and the other to drive the 02_06 type device. All operating voltages were set according to EEV's specification. The gain in the amplifying circuit in the camera was set (by changing a gain resistor) so that the maximum output voltage signal was equal to the maximum input voltage signal for the CDS unit (around 1Volt). A measure of the current from the CCD can be obtained by measuring the voltage V_{RD}, arising from the reset drain in the CCD, across a known resistance. A low noise circuit is included in the camera to allow accurate measurements of V_{RD}.

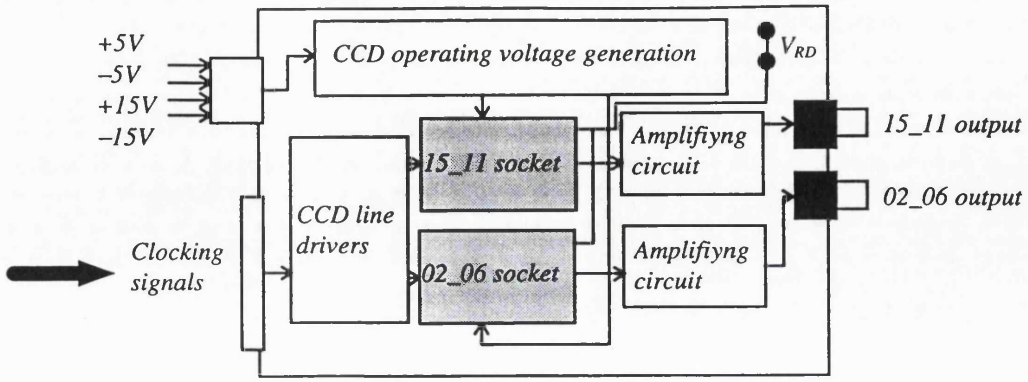

Figure 2.3 diagram of camera board layout

2.1.3 CDS unit

The SIRA CDS correlated double sampling unit digitises the video signal before it is 'grabbed' by the digital video frame grabber . Correlated double sampling refers to the technique of eliminating the noise component which arises from resetting the output drain of the CCD.

Analogue video signals from the CCD and synchronisation signals from the timing generator are used to digitise the video signal. The ADC converts the video signal to 12-bit signal at a rate of up to 10MHz. Pixel, line, and frame synchronisation signals are added to the digitised video signal and sent to the PC based video frame grabber.

The CDS unit has three gain settings high, medium, low. The gain can easily be changed by replacing gain resistors. A set of two variable resistors control the level of the d.c. offset at which the video is digitised.

2.1.4 Video frame grabber

The frame grabber used was the Imaging Technologies MFG with the AM-DIG -16D module. The AM-DIG module receives pixel data based upon timing signals (pixel, line enable, frame enable) provided by the digitising CDS unit and synchronises this data to the MFG mother board timing. Video data is loaded into line FIFOs (first-in first-out data buffer) at camera clock rates and unloaded at mother board clock rates. The MFG is fully programmable and can store 3072 by 1024 by 16 bit frames.

Software supplied with the MFG allows the user to define areas of interest on the video display and to define the CCD specific parameters such as array format and synchronisation signal polarities.

All images were obtained with the MFG programmed to accept 12 bit data. When 15_11 type CCDs were used the MFG was programmed to accept 1024 by 256 pixel frames. For 02_06 type CCD devices the MFG was programmed to accept 385 by 288 pixel frames.

Table 2.1 description of Commands used in 'C' program.

Command	*Function*
Snap	Acquire a single frame
Grab	Acquire frames continuously
Calc	Calculate mean ,standard deviation, maximum and minimum pixel values and their positions x,y.
Save	Save in either *.TIF or *.MFG format
Dark	Aquire Dark images
Norm	Aquire Normalisation images
Correct	Correct images

2.1.5 Personal computer

The PC contained an 80486 based processor with an operating frequency of 66Mhz.with 16Megabytes of RAM. The timing generator and frame grabber were both plugged in to ISA slots and housed in a mini tower casing.

Timing sequences for the CCDs were programmed using text files and manufacturers supplied software was used to implement them.

Software libraries supplied with the Frame grabber were used to write a 'C' program to control image acquisition from the camera board. A summary of the commands available in this program is shown in Table 2.1. The images could be analysed saved to hard disk and further analysed in a unix based application called Dispimage, written by D. Plummer in the Medical Physics Department at UCL.

2.1.6 X-ray tube

All x-ray measurements where performed with a Siemens Mammomat I system. The generator has 4 tube potential settings (28, 30, 35, 40 kVp) and a dial which combined tube current and exposure time to give a range of "mAs" values. The tube has a choice of either a molybdenum or aluminium filter. Only the molybdenum filter was used in this project.

To ensure that the all the x-ray flux from an exposure was captured in a single video frame a simple circuit was made. This circuit enabled a footswitch was used to prepare the tube, that is, to set the anode rotating and a frame enable trigger from the timing generator board switched the tube to expose. A diagram of the circuit is shown in Figure 2.4.

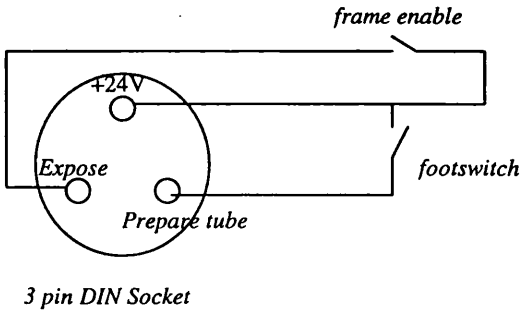

Figure 2.4 diagram of circuit used to control x-ray tube.

2.2 Detectors used

All detectors consisted of a x-ray converting phosphor screen either directly coated onto a CCD or coupled via a fibre optic stud or taper as shown in Figure 2.5. Details of all the detectors investigated are shown in Table 2.2.

Table 2.2 Detectors investigated

Detector ID	*phosphor screen*	*fibre optic coupling*	*CCD type*
dc120C	CsI(Tl), 120μm	none	15_11
dc70C	CsI(Tl), 70μm	none	15_11
dc50C	CsI(Tl), 50μm	none	02_06
dc45C	CsI(Tl), 45μm	none	15_11
dc30C	CsI(Tl), 30μm	none	02_06
fo120C	CsI(Tl), 120μm	1:1a	15_11
fo70C	CsI(Tl), 70μm	1:1a	15_11
fo50C	CsI(Tl), 50μm	1:1b	02_06
fo200G	GdO_2S_2(Tb), 200μm	1:1a	15_11
fo50G	GdO_2S_2(Tb,Eu), 50μm	1:1b	15_11
foMinR	Kodak Min-R	1.1t	15_11
fohama	Hamamatsu CsI, 80μm	1.1a	15_11
ft120C	CsI(Tl), 120μm	1.5:1t	02_06
ft70C	CsI(Tl), 70μm	1.5:1t	02_06

Detectors with the prefix 'dc' (Table 2.2) have direct coatings of phosphor screen onto the CCD, all CCDs are 15-11 devices except for the 30μm and 50μm CsI(Tl) coated detectors which are 02-06 devices.

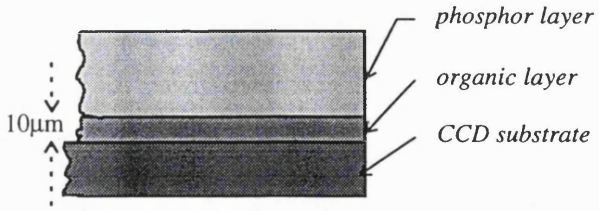

Figure 2.5 diagram of EEV's coating process

Detectors with the prefix 'fo'(Table 2.2) have a fibre optic stud which coupled the phosphor screen to the CCD. With the exception of fo120C, fo70C, fohama and foMinR, all phosphor screens were coated directly onto the fibre optic stud. Detectors fo120C and fo70C have their phosphor screens coated onto a fibre optic disc which was coupled to a fibre optic stud, as shown in Figure 2.6.The use of coupling fluid between

the fibre optic disc and fibre optic stud was found to increase the light detected in the CCD by 24% see chapter 3.

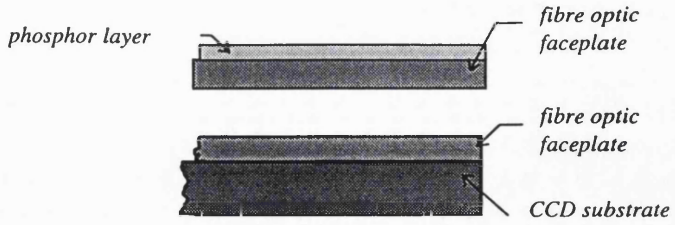

Figure 2.6 Diagram of fo120C, fo70C configuration.

Detector fohama is similar to detectors fo120C and fo70C but uses an intagliated fibre optic faceplate supplied by Hammamtsu. This intagliated faceplate has a fibre pitch of 10μm with an 80μm thick CsI(Tl) phosphor coating and a reflective top surface as shown in Figure 2.7.

Intagliated face plates have their cladding etched away leaving the cores exposed. When CsI(Tl) is vapour deposited upon the surface it grows forming columnar structures.(Stevels 1974). These columnar structures channel the scintillation quanta produced down through a single fibre and reduce image blur (Ito et al 1982).

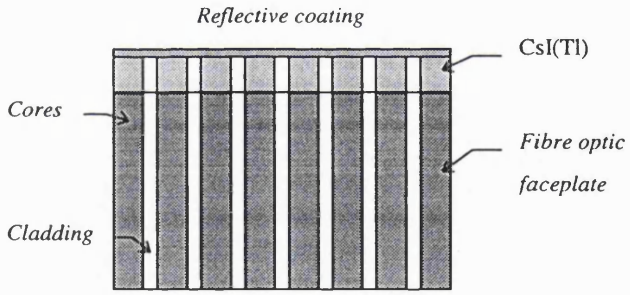

Figure 2.7 Intagliated fibre optic faceplate used in detector fohama

A diagram of the configuration of detector foMinR is shown in Figure 2.8. A section of a Min R screen cassette was cut out and used to hold the screen in close contact with the fibre optic stud. No coupling fluid was used between the screen and fibre optic stud as this was found to dissolve the screen.

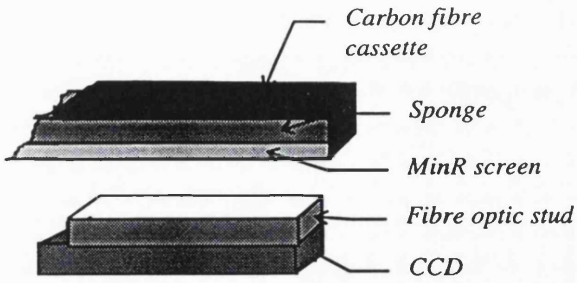

Figure 2.8 Diagram of detector foMinR

Detectors with the prefix 'ft' (Table 2.2) refer to detectors with a fibre optic taper coupling between the phosphor screen and the CCD and are similar in configuration to detectors fo120C and fo70C.

2.2.1 CCD Devices used

Table 2.3 shows details of the two CCD sensors used in the project. All sensors were EEV, front illuminated, 3 phase devices. EEV's 15_11 device is a full frame device (1024 × 256 pixels) which can be used for time delay and integration. The 02_06 device is a frame transfer device with an image region (385 × 288 pixels) and store region (385 × 290 pixels). Both CCDs are packed in a 20pin DIL ceramic package.

Table 2.3 CCD specifications

CCD type	*15_11*	*02_06*
Operation mode	full frame	frame transfer
Array format	1024 × 256 pixels	385 × 288 pixels
Active area	27.64 × 6.91 mm^2	8.5 × 6.3 mm^2
Pixel size	27 × 27 μm^2	22 × 22 μm^2
Quantum efficiency (550nm)	.31	.31
Peak signal	≈ 700k e^-/pixel	≈ 300k e^-/pixel
Max. output from charge amp.	≈ 2V	≈ 0.14V
Pixel readout rate	800kHz	1.0Mhz

All experiments with CCDs involved them operating at their recommended maximum pixel readout rate. CCD 15_11 devices were operated with a pixel readout rate of 800kHz which led to a frame period (time to readout the whole device) of 0.281 seconds. The 02_06 device was operated with a pixel readout rate of 1Mhz which led to a frame period of 0.181 seconds.

The 15_11 device was not designed for integrating images, however the clocking scheme of the 15_11 CCD was modified to enable a sort of pseudo integration mode. This was done by holding all clocks stationary to collect charge for the required period and then quickly reading out the device. If the time of the exposure is less than the integration time then image smear caused by illuminating the CCD during readout are eliminated.

2.2.2 Fibre optic couplings used.

Three fibre optic faceplates were used details of which are shown in Table 2.4.

Table 2.4 Fibre optic coupling specifications

Taper ID	*1:1a*	*1:1b*	*1.5:1t*
type	Schott Hi-trans	EEV	Schott
core size	10μm	6μm	10μm
cladding size	1μm	1μm	1μm
thickness	0.5mm	0.3mm	3cm
magnification	1:1	1:1	1.7:1
index of refraction of cores	1.41	1.41	1.41
index of refraction of cores	1.84	1.84	1.84
transmission	60%	30%	17%

Values in the table were obtained from manufacturers data sheets. The fibre optic studs and tapers were obtained from EEV Ltd and Schott Fibres inc.

2.2.3 Phosphor screens used

Three types of x-ray converting phosphor screens have been investigated, details of which are shown in Table 2.5. They were chosen for their good attenuation properties, good overlap between the spectral output and CCD quantum efficiency curves and availability.

CsI(Tl) and gadox screens were obtained from EEV Ltd. As part of EEV's coating process a thin organic layer (≈10μm thick) is used as a 'pre-coat' to bond the phosphor layer to the surface to be coated as shown in Figure 2.5.

Table 2.5 Phosphor screen specifications

Phosphor screen	*CsI(Tl)*	*$Gd_2O_2S_2$(red)*	*Kodak Min-R*
peak emission λ(nm)	550	617	600
density (g/cm^3)	3.5	6.7	3.3
overcoat layer	~20μm	~20μm	No
no. light quanta (keV^{-1})	52	62	62

2.3 Summary

The prototype imaging system uses EEV CCD15_11 and CCD02_06 devices in integration mode with a typical integration time of 1s. Fourteen different detectors were available for testing and comparing . The whole system was fully controlled via a P.C. and specially written software. Problems with synchronising the x-ray exposure with the image frame acquisition were overcome by using a switching circuit controlled by a foot pedal.

CHAPTER 3

3. System tests and calibration

This chapter describes the tests and calibration of the CCD based imaging system. These include the evaluation of the following parameters:

- system stability
- system gain (electron/ADU)
- charge amplifier sensitivity ($\mu V/e^-$)
- system linearity
- CCD full well capacity
- x-ray sensitivity (electron/incident x-ray)
- x-ray quantum detection efficiency
- detector dynamic range
- fraction of signal due to direct interaction in the CCD.

In order to obtain quantitative digital images it is necessary to calibrate the system. This is achieved by calculating the system gain in terms of the number of electrons produced in a CCD pixel necessary to produce an analogue to digital unit ADU in an image pixel. The reliability of this measurement is dependent to a certain extent upon the system stability and linearity. The system linearity is calculated under both optical and x-ray irradiation. Knowledge of the system gain allows evaluation of other relevant parameters such as the charge sensitivity of the charge amplifier, the full well capacity of a CCD pixel and the x-ray quantum detection efficiency.

Theoretical models of x-ray sensitivity which include effects of optical coupling efficiency are presented. This work uses equations referenced to other workers.

The presence of thermally generated signal carriers in the CCD can severely reduce the dynamic range of the CCD. Dark current noise also contributes to the system noise and may be the dominant contribution . Dark current noise, together with the other noise contributors to system noise is characterised in section 3.6. Methods of minimising dark current noise are also presented. All of the noise and sensitivity measurements are in terms of magnitude only . The spatial distributions or textures are described in chapter 4 in the form of MTF and NPS analysis.

3.1 System stability

The time taken for the system to stabilise was estimated by making measurements of dark current as a function of time from when the system was turned on. From Figure 3.1 it can be seen that dark current increases with time until it levels off after 500 s. This is caused primarily by the CCD heating up until it reaches thermal equilibrium after about 10 minutes. The time taken for the system to stabilise can be reduced to a few minutes if the CCD is cooled. Each time the system was switched on it was allowed to stabilise for 5 minutes before any images were taken.

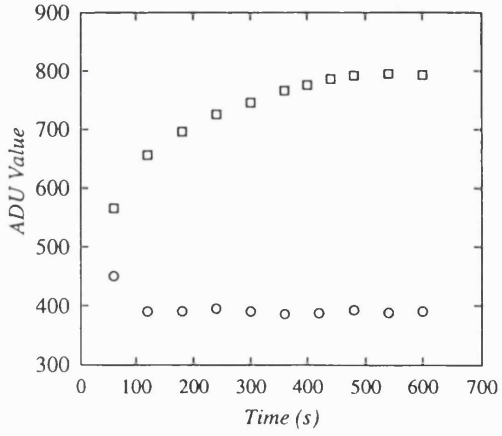

Figure 3.1 dark current as a function of time from switching on the system for cooled (circles) and uncooled (squares) 15_11 CCD.

3.2 ADU/volt calibration

To eliminate the effect of non-uniformities in CCD pixel response a specially designed low noise circuit was built and used to simulate a CCD. The circuit produced a stable square wave signal amplitude of V_{in} and period Δt, as input to the socket on the camera board which usually received the CCD output source V_{os}.

$$\frac{ADU_{HI} - ADU_{LO}}{V_{HI} - V_{LO}}$$

Eq 3.1

The square wave circuit has inputs from the third CCD clocking signal ϕR3, and a 10Volt d.c. source off the camera board. The amplitude of the signal could be varied from 0-10V using a variable resistor in the circuit. The signal has the same periodicity as ϕR3.

V_{in} is set to low value (at around 1Volt) and a video frame is obtained; the mean pixel ADU is calculated. This is repeated with V_{in} set to a high value (at around 8Volts). This is done for both CCD sockets (15_11 and 02_06) and for each gain switching on the CDS unit. The value of ADU/Volt is calculated using Eq 3.1.

Table 3.1 ADU/V values for three CDS gain settings

CDS gain	*1*	*2*	*3*
ADU/V (15_11)	1328±3.1	3957±3.1	10384±3.1
ADU/V (02_06)	7893±3.1	23284±3.1	57461±3.1

Table 3.1 shows the results obtained for the 15_11 and the 02_06 socket for each gain switching on the CDS unit. From these results it can be seen that a factor of ×3.0 and ×7.8 in gain is achieved for gain switches 1 and 2 respectively on the CDS unit.

3.3 Number of electrons per ADU (e^-/ADU)

Figure 3.2 shows a diagram of the experimental set-up for measuring the number of electrons per ADU for each detector. A tungsten filament lamp illuminates a green filter

and a series of semi opaque optical dispersing filters to produce a uniform or flat field of green light over the detector. The green filter was chosen to simulate the emission spectra of the phosphors used. A plot of its transmission spectrum is shown in Figure 3.4.

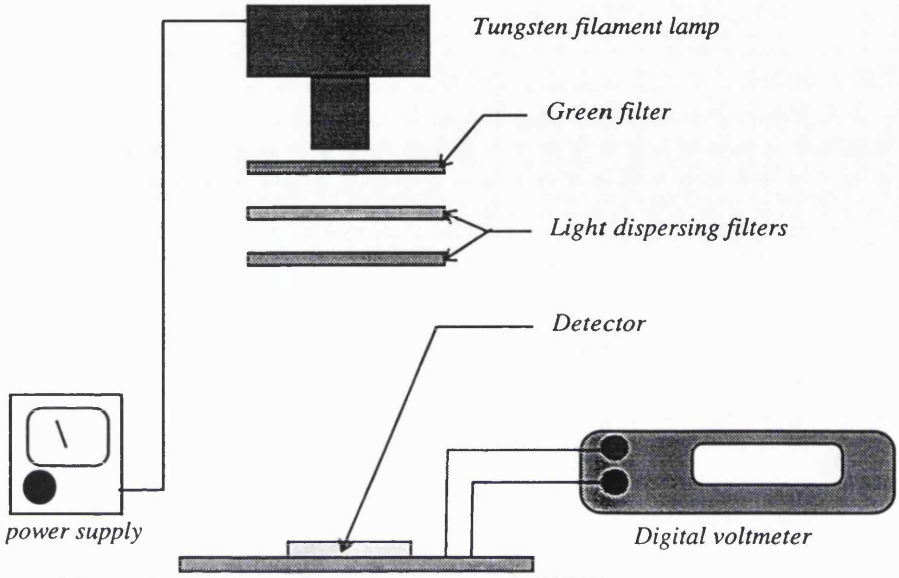

Figure 3.2 experimental set-up for measuring no. of e⁻/ADU

The uniformity or flatness of the field was measured using a photodiode and photometer. The photodiode was moved across the centre of the light field along one axis. Readings of light intensity were taken every 0.5cm across the light field. Figure 3.3 shows light intensity values for positions across the light field. The light field is uniform to within 1% over about 16cm which is adequate for the measurements made.

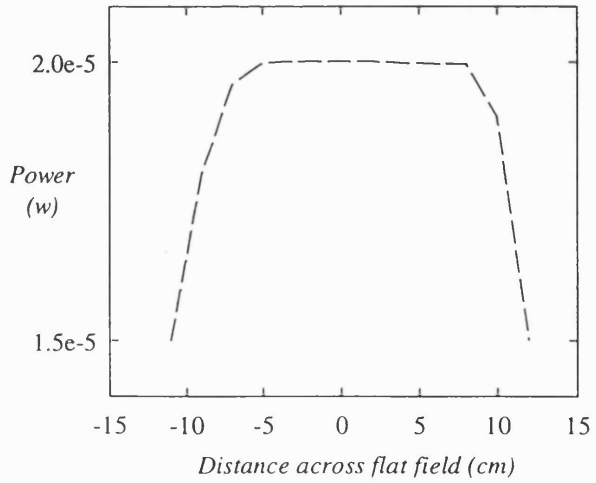

Figure 3.3 light power across flat field

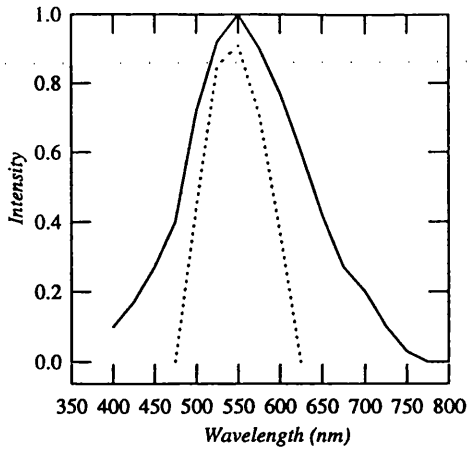

Figure 3.4 Dashed line is the transmission spectrum of green filter. Solid line is a typical emission spectrum of CsI(Tl) phosphor.

3.3.1 Method for calculating e⁻/ADU

The detector was operated in continuous readout mode with the CDS unit at gain1 setting and was placed in the flat field of light. Readings of V_{RD}, the voltage across the reset drain resistor (see chapter 1) were made. An image was 'snapped' and a mean pixel ADU value was calculated. This procedure is repeated for a number of light field intensities. The current I_{RD}, from the CCD reset drain gives a direct measure of the number of electrons produced in the CCD per second. The number of electrons per pixel is given in Eq 3.2 where $I_{RD} = V_{RD}/100k\Omega$. The charge sensitivity of the CCD charge amplifier is given in Eq 3.3.

$$\text{no. of electrons/pixel} = I_{RD} \times \text{pixel rate} \times \text{electron charge} \qquad \textbf{Eq 3.2}$$

$$\text{charge sensitivity } (\mu V/e^-) = 10^{-6}/(\text{no. of electrons/ADU} \times \text{ADU/volt}) \qquad \textbf{Eq 3.3}$$

3.3.2 Results of calculating e⁻/ADU

A plot of current in the reset drain against ADU value for a 15_11 device is shown in Figure 3.5. A regression was applied to the data and the gradient was calculated, values of the no. of electrons per ADU were calculated using Eq 3.2. The sensitivity of the CCD charge amplifier was calculated using Eq 3.3. Results for all detectors under test are shown in Table 3.2

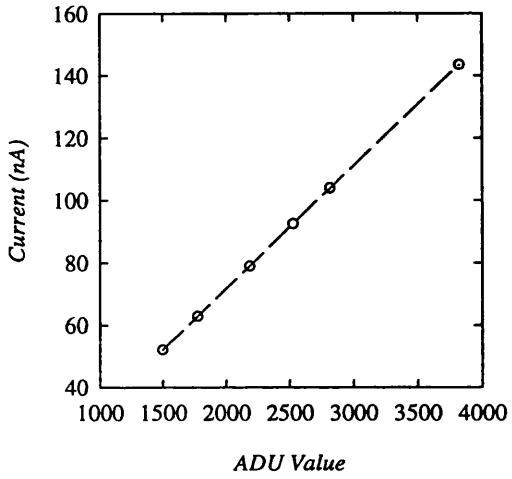

Figure 3.5 plot of current in reset drain against ADU value for 15_11 device. Circles correspond to measured points, the dashed line is a regression on the data.(298K).

Results show figures of around 300 e^-/ADU for 15_11 based detectors and around 120 e^- /ADU for the 02_06 detectors, estimated errors in the measurement were calculated from uncertainties in current readings and are 1%.

For the 15_11 based detectors, the discrepancy between figures of 2.5 μV/e^- for charge amplifier sensitivity and 3.0 μV/e^- (quoted in the manufacturers data sheet at 140K) are attributed to the measurement being made at 298K.

Table 3.2 results of no. of electrons/ADU calibration

Detector ID	*No. of electrons per ADU*	*Charge amplifier sensitivity(μV/e)⁻*
dc120C	304	2.5
dc70C	280	2.7
dc50C	110.2	1.1
dc43C	285	2.6
dc30C	118.2	1.1
fo120C	306	2.5
fo70C	306	2.5
fo50C	113	1.1
fo200G	298	2.5
fo50G	122	1
fohama	306	2.5
foMinR	306	2.5

For the 02_06 based detectors figures of about 1μV/e⁻ for charge amplifier sensitivity agree well with figures from manufactures data sheets. ✳

Measurements for the 02_06 device were made at 288K

3.4 System linearity

The same experimental set-up described in the last section was used investigate the system linearity.

3.4.1 Method for measuring system linearity

A image was taken with the detector placed in a field of uniform light and the average ADU and its standard deviation was calculated. The contribution to the signal due to dark current was obtained by repeating the procedure with the detector shielded from any illumination. The signal due to irradiance was then calculated by subtracting the dark current contribution. This was repeated for a range of illuminations.

3.4.2 Results of system linearity measurements

The number of electrons per pixel as a function of irradiance is shown in Figure 3.6. From the plot for the 15_11 CCD the signal is observed to be linear up to about ~40 nW/mm^2 where the device begins to saturate. Similarly the plot for the 02_06 CCD is observed to be linear up to ~26nW/mm^2.

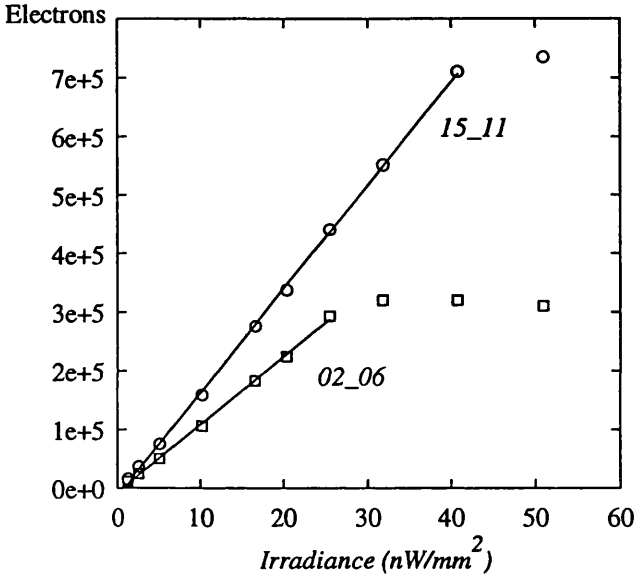

Figure 3.6 plot of no. of electrons per pixel as a function of irradiance. Solid lines are regressions to the linear portion of the data.

3.4.3 Full-well capacity

A CCD pixel has a limit to the amount of charge it can store. This limit is known as the full well capacity. When the limit is exceeds charge from the pixel spreads into adjacent pixels, an effect known as charge blooming. The point at which the graph in Figure 3.6 flattens out can be taken as an estimate of the irradiance at which onset of charge blooming occurs.

Values of the full well capacity where estimated to be ~7.1×10^5 electrons for the 15_11 CCD and 3×10^5 electrons for the 02_06 CCD which agree with the figures for full well capacities quoted by the manufacturer.

*Air kerma is the kinetic energy released by the xrays per unit mass of absorber (air)

3.5 X-ray measurements

Quality assurance tests where made to determine the main characteristics of the x-ray tube, these included output linearity and stability, focal spot size and half value layer (HVL).

The output of the tube was measured for a range of mA and kV_p. Air kerma was measured using a Keithley 35050A dosemeter fitted with a 15cc air ionisation chamber. Figure 3.7 shows that the tube output is linear with tube current and exposure time for the three tube settings. After a few pre-exposures, to warm the tube, the consistency of output was about 6% at the dial setting of 5mAs and 1% at 80mAs at 28 KVp.

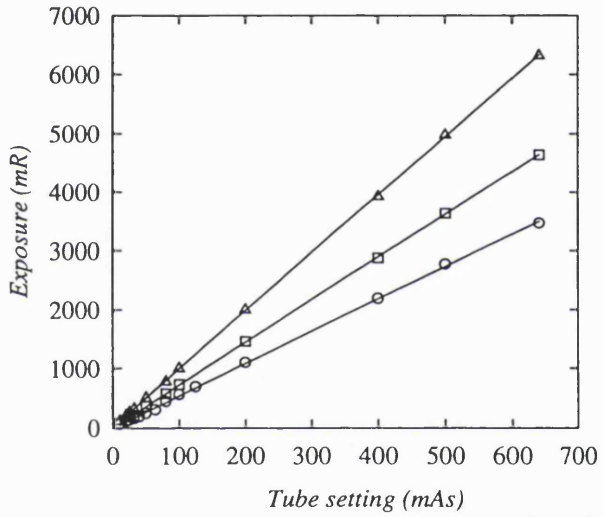

Figure 3.7 air kerma (at .75m) as a function of tube output setting. Solid lines are regressions to the data

The focal spot size was estimated using a star resolution grid with 1° spoke angles. A film screen was used to obtain a magnified image (magnification =3.2) of the star resolution grid. The distance between the outermost blurred regions on the image was measured and the focal spot size was calculated using Eq 3.4 (IPSM report no. 59),

$$\text{focal spot size} = \frac{\pi\theta}{180} \cdot \frac{D}{(M-1)}$$

Eq 3.4

where θ is the spoke angle of the star resolution pattern =1°, M is the geometrical magnification of the image and D is the measured blurring diameter on the image. A focal spot size of 440 × 460 μm was obtained.

The half value layer (HVL) was determined using a Keithley 115A aluminium HVL set and operating the tube with a 28 kVp beam for both filters. With the aluminium filter the HVL was found to be .448mm Al which corresponds to a inherent filtration of .72 mm Al (Cranley et al 1991). A HVL of .35mm of Al was obtained with the molybdenum filter in place which corresponds to an inherent filtration of 39μm Mo.

Knowledge of the filtration of the tube and kVp enabled the energy spectrum of the beam to be calculated using a program called XCOM (Berger et al) see Figure 3.8.

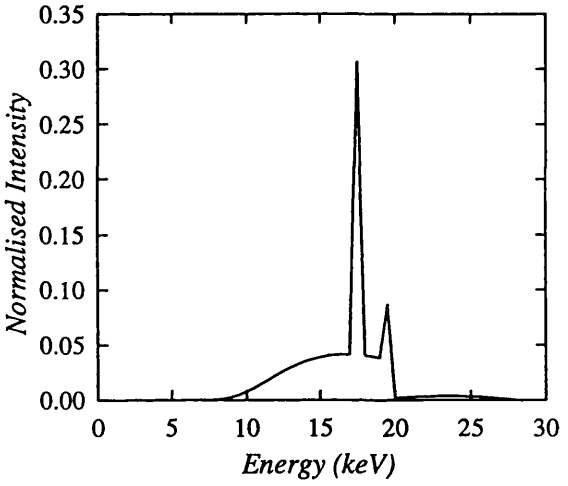

Figure 3.8 28kVp energy spectrum for Mo tube with 39μm Mo filtration

3.5.1 Linearity and sensitivity

The sensitivity of the system toward x-ray exposure was measured in terms of the number of electrons per pixel per entrance air-kerma at the input plane of the detector. The distance between the x-ray tube focus and the detector was kept constant at 0.75m. A 28kVp beam was used and three images were taken with each device for a range of exposures (measured using an ion chamber). The images where averaged and the dark signal contribution was subtracted.

$$\text{X - ray sensitivity} = \frac{\dfrac{\text{no. of electrons}}{\text{Exposure}}}{\dfrac{\text{no. of x - rays}}{\text{Exposure}}}$$

Eq 3.5

Figure 3.9 shows a plot of the number of electrons as a function of incident air kerma for various detectors. The system is observed to be linear in response to x-ray exposure for twelve detectors, this was the case for all subsequent detectors tested.

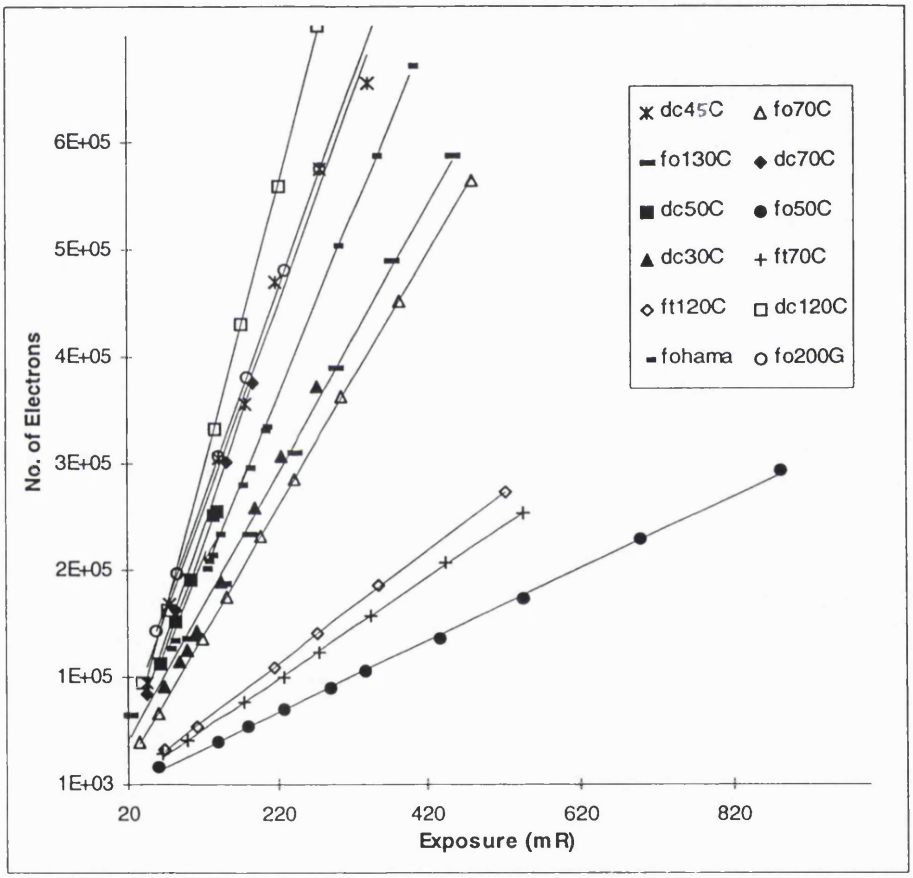

Figure 3.9 number of electrons per pixel as a function of incident air kerma for twelve detectors.

The x-ray sensitivity of each detector was expressed in terms of the number of electrons per pixel produced per incident x-ray which is given by Eq 3.5.

The number of electrons per unit exposure was calculated by finding the gradient of the linear regression data shown in Figure 3.9 and applying a correction for pixel size and

the number of x-rays incident per unit exposure is calculated using the method detailed in appendix 2.

3.5.1.1 Results and discussion for directly coated CCDs

Directly coated CCDs are the most sensitive of all the detectors used. This is as expected as no there is no light loss associated with additional optical coupling between the phosphor and the CCD and there is an additional contribution to the signal from direct hits in the CCD.

Signal contribution from phosphor $\Gamma_{phos}, = E \times \eta_{phos}(E) \times P(E) \times G \times \eta_{ccd}(E)$

Eq 3.6

The signal contribution from an x-ray of energy E incident on the phosphor Γ_{phos}, is given in Eq 3.6 where:

$$\eta_{phos}(E) = \left(1 - \exp\left(-\mu_{photo}(E) \times d_{phos}\right)\right)$$

Eq 3.7

- $\eta_{phos}(E)$ is the quantum detection efficiency of the phosphor at energy E, given in Eq 3.7 where:
  - $\mu_{photo}(E)$ is the photoelectric interaction coefficient for an x-ray photon of energy E,
  - d_{phos} is the phosphor thickness,
- $P(E)$ is the number of optical quanta produced when an x-ray photon of energy E is photoelectrically absorbed in the phosphor,
- G is a geometrical factor to account for the fact that not all the optical light, produced in the phosphor, reaches the output face of the phosphor,
- η_{ccd} is the optical quantum efficiency of the CCD which is calculated using the method described in appendix 1.

$$\text{Signal contribution from direct hits } \Gamma_{epi} = \left(E \times \left(1 - \eta_{phos}(E)\right) \times \eta_{epi}(E)\right) / 3.65\text{eV}$$

Eq 3.8

Assuming all x-ray interactions occur inside the epitaxial layer, the signal contribution from direct hits Γ_{epi} is given in Eq 3.8 where:

- η_{epi} is the x-ray quantum detection efficiency of the CCD i.e. it is equal to the percentage of incident x-rays of energy E which are absorbed in the depleted region of the CCD and is given in Eq 3.9 where:

$$\eta_{epi}(E) = \left(1 - \exp\left(-\mu_{epi}(E) \times d_{epi}\right)\right)$$

Eq 3.9

- $\mu_{epi}(E)$is the photoelectric absorption coefficient of silicon at energy E,
- d_{epi} is the depletion depth of the CCD.

The figure of 3.65 eV is the energy required to produce an electron-hole pair in silicon.

Combining Eq 3.8 and Eq 3.9 an expression for the sensitivity of the directly coated CCD $S_{e/x}$, under broad beam exposure conditions can be expressed as Eq 3.10 where $\Phi_x(E)$ is the normalised x-ray photon fluence with energy E per pixel.

$$S_{e/x} = \int_0^{kVp} \Phi_x(E) \left[\left\{ \eta_{phos}(E) \times P(E) \times G \times \eta_{ccd} \right\} + \left\{ \left(\left(1 - \eta_{phos}(E)\right) \times \eta_{epi}(E) \right) / 3.65\text{eV} \right\} \right] dE$$

Eq 3.10

Theoretical values for x-ray sensitivity were calculated using Eq 3.10 with $P(E)$= 52 photons per keV (Knoll), G= 0.5 (i.e. half of optical photons produced reach the CCD), η_{ccd}= 0.31 (calculated in appendix 1.), d_{epi}= 20μm using a 28kVp x-ray spectrum shown in Figure 3.8. Results are tabulated in Table 3.3.

Experimental results for the contributions from direct hits were calculated by subtracting the theoretical phosphor contribution from the experimentally obtained total sensitivity of the device.

Results shown in Figure 3.10 and Figure 3.11 reveal good agreement between experimental and theoretical results obtained for both contributions to the x-ray sensitivity.

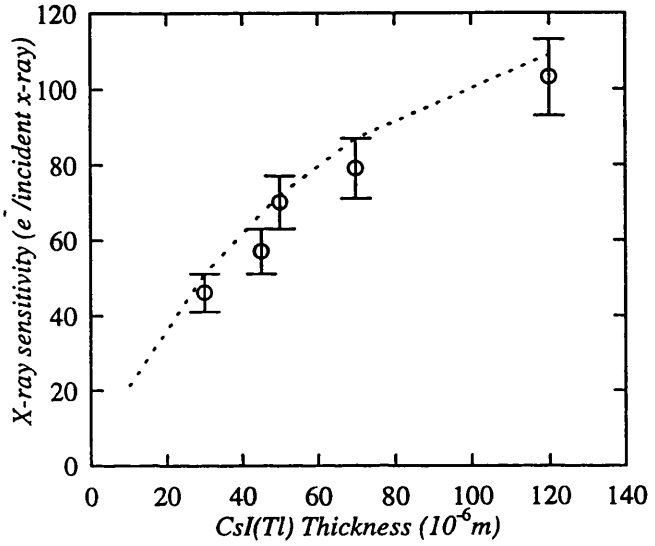

Figure 3.10 x-ray sensitivity as a function of CsI(Tl) phosphor thickness. Dashed line are data obtained from theoretical data.

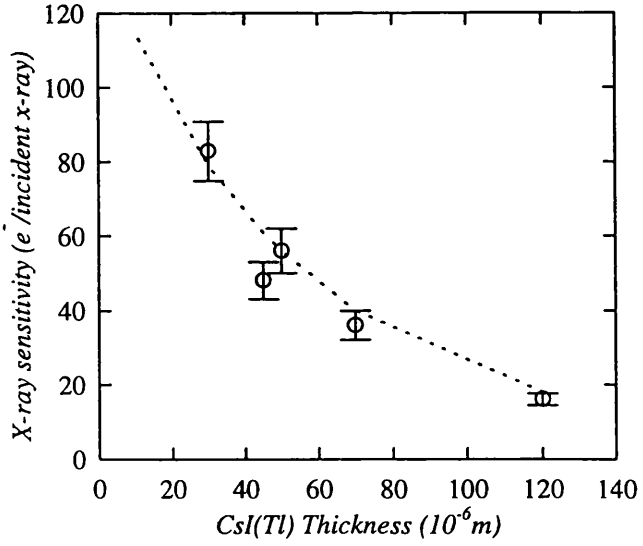

Figure 3.11 contribution to x-ray sensitivity from direct hits in the CCD for direct coated detectors. Dashed line is obtained from theoretical data

3.5.1.2 Results and discussion for fibre optic coupled detectors

The thickness' of fibre optic faceplate used in the detectors was sufficient such that there was a negligible contribution to the signal from direct hits in the CCD.

$$S_{e/x} = \int_0^{kVp} \Phi_x(E)\eta_{phos}(E) \times P(E) \times G \times T \times \eta_{ccd} dE$$

Eq 3.11

The x-ray sensitivity for these detectors is given in Eq 3.11 where T is the transmission efficiency of the fibre optic coupling between the phosphor and the CCD. Theoretical values for x-ray sensitivity were calculated for using each detector using Eq 3.11 and values of T and G tabulated in Table 3.3

For detector foMinR the value of G was calculated using Eq 3.12 (Swank 1973a) with μ = 19.45 mm^{-1}, L = 85μm, σ = 11mm^{-1}, τ = 50mm^{-1}, ρ_0 =0.9 ρ_1 = 0.7 (Nishikawa et al.1990a) and T= 0.60

$$G = \frac{\mu\tau\rho_1 \exp(-\mu L)}{1-\exp(-\mu L)} \frac{\left[2\sigma(\mu+\tau\rho_0)\exp(\mu L) - (\mu-\sigma)(\sigma-\tau\rho_1)\exp(-\sigma L) - (\mu+\sigma)(\sigma+\tau\rho_0)\exp(\sigma L)\right]}{(\sigma+\tau\rho_0)(\sigma+\tau\rho_1)\exp(\sigma L)}$$

Eq 3.12

The value of G for all CsI(Tl) based detectors (apart from detector fohama) was chosen to be 0.5, which assumed that half of all scintillation photons created reached the output face of the phosphor. To account for the reflective coating on the top surface of the CsI(Tl) layer of fohama the value of G was chosen to be 0.7(i.e. there is a contribution from photons which have reflected from the top surface).

The value of G for all 'gadox' based detectors was chosen to be 0.3 which is lower than the value used for CsI(Tl). This is because the 'gadox' phosphor is opaque (CsI(Tl) was transparent) and consequently scintillation light is lost through self absorption and reflection. A value of $P(E)$ was estimated to be 62 photons /keV for detector fo200G.

*It was found that detector fohama was 1.4 times more sensitive than detector fo70C(after correcting for their different thickness' 6%). G for detector fohama was then calculated to be $0.5 \times 1.4 = 0.7$.

For detector fo200G a value for G was chosen to match the theoretical and experimental values. A value for G of 0.28 was chosen.

The transmission efficiency T, of the fibre optic faceplate '1:1a' used in detectors fo200G, foMinR, fohama, fo130C and fo 70C was equal to 60% (obtained from manufacturers data).

The transmission efficiency T, of the fibre optic taper '1.7:1t' used in detectors ft130C and ft70C was calculated using the following Eq 3.13 (H. Liu et al. 1993) where M is the magnification of the taper n_1 and n_2 are the refractive indices of core and cladding material respectively, d is the diameter of the fibre core, D is the overall fibre diameter and F is the transmission efficiency of a single fibre. A figure of 20% was obtained with $M = 1.7$, $n_1 = 1.81$, $n_2 = 1.5$, $d = 6\mu m$, $D = 7\mu m$ and $F = 90\%$.

$$\text{Taper transmission efficiency} = \left(\frac{1}{M}\right)^2 (n_1^2 - n_2^2) \times 0.907 \left(\frac{d}{D}\right)^2 F$$

Eq 3.13

The transmission efficiency of the phosphor coated fibre optic studs used in detectors fo130C, fo70C, ft130C and ft70C was estimated to be around 75% which made the total coupling efficiency of fo130C and fo70C equal to 45% and ft130C and ft70C equal to 16%.

*

The figure for the transmission efficiency T, of EEV's fibre optic coupling used for detectors fo50C and fo50G was obtained by comparing the x-ray sensitivities of detectors dc50C and fo50C. Both detectors had phosphor coatings 50μm of CsI(Tl), so by subtracting the contribution due to direct hits from the value of sensitivity for the dc50C detector, a direct measure of the transmission efficiency of the fibre optic coupling was obtained. Errors associated with all the theoretical calculations are 10%.

From Table 3.3 it can be seen that there is generally good agreement between theoretical and experimental values of x-ray sensitivity. The discrepancy between the theoretically obtained value of 73 electrons/incident x-ray and the experimental value of 33 for fo MinR is attributed to light losses at the Min-R screen/fibre optic interface which effectively reduce the transmission efficiency of the fibre optic coupling by a further

50%. Also the use of the carbon fibre cassette see chapter 2 will also act to reduce the quantum detection efficiency.

Theoretical values are all lower for the fibre optic coated detectors, this is attributed to light losses at the CCD/fibre interface and phosphor/fibre interface.
The discrepancy between values for fo50G is attributed to the poor quality of the coating, the coating was flaking in areas and there was not a good bond between the coating and the fibre optic..

Table 3.3 x-ray sensitivities for detectors under investigation.

Detector id.	*Quantum detection efficiency*	*X-ray sensitivity e⁻/incident x-ray (expt)*	*T*	*G*	*X-ray sensitivity e⁻/incident x-ray (Theory)*
dc120C	0.84	119	-	0.5	117
dc70C	0.68	115	-	0.5	117
dc50C	0.57	135	-	0.5	118
dc45C	0.51	105	-	0.5	118
dc30C	0.40	101	-	0.5	110
fo130C	0.86	45	0.45	0.5	56
fo70C	0.68	39	0.45	0.5	44
fo50C	0.57	23	0.3	0.5	24
foMinR	0.79	33	0.60	0.3	68
fohama	0.72	63	0.45	0.7	66
fo200G	0.994	72	0.6	0.2	72
fo50G	0.80	19	0.3	0.2	24
ft130C	0.86	19	0.16	0.5	21
ft70C	0.68	14	0.16	0.5	17

3.5.2 Detector dynamic range

The dynamic range of the system was estimated using Eq 3.14. The estimate is an overestimation and neglects any reduction in dynamic range caused by spurious dark signal generation. That said a 1s integration time will only reduce the dynamic range by 1.5% for the 15_11 CCD. Results are presented in Table 3.4

$$\text{Dynamic range} = \frac{\text{fullwell capacity} \times \text{Quantum detection efficiency}}{\text{X - ray sensitivity}}$$

Eq 3.14

Table 3.4 dynamic range estimates of detectors

Detector Id.	*Dynamic range*	*Detector Id.*	*Dynamic range*
dc120C	4950:1	fo50C	7300:1
dc70C	4140:1	foMinR	17000:1
dc50C	1266:1	fohama	8000:1
dc45C	3400:1	fo200G	9600:1
dc30C	1180:1	fo50G	13500:1
fo130C	13300:1	ft130C	13500:1
fo70C	12200:1	ft70C	14000:1

These figures for dynamic range refer to the detector capability, obviously when the signal is digitised to 12bits the dynamic range is limited to 4095:1.
Research into the dynamic range requirements for digital mammography has shown that a value of around 3000:1 is needed (Maidment 1994).

3.6 System noise

The four main sources of noise in the system were found to be inherent electronic noise from the camera board and the CDS unit σ_{elec}, fixed pattern noise due to detector non-uniformities σ_{fpn}, x-ray quantum noise σ_x, and dark signal noise σ_d. For directly coated detectors there is an additional noise source which arises from fluctuations in the no. of direct hits in the CCD σ_{epi}.

3.6.1 System electronic noise

To obtain a measurement of the inherent system noise, images were obtained without any detectors inserted in the camera board. Two successive images were taken and one subtracted from another, the magnitude of the noise was then calculated by computing the root of the mean of the squares of the pixel values and dividing by a factor of $2^{0.5}$.

$$\sigma^2_{elec} = \sigma^2_{CDS} + G\sigma^2_{CAM}$$

Eq 3.15

The system has only two major noise sources the camera board and the CDS unit and the total noise can be expressed as in Eq 3.15

$$\sigma_{CAM} = \frac{\sigma_{TOTAL}}{\sqrt{G}}$$

Eq 3.16

where σ^2_{TOTAL}, σ^2_{CDS}, σ^2_{CAM} are the total, CDS unit and camera board noise respectively and G is the system gain. For large gains the contribution from the CDS unit becomes negligible so that the noise due to the camera board is given in Eq 3.16.

Table 3.5 Inherent system noise measurements.

CDS Gain	*No. of electrons/ADU*	*Total noise (ADU)*	*Noise equivalent electrons*
1	306	2.3	704
2	104	3.8	395
3	39.1	8.9	348

Table 3.5 shows measurements of noise for three CDS gain settings. The contribution from the camera board and CDS unit was estimated to be ~320 and ~627 noise equivalent electrons respectively (assuming an electron per ADU conversion factor of 306 for CDS gain 1).

3.6.2 Fixed pattern noise

For highly illuminated images fixed pattern noise can be the dominant noise source. It arises from variations in pixel gain and dark charge generation.

Fixed pattern noise was almost completely removed using a simple algorithm summarised in Figure 3.12. An average of 10 dark images (detector non illuminated) was calculated this provided the dark current offset image. An average of 10 uniformly illuminated, x-ray exposed images was calculated and the dark current offset was subtracted to provide an image of the pixel gain nonuniformities. Each image was then corrected by subtracting the dark current offset image, dividing by the image of pixel gain non-uniformities and multiplying by the average ADU value of the original image.

Correcting for fixed pattern noise resulted in ~3.7 reduction in image noise for fibre optic coupled detectors and ~1.3 reduction for directly coated detectors.

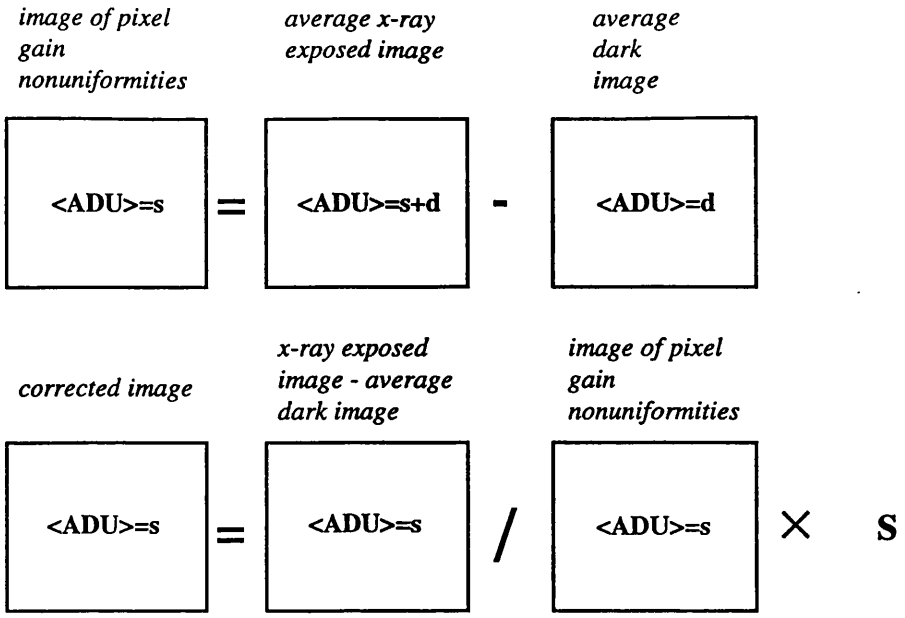

Figure 3.12 schematic of correction for fixed pattern noise. **<ADU>** means average ADU value, **s** is the signal due to illumination only, **d** is the signal due to dark current generation.

3.6.3 Dark signal noise

$$S_d = Jq_e^{-1}A_{pix}t \quad \text{electrons}$$

Eq 3.17

The dark current signal per pixel is given by Eq 3.17 where J is the dark current for the detector, q_e is the electron charge, A_{pix} is the pixel area and t is the integration time. The dark current noise is given in Eq 3.18.

$$\sigma_d = \sqrt{Jq_e^{-1}A_{pix}t} \text{ electrons}$$

Eq 3.18

Dark signal was measured as a function of integration time by shielding the detector from any illumination and taking image s for various integration times. The results of these measurements are shown in Figure 3.13. From a linear regression on the data $Jq_e^{-1}A_{pix}$= 13×10^{-4} electrons/pixel/second. The pixel area of the device is 7.29×10^{-2} mm^2, therefore the dark current was J=0.3nAcm^{-2}.

$$\sigma_d = \sqrt{\sigma^2_{meas} - \sigma^2_{elec}}$$

Eq 3.19

The noise contribution from dark current was measured as a function of integration time. This was done by subtracting two successive images from each other, the noise was then calculated by computing the root of the mean of the square of the pixel values and dividing by $2^{0.5}$. The contribution to the noise from dark current was calculated by subtracting the electronic noise contribution using Eq 3.19 where σ_{meas} is the measured noise. The results of the measurement are shown in Figure 3.14, together with theoretical results obtained using Eq 3.18 with J= 0.3 nA/cm^2.

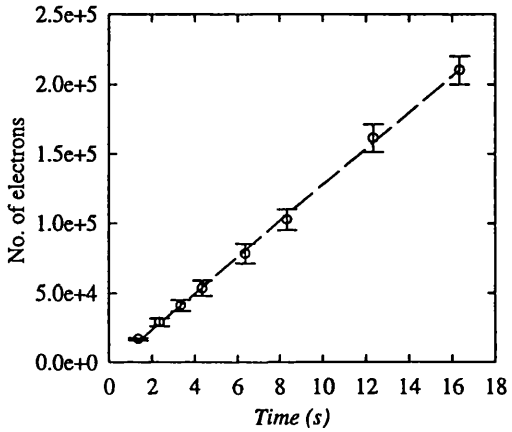

Figure 3.13 dark signal (per pixel) as a function of integration time for detector dc120C at 298K. Dashed line is data from a regression.

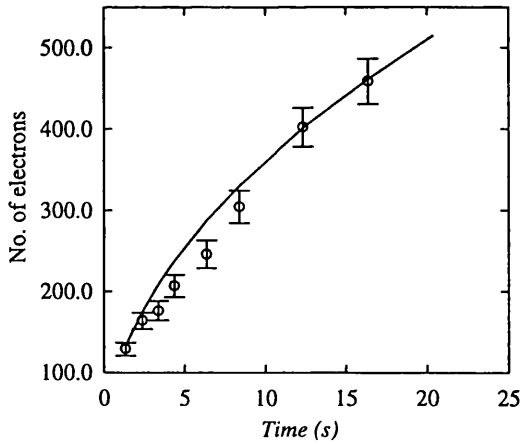

Figure 3.14 dark signal noise as a function of integration time for dc120C (298K). Solid line is obtained from theoretical data.

3.6.4 X-ray quantum noise

X-ray quantum noise was calculated using Eq 3.20, where S_X is the x-ray signal and all other symbols are defined in sections 3.5.1.1 and 3.5.1.2.

$$\sigma_x = \sqrt{\frac{S_x}{\Gamma_{phos}}(\eta_{phos})} \times P(E) \times G \times T \times \eta_{ccd} \text{ electrons}$$

Eq 3.20

3.6.5 Direct hit noise

For directly coated detectors there is an additional noise source which arises from fluctuations in the number of direct hits per pixel in the CCD. It was calculated using Eq 3.21, where all symbols are defined in sections 3.5.1.1 and 3.5.1.2.

$$\sigma_{epi} = \sqrt{\frac{S_x \times \overline{E}}{\Gamma_{epi} \times 3.65eV}} \text{ electrons}$$

Eq 3.21

3.6.6 Results of detector noise measurements

Table 3.6 Noise contributions for detectors dc120C and fo70C. All figures are expressed in ADU with no. of e⁻/ADU = 306 for dc120C and =39 for fo70C.

Detector	S_x	S_d	σ_{tot}	σ_{cor}	σ_{fpn}	σ_x	σ_d	σ_{elec}	σ_{epi}
dc120C	1465	330	74	58	46	2.3	0.6	2.4	58
fo70C	965	220	34	9.2	33	5.0	2.4	7.3	-

Table 3.6 shows values for total noise σ_{tot} and noise contributions for two typical detectors(direct coated device and a fibre optically coupled device) with x-ray signal S_x, and dark current signal S_d, all measured in terms of rms pixel fluctuations.

Results show that for detector fo70C fixed pattern noise is the dominant noise source, however once the image is corrected (see section 3.62) then electronic noise is dominant.

For the directly coated detector dc120C fluctuations in the number of 'direct hits' in the CCD is the dominant noise source and it can be seen it remains so after image correction.

3.7 Dark current reduction methods

Methods for reducing dark current and the nose associated with it include

- Increasing the substrate potential until inversion occurs under two of three electrodes of a pixel.(Saks 1980)
- Charge pumping or dithering (Burke et al 1991)
- Cooling the CCD

3.7.1 Increasing substrate potential

When the substrate potential is increased to about 9 volts the surface under a low level gate (0V) the substrate potential now equals the potential at the silicon surface and holes can flow from the channel stops into the surface region. The presence of these holes effectively inverts the surface from n-type to p-type, and the contributions to dark current from the surface states are suppressed.

The variation of dark signal as the substrate potential is increased is shown in Figure 3.15. Increasing substrate potential from 6V to 9V decreases dark signal by a factor of ~2.6.

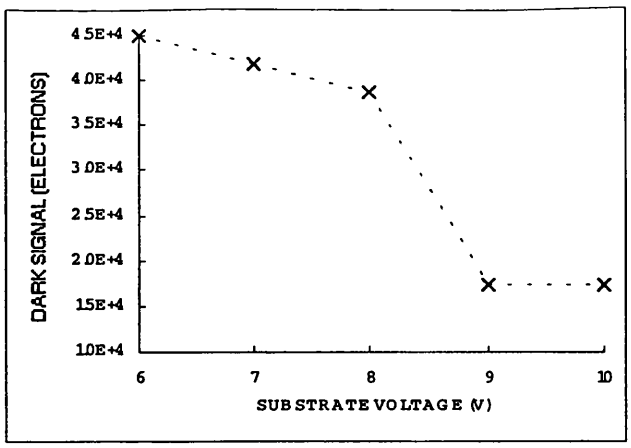

Figure 3.15 Dark signal as a function of substrate voltage for 15_11 CCD at 293K (1second integration time).

3.7.2 Charge pumping or dithering

In order for a buried channel CCD to image correctly at least one pixel electrode needs to be held high to isolate separate charge packets. Burke et al (1991) have shown that when a surface is switched from inversion to depletion, the surface generation rate remains low for a characteristic time period before recovering to its steady state value. This means that the interface state dark current can be dynamically suppressed by periodically switching charge packets between electrodes and keeping them inverted when not storing charge. Using the charge pump scheme illustrated in Figure 3.16 led to ~2 reduction in dark current for the 02_06 device.

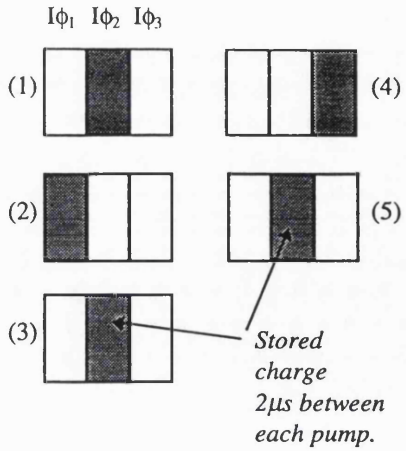

Figure 3.16 Charge pumping scheme used for CCD02_06 device

Charge pumping can only be used if the CCD is used in an signal integrating mode or in frame transfer CCDs, it is not applicable to CCDs when operated in TDI mode due to the continuous nature of the operation. For this reason no charge pumping was used with the 15_11 devices.

3.7.3 Cooling the CCD

Reducing the temperature of the CCD reduces the thermal generation of signal carriers produced in the CCD. The CCD was cooled using a peltier cooling system described in chapter 2. 15_11 CCDs could be cooled to around 293K and 02_06 CCDs to around 283K. The difference in the temperatures to which the CCDs can be cooled can be explained because the 15_11 device is about 1.8 times larger in area than the 02_06 device.

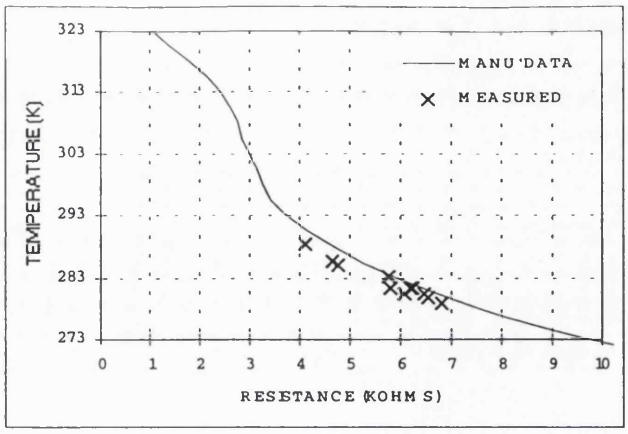

Figure 3.17 Themistor resistance as a function of temperature.

Figure 3.17 shows the variation of thermistor resistance with temperature, temperature was measured using a platinum resistance thermometer in contact with the cooling top plate. The measured temperatures are all lower than manufacturers data. This is probably due to the thermal contact between the thermometer not being 100% efficient. Thermal conducting fluid was used between the CCD and the top cooling face to ensure good thermal contact. Figure 3.18 shows dark signal as a function of temperature for a 15_11 CCD.

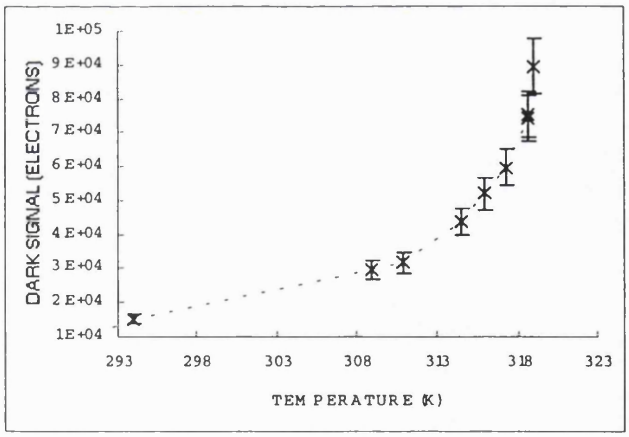

Figure 3.18 Dark signal as a function of temperature for a 15_11 device (substrate poential=9V).

Previous work has shown that dark charge generation mainly arises from generation at surface states (90%) (Torren and Bisshop 1994).By using an inverted CCD chip and using an appropriate charge pumping clocking scheme charge generation at surface states can be removed charge current can be virtually eliminated.

When CCDs are cooled to temperatures approaching the dew point it is necessary to remove all moisture from its environment to prevent condensation causing a short on the chip. This can be achieved by having a constant flow of dry nitrogen over the CCD. Results show that dark current can be reduced by a factor of ~10 by cooling to 293K (with an 'inverted' CCD).

3.8 Summary and conclusions

In this chapter the tests and calibrations of a prototype CCD x-ray imaging system have been described. Tests of system stability show that dark current from a CCD takes about 10 minutes to reach a steady value as the CCD heats up, but this time can be reduced to 4 minutes if the CCD is cooled.

The system has been calibrated in terms of the number of electrons produced in a pixels of the CCD per ADU value in the digitised image. This calibration combined with the ADU per output voltage enabled figures for the charge sensitivity of each CCD to be calculated. Values of charge sensitivity obtained agree well with values reported in manufacturers data sheets.

The imaging system is shown to be linear with respect to optical illumination and x-ray irradiation and values for the full well capacity of the CCD pixel was found to be 700k electrons and 300k electrons for the 15_11 CCD and 02_06 CCD respectively.

The sensitivity of the detectors to x-ray irradiation was calculated in terms of the number of electrons produced in a pixel of the CCD per incident x-ray. Results show good agreement with simple models presented.

Of the detectors used the directly coated detectors are the most sensitive to x-ray irradiation. This is due in part to direct hits in the epitaxial layer of the CCD and because there is no light loss due to intermediate optical coupling between the phosphor and the CCD. Both contributions to x-ray sensitivity, for these detectors have been

characterised. X-ray sensitivity should increase with the thickness of phosphor used in the detector, however as the phosphor thickness decreases the probability of a "direct hit " increases such that the x-ray sensitivity of the detectors is approximately constant. A typical value for x-ray sensitivity is 120 electrons per incident x-ray for a 28 kVp Mo-Mo x-ray spectrum.

The fibre optically coupled detectors have a lower x-ray sensitivity compared to directly coated detectors. This due to the losses of light in the fibre optic coupling and because there are negligible contributions to the signal from direct hits in the CCD.

Results show moderate agreement between experimentally obtained results and theoretical results obtained from models. X-ray sensitivity for these detectors depends upon the transmission efficiency of the optical coupling and the thickness of phosphor used. X-ray sensitivity can be seen to increase with phosphor thickness for all the fibre optically coupled detectors. Values for x-ray sensitivity for these detectors is lower than directly coated detectors by as much as a factor of ~2. A typical value is 45 electrons per x-ray for detector fo130C.

It is noted that an x-ray sensitivity of detectors fo130C, fo70C, ft130C and ft70C can be increased by 25% by coating the phosphor directly onto the fibre optic faceplate and thereby 'losing' the fibre optic stud.

The noise in the system has been characterised in terms of rms. pixel fluctuations. Results show that fixed pattern noise is a major contribution to image noise but can be virtually eliminated by correcting for pixel offset and gain using reference images. This correction reduces image noise by a factor of ~ 4 and ~ 1.3 for fibre optically coupled detectors and direct coated devices respectively.

For directly coated detectors the major noise source arises from fluctuations in the number of direct hits in the CCD. The effect of this noise source on image quality is investigated in chapter 5.

For fibre optically coupled devices operated with high irradiance levels the major noise source arises from x-ray quantum fluctuations, however for lower irradiance electronic noise dominates and may be the dominant contribution for the irradiance levels used in mammography. This is investigated further in chapter 5

CHAPTER 4

4. Detector evaluation

This chapter describes the methods used for evaluating the imaging performance of the detectors. The quality of an image depends strongly upon spatial resolution. The use of modulation transfer function (MTF) is widespread in characterising the resolution properties of imaging systems. When determining the MTF of digital imaging systems care is needed to avoid aliasing effects caused by discrete sampling (M. Giger, 1984). The MTF of all the devices used was determined using a method similar to those developed by H. Fujita (1992) and S. Reichenbach (1991).

Theoretical models of MTF including effects due to direct hits in the CCD and light attenuation in the phosphor screen are discussed. Comparisons between MTF and limiting spatial resolutions, measured with a star pattern are discussed.

Image noise is another factor which determines the quality of images. The Wiener spectrum or noise power spectrum (NPS) provides a measure of the magnitude and the spatial distribution or texture of the noise. Methods of measurement are discussed and results are presented.

It is widely accepted that there is an intimate relationship between an observer's ability to detect an object in an image and the signal to noise ratio (SNR) associated with that object. A review of the work done in this field can be found in a volume edited by Biberman (1973) and a text by Rose (1972). The MTF of a system describes how signal is passed through an imaging system in the absence of noise. The spatial frequency dependent detective quantum efficiency DQE(f) describes how a system passes signal to

noise ratio and is a better measure of the quality of images that will be produced from a detector. The calculation of spatial frequency dependent DQE(f) is described and results are presented.

4.1 Spatial resolution of a CCD based detector.

The spatial resolution of a CCD based detector is dependent upon the following factors

- Pixel dimensions

The width of a pixel can be a determining factor in the limiting spatial resolution of the CCD. An ideal pixel has a uniform response across its area and has an MTF given in Eq. 4.1.(taken from the Fourier transform of a 'top hat' function)

$$MTF_{pixel} = SIN(\pi\, d_p\, f)/(\pi\, d_p\, f)$$

Eq. 4.1

and has an associated cut-off and Nyquist frequency of $1/d_p$ and $1/2d_p$ respectively, where d_p is the width of the pixel and f is the spatial frequency.

The MTF of a CCD is dependent upon how much charge is stored in the pixels due to the reduced potential profile of a pixel as charge is stored. For this reason all MTF measurements were carried out with the CCD pixels 'half filled' to allow comparison of MTF's from different detectors.

- Spreading of generated optical photons

This was found to be the dominant factor in degrading spatial resolution by Martinez (1994), who measured MTF's of CCD based detectors with fibre optic face-plates and CsI(Tl) phosphors. In some phosphor screens the spreading of optical photons is reduced by using light absorbing dyes and by using structured screen such as CsI(Tl).

- fibre optic fibre dimensions

Optical cross talk where light scatters from one fibre to another , can cause a significant degradation in MTF. This effect can be removed by the use of extra mural absorber or EMA. All fibres used in this project have EMA so this is not a problem.

The MTF of a fibre optic faceplate is related to the diameter of a single fibre and is given in Eq. 4.2 where d_f is the diameter of the fibre.

$$MTF_{fibre} = SIN((\pi d_f f)/(\pi d_f f)$$

Eq. 4.2

A single fibre has associated with it a finite numerical aperture which restricts the maximum angle relative to the normal, from which light is accepted. Experimental model have shown this effect increases MTF (Westomore and Cunningham 1994). This effect is modelled in a later section.

4.2 Modulation transfer function theory

The modulation transfer function is defined as the ratio of the output to the input modulation of a sinusoidal input, normalised at zero spatial frequency and is given in Eq. 4.3 (Johns and Cunningham 1983). Practical measurements involve the input signal being generated at different frequencies with the same modulation i.e. $M_{in}(f)=M_{in}(0)$ for all f.

$$MTF(f) = \frac{M_{out}(f)}{M_{in}(f)} \bullet \frac{M_{in}(0)}{M_{out}(0)}$$

Eq. 4.3

This means that the definition of MTF(f) reduces to Eq. 4.4 which means that the MTF can be determined simply by measuring the modulation of the output signal.

$$MTF(f) = \frac{M_{out}(f)}{M_{out}(0)}$$

Eq. 4.4

In practise it is not easy to generate a sinusoidal variation of x-ray fluence. However a way around this problem is to measure the modulation of the system using a square wave pattern which is much easier to fabricate. From this data an estimation of the MTF can be calculated using a correction function defined in Eq. 4.5 (Coltman 1954), where $T_s(f)$ is the measured square wave response, with k=1,3,5,... and B_k=1,0 or -1 according to Eq. 4.6 where *m* is the total number of primes into which k can be factored, and *r* is the number of different prime factors in *k*.

$$MTF(f) = \frac{\pi}{4}\sum_k B_k \frac{T_s(kf)}{k} = \frac{\pi}{4}\left[T_s(f) + \frac{1}{3}T_s(f) + \ldots\right]$$

Eq. 4.5

$$B_k = \begin{cases} (-1)^m.(-1)^{(k-1)/2} & \text{if } r = m \\ 0 & \text{if } r < m \end{cases}$$

Eq. 4.6

Another method used for measuring MTF is based upon the Fourier transform of the line spread function (LSF). The LSF can be obtained directly from an image of a thin slit (thinner than the pixel dimensions) which is corrected for the width of the slit or from an image of a sharp straight edge which gives the edge response function (ERF) which is then differentiated to give the LSF. The following work details of 3 methods of measuring MTFs are presented which are summarised as follows:

- Optical measurement - It is very difficult to obtain a slit that is thin enough and made out of appropriate material thick enough to prevent transmission of x-rays. The use of optical illumination enables a slit to be demagnified onto the surface of the CCD and enable the LSF to be obtained directly. The measurement of MTF was repeated using a sharp, straight edge to obtain the LSF by differentiating the ERF and a check on the consistency between these measurements was obtained.

- X-ray measurement using edge response technique.
- X-ray measurement using square wave technique. This method was used to confirm/verify results obtained with the edge response technique.

With all discrete imaging devices there are problems caused by measuring the MTF (using spread methods) caused by undersampling. To overcome this an extended edge technique has become widely used to determine the pre-sampling MTF. The method employed involves the knife edge being aligned slightly off-perpendicular to the pixel columns as shown in Figure 4.1(a). Figure 4.1(b) shows the edge responses and sample points for this alignment. By superimposing these edge responses a composite edge response function (ERF) is obtained with a smaller sampling distance, shown in Figure 4.1(c).

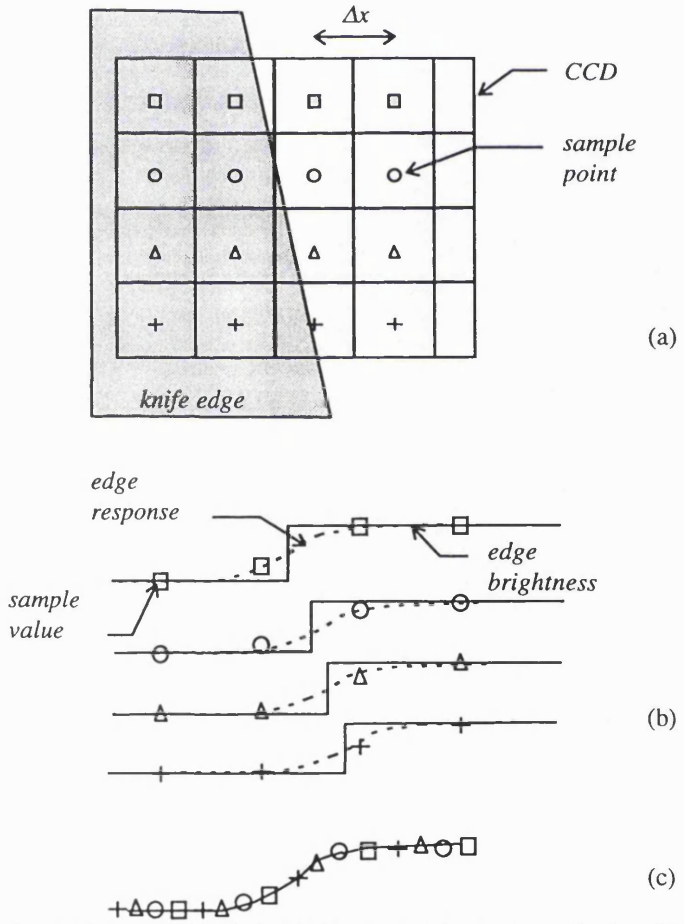

Figure 4.1(a) sampling grid with shifted knife skewed from perpendicular. (b) knife edge shift for successive lines. (c) composite ERF.

The composite ERF is differentiated to obtain the line spread function (LSF). The MTF is obtained by computing the Fourier transform of the LSF and normalising.

4.2.1 Methods and materials for calculating the MTF (ERF measurement)

A 0.5mm thick tantalum knife edge was placed in contact with the detector with its edge slightly off perpendicular to the pixel columns as in Figure 4.1(a). The angle of the edge relative to the columns was chosen to ensure that a sufficient number of sample points were obtained in the composite LSF. In order to minimise the effect of the focal spot on the detector MTF measurements the x-ray tube was placed at about 120cm from the detector plane.

The tube potential was set to 28kVp and the current was set to a value such that the signal in an uncovered pixel of the CCD was half the full well capacity of the device. This ensured that effects on MTF due to signal level in the pixel are identical for each detector and all images are x-ray quantum noise limited. The integration time of the CCD was set to 1 second.

A set of 6 images of the edge were taken and averaged to reduce quantum noise and electronic noise due to fixed frequency 'pick up'. The averaged image was corrected for pixel gain and offset variations.

A computer program was written to calculate the composite LSF from the averaged image and calculate the MTF. The steps used in the program are summarised below.

1. Calculate LSF for each line in the image.
2. Find the line l_{max}, for which the peak LSF value occurs (the peak LSF corresponds to the alignment of the edge being over the boundary between 2 pixels).

3. Find the position of the edge in each line. This was done by centroiding the LSF over the 5 values centred on the maximum using Eq. 4.7 where E is the position of the edge, S_n is the signal in pixel number. n.

$$E = \sum S_n n \Big/ \sum n \qquad \textbf{Eq. 4.7}$$

4. Calculate the displacement of the edge between consecutive lines. Since the edge is straight the position of the edge in the n^{th} line E_n, is given by Eq. 4.8 where E_1 is the position of the edge in the first line, l is the line number and m is the edge displacement. A least squares fit is applied to the data to calculate l.

$$E_n = ml + E_1 \qquad \textbf{Eq. 4.8}$$

5. Form the composite ERF by combining individual ERFs from line l_{max} up to line (l_{max}+1/m).
6. Resample composite ERF to give an effective sampling distance of 1/10×pixel size.
7. Differentiate the composite ERF to give the composite LSF.
8. Calculate discrete Fourier transform of composite LSF and normalise to give MTF.

The MTF values were corrected for the effect of the finite element differentiation using the method described by Cunningham (1987).

4.2.2 Optical MTF measurement of CCD.

The MTF of the 15_11 CCD was determined using the experimental set-up shown in Figure 4.3. A 50μm slit is demagnified using a 10× microscope objective to produce a 5μm slit in the CCD image plane. The slit was set at a slight angle to the row direction (to obtain column MTF) in the CCD and an image was taken. This technique requires no

intermediate step to transform the ERF to the line spread function LSF(X) as it is obtained directly. The MTF is obtained using the method described above and is corrected for the size of the slit using Eq. 4.9.

$$MTF_{CCD}(f) = MTF_{expt}(f)/SINC(\pi f \times 0.005)$$

Eq. 4.9

Figure 4.2(a) shows experimentally obtained LSFs for the 15_11 CCD. The composite LSF with effective sampling distance equal to 2.7μm is shown in Figure 4.2(b).The composite LSF was Fourier transformed to obtain the MTF.

The procedure was repeated to obtain the row MTF by changing the orientation of the slit. MTFs were determined for the 15_11 device, 15_11 device with fibre optic coupling, 02 device and 02 device with fibre optic taper.

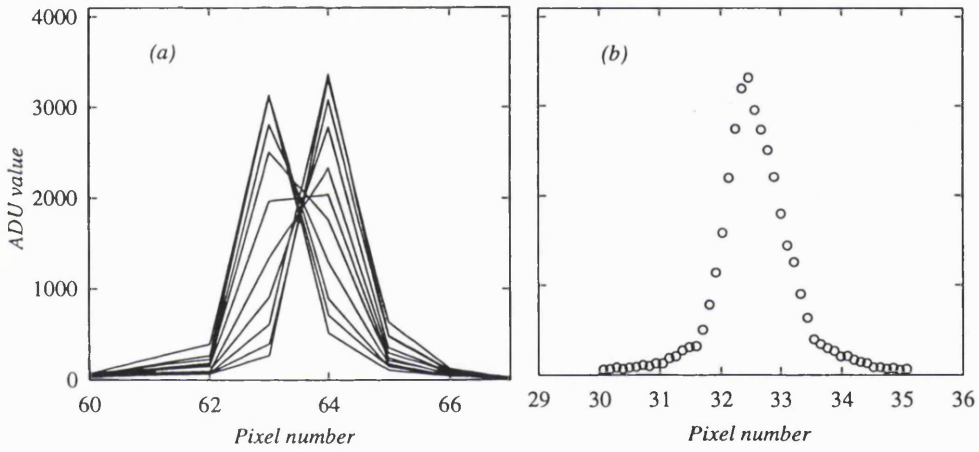

Figure 4.2 (a) successive LSF's along rows showing the slit position shift. (b) composite LSF for the 15_11 CCD. Effective sampling distance is ~0.1×pixel size.

4.2.2.1 Comparison of the slanted knife edge method and the slanted slit method

A comparison of the slanted knife edge method and the slanted slit method was made with the fibre optic coupled 15_11 CCD. The slanted knife edge was placed in contact with the detector and the detector was placed in a field of parallel uniform illumination. An image was taken and the MTF was obtained as described in section 4.2.

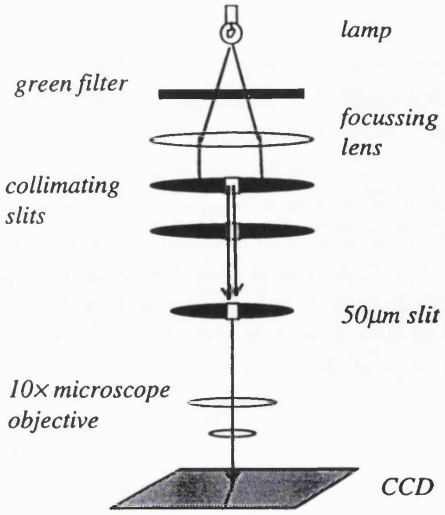

Figure 4.3 experimental setup for measuring the MTF of the CCD imaging array.

4.2.2.2 Results for optical MTF

From Figure 4.4 it can be observed that the MTF for the 15_11 CCD in the column and row direction are equivalent and agree broadly with the theoretical MTF due to the square sampling aperture which is given by Eq. 4.10 where SINC(π x) =SIN(π x)/(π x) and p is the pixel size in millimetres. Errors associated with each MTF measurement are estimated to be 2% at 5 lp/mm and 5 % at 10 lp/mm and higher.

$$MTF_{pixel} = SINC(\pi f p)$$

Eq. 4.10

Similar results were obtained for the fibre optically coupled 15_11 CCD. The MTF in the column and row direction are equivalent and agree broadly with the theoretical MTF due to the square sampling aperture. The knife edge technique gives similar results to the angled slit technique (within experimental errors).

Comparing results for the 15_11 CCD and the fibre optically coupled 15_11CCD it can be seen that there is no appreciable difference in MTF that could be attributed to the fibre optic coupling.

Also shown in Figure 4.4 are row and column MTF's for an 02_06 CCD coupled to a 1.7× magnification fibre optic taper. Also shown is the theoretical MTF for the effective pixel size of 38μm.

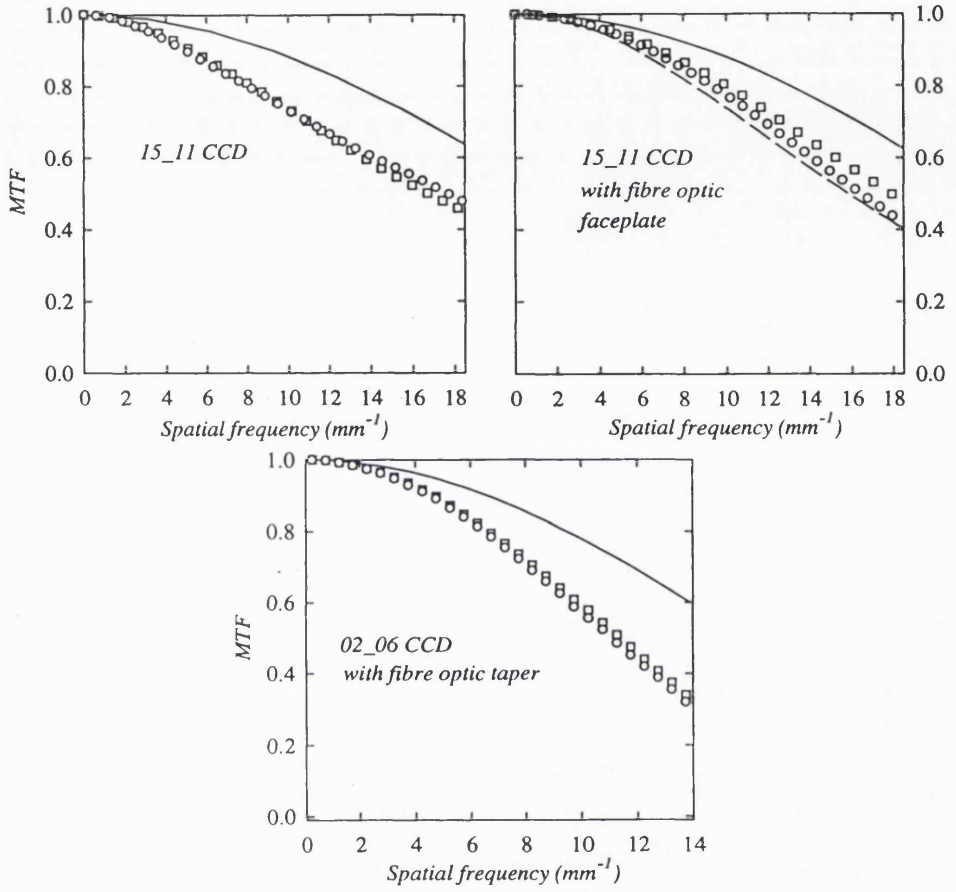

Figure 4.4 Optical MTFs for detectors. Squares represent MTF in column direction. Circles represent MTF in row direction. Solid line represents geometrical component of the MTF due to the square sampling aperture of the CCD. Dashed line is MTF in row direction obtained using knife edge technique.

4.2.3 MTF measurement using square wave approximation

Images of a Type 9 star phantom were used to measure the square wave response of each detector and an estimation of the MTF of the detector was obtained using the previously mentioned correction. The phantom was placed directly on top of the detector to eliminate any possible geometrical unsharpness, images were obtained using

the same exposures as used for the MTF measurements. All images were corrected for gain non-uniformity's and offset.

The phantom contains 4 groups of 14.5 line pairs each. A single line pair has an angular aperture of 2°, therefore there are 180 line pairs in a whole circle. At the external diameter (45 mm) of the pattern the spatial frequency is 180lp /(π 45mm) = 1.27 lp/mm. the internal diameter is 3.2 mm giving a maximum spatial frequency of 17.9 lp/mm.

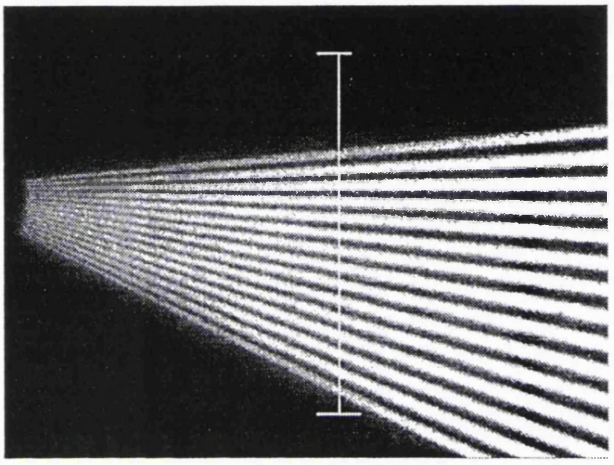

Figure 4.5 image of star pattern used to obtain square wave response function

Figure 4.5 shows an image of the star phantom obtained with detector fo50C. An example profile from the image is shown in Figure 4.6 corresponding to a spatial frequency of 3.7 lp/mm.

$$M_{out} = \frac{S_{max} - S_{min}}{S_{max} + S_{min}}$$

Eq. 4.11

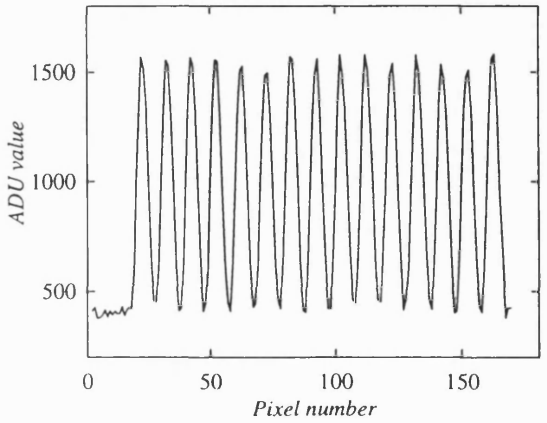

Figure 4.6 profile taken from an image of star phantom.

The profile shown in Figure 4.6 was taken from the image shown in Figure 4.5. In this image the frequency is reduced at the edges of the profile for this reason only the central 6 line pairs were used to calculate mean values of S_{max} and S_{min}. The amplitude modulation was calculated according to Eq. 4.11 and to reduce uncertainties the average value was found from five images. Uncertainties in estimating the spatial frequency are considered negligible. Errors on the values of MTF were calculated from fluctuations in amplitude modulation across the profile.

A four term expansion of Eq. 4.5 was used to obtain an estimate of the MTF. Figure 4.7 shows the MTF of detector fo70C obtained using the edge response method and the square wave estimation. It can be observed that results from both measurements show good agreement and this was the case for all the detectors in this study.

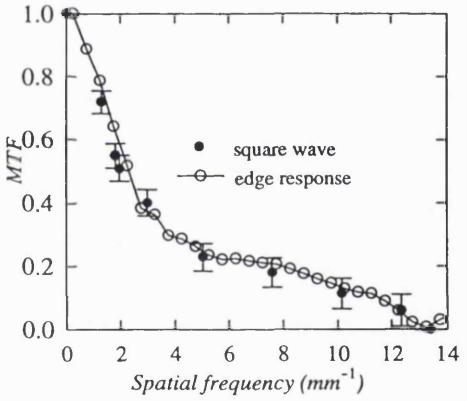

Figure 4.7 MTF of detector fo70C measured using edge response method and square wave response estimation.

4.2.4 Theoretical models for detector MTF

The use of theoretical models of MTF enables the investigation of:

- The dominant factor in degradation of spatial resolution (phosphor thickness, pixel size, etc.)
- The effects of direct hits upon MTF.
- The effect of fibre optic numerical aperture upon MTF.
- The effect of columnar structure in CsI(Tl) phosphors.

- If models are accurate they can be used to produce MTFs of hypothetical detector configurations.

Theoretical MTF models of thin film phosphors have been developed by Swank (1973a) and Nishikawa (1992). The model for the MTF of a phosphor layer has been derived to account for contributions to the signal from direct hits in the CCD. An outline of the model is given below:

- An expression for the light emitted per unit solid angle is (taken from Barret and Swindell) used to derive an expression for the PSF(X,Y).
- The PSF is integrated along the Y dimension to give an expression for the LSF(X).
- The LSF(X) is Fourier transformed and normalised to give the MTF(f).

4.2.4.1 MTF of thin layer phosphors

The following assumptions were used:

1. X-ray flux, defined by $\Phi_x(X',Y')$, is incident perpendicular to the phosphor plane.
2. The phosphor is homogeneous with no internal structure and infinite in the X-Y plane.

$$d\phi(X,Y,Z,E) = \frac{dN\cos\theta}{4\pi L^2}$$

Eq. 4.12

3. When an x-ray interacts all its energy is assumed to be deposited locally.
4. The scintillation light produced is emitted isotropically with a distribution defined by $\Phi(X,Y)$, as shown in Figure 4.8. The light emitted per unit solid angle is given in Eq. 4.12 where L is the distance the scintillation light travels through the phosphor before being detected, where $L^2 = (X-X')^2 + (Y-Y')^2 + (d_0 - Z)^2$, dN is the total amount of scintillation light emitted from an x-ray absorbed at Z in a thin slice of phosphor dZ, given by Eq. 4.13,

$$dN = \exp[-\mu_{phos}(E)Z]m(E)\mu_{phos}(E)\,dX'\,dY'\,dZ$$

Eq. 4.13

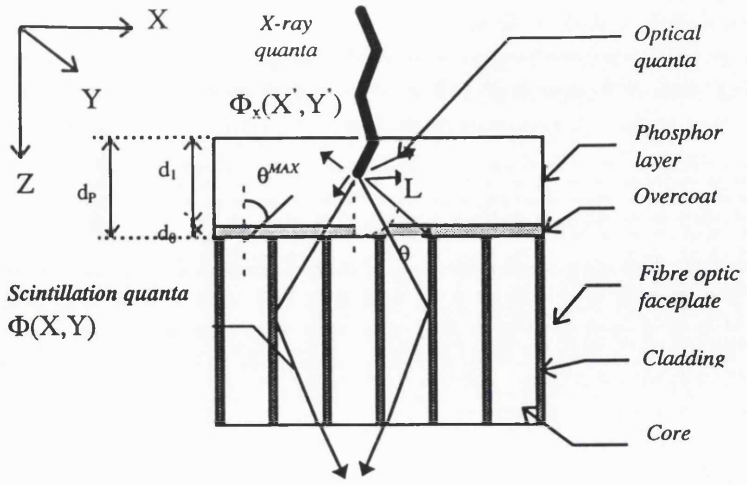

Figure 4.8 diagram of scintillation process

where $\mu_{phos}(E)$ is the photoelectric absorption coefficient of phosphor for an x-ray energy E, $m(E)$ is the scintillation light gain, $m(E)=gE$,where g is the number of scintillation photons produced per keV of energy deposited in the phosphor. E is the incident x-ray energy in keV, d_0 is the thickness of the overcoat, and d_p is the overall phosphor thickness.

The scintillation light distribution is found by integrating over all X' and Y' (assuming phosphor plane to be infinite) see Eq. 4.14.

$$\Phi(X,Y,Z,E) = \int_0^{kVp} \frac{\mu_{phos}(E)m(E)}{4\pi} \int_0^{d_p-d_o} \exp(-\mu_{phos}(E)\,Z)\cos\theta dZdE \frac{\int_{-\infty}^{\infty}\int_{-\infty}^{\infty} \Phi_x(X',Y')dX'dY'}{L^2}$$

Eq. 4.14

The scintillation light distribution becomes a point spread function by assuming the incident x-ray distribution is a delta function, the x-ray distribution is given in Eq. 4.15

$$\Phi_x(X',Y') = \delta(X)\delta(Y)$$

Eq. 4.15

which gives Eq. 4.16

$$PSF(X,Y,Z,E) = \int_0^{kVp} \frac{\mu_{phos}(E)\, m(E)}{4\pi} \int_0^{d_p - d_0} \exp(-\mu_{phos}(E)Z)\cos\theta dZdE \frac{\int_{-\infty}^{\infty}\int_{-\infty}^{\infty}\delta(x)\delta(y)dX'dY'}{L^2}$$

Eq. 4.16

which gives the average point spread function (Eq. 4.17).

$$PSF(X,Y,Z,E) = \int_0^{kVp}\int_0^{d_p} \frac{\mu_{phos}(E)m(E)}{4\pi} \frac{\exp(-\mu(E)Z)(d_p - Z)}{(X^2 + Y^2 + (d_p - Z)^2)^{3/2}} dZdE$$

Eq. 4.17

$$LSF(X,Z,E) = \int_{-\infty}^{\infty} PSF(X,Y,Z,E)dY$$

Eq. 4.18

The line spread function (LSF(X)) is found by integrating over all *Y*, given by Eq. 4.18.

4.2.4.2 Modelling the effect of direct hits on MTF

The following assumptions were used:

- The signal due to direct hits is given by Eq. 4.19, where $\mu_{epi}(E)$ is the total absorption coefficient for the silicon epitaxial layer in the CCD for x-ray energy *E*, d_{epi} is the epitaxial layer thickness.

$$\exp(-\mu_{phos}(E)(d_p - d_0))\left[1 - \exp(-\mu_{epi}(E)d_{epi})\right] \times E/3.65eV$$

Eq. 4.19

- The signal created from a direct hit in the CCD is assumed to be collected under a single pixel. Hopkinson (1987) has shown that the maximum diameter of an electron cloud diffusing in the field free region is equal to approximately twice the depth of the undepleted layer. For the CCDs used the epitaxial layer thickness is ~20μm and the depletion depth being around 6μm this makes the maximum diameter of the electron cloud ~28μm which is equivalent to the pixel width of the 15_11 CCD (27μm).

4.2.4.3 Modelling the effect of fibre-optic coupling on MTF

A different approach is required when deriving the PSF of a phosphor layer deposited onto a fibre optic face plate. For a single fibre there is a finite numerical aperture which defines a maximum angle of incidence θ^{MAX} beyond which there is no light transmitted given by Eq. 4.20 where n_f, n_p, n_c, are equal indices of refraction of fibre core, phosphor, fibre cladding respectively. In the theoretical model contributions to PSF are included only for $\theta<\theta_{MAX}$.

$$\theta^{MAX} = \sin^{-1}\left(\sqrt{n_f^2 - n_c^2}\,/\,n_p\right)$$

Eq. 4.20

4.2.4.4 Modelling the effect of light absorption in the phosphor on MTF.

The GdO_2S_2 based phosphors are opaque and a certain amount of self absorption of scintillation light occurs. The effect of this absorption is modelled by modifying Eq. 4.17 to give Eq. 4.21

$$PSF(X,Y,Z,E) = PSF(X,Y,Z,E)\exp[-\lambda (X^2 + Y^2 + Z^2)^{1/2}]$$

Eq. 4.21

where λ is the reciprocal absorption length for scintillation quanta in the phosphor layer.

A computer program was written to calculate the ensemble average of point spread functions PSF(X,Y) arising from contributions from a thin slice *dZ*, of phosphor over the entire thickness of phosphor for the incident x-ray spectrum. Contributions to the signal from direct hits in the CCD were included and weighted over the incident x-ray spectrum. The LSF(X)was obtained from the PSF(X,Y) using Eq. 4.18 and was Fourier transformed to obtain the spatial frequency dependent function *G(f)*. The MTF(f) was obtained using Eq. 4.22.

$$MTF(f) = \frac{G(f)}{G(0)}$$

Eq. 4.22

where $G(0)$ is the zero spatial frequency value of $G(f)$.

4.2.5 Results and discussion for direct coated detectors

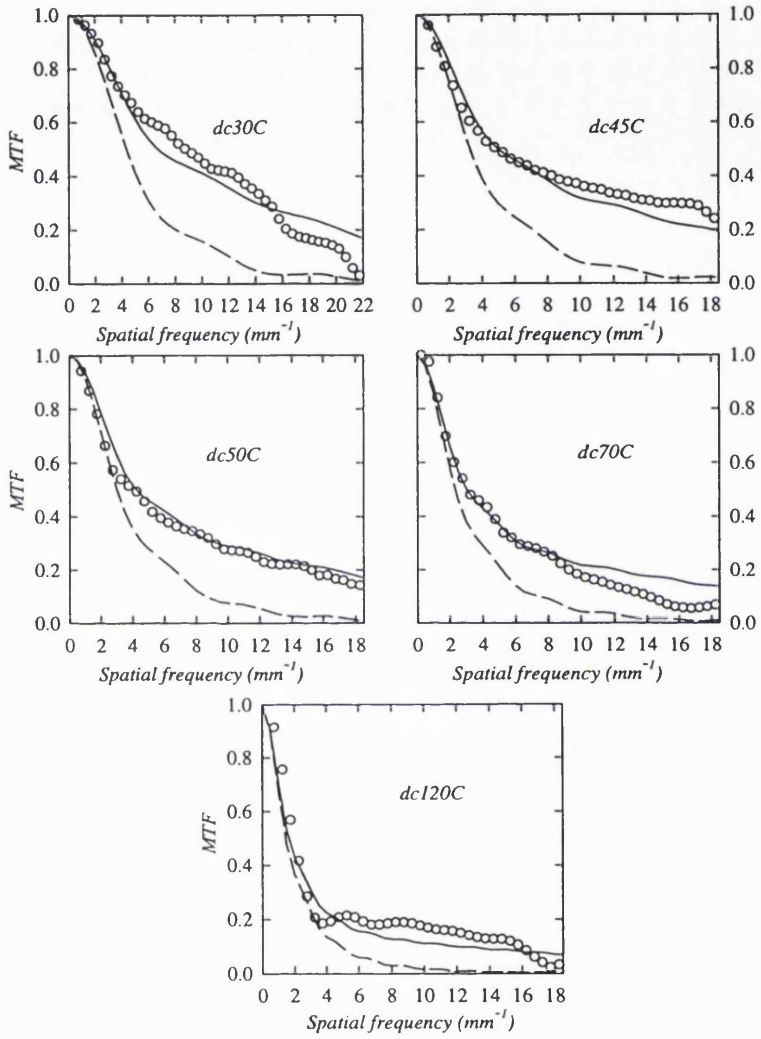

Figure 4.9 MTF for direct coated devices. Circles represent experimentally obtained data points. Solid line is theoretical data. Dashed line is theoretical MTF due to CsI(Tl) only.

Figure 4.9 shows the MTF's of the directly coated detectors dc30C, dc45C, dc50C, dc70C and dc120C.Theoretical values were calculated with $g=52\ keV^{-1}$, $d_o=20\mu m$, $d_{epi}=20\mu m$, and a 28kVp Mo/Mo spectrum. Errors on experimental values of MTF were estimated to be around 5% at 2lp/mm and 10% at 10lp/mm and 15% at 15lp/mm and

higher. It can be observed that generally there is good agreement between experimental and theoretical MTF's.

Comparing the overall detector MTF with the MTF of the phosphor layer only one can see that direct hits in the CCD has the effect of increasing the MTF at higher frequencies for all the detectors. In general the increase in MTF due to direct hits is greater for detectors with thinnest phosphor layers. This is as expected because with smaller phosphor layers the contribution to signal from direct hits increases.

4.2.6 Results and discussion for fibre optically coupled detectors

4.2.6.1 Detectors fo50C, fo70C and fo130f.

Figure 4.10 shows MTF's for detectors fo50C, fo70C and fo130C. The theoretical MTF for the phosphor/optical fibre combination was calculated with $g=52\ keV^{-1}$, $d_o=20\mu m$, $n_f=1.81$, $n_c=1.48$, $n_p=1.5$, a 28kVp Mo/Mo spectrum and appropriate transmission efficiencies to give the same number of electrons per x-ray as experimentally observed. The detector MTF was calculated using Eq. 4.23 where $MTF_{phos/fib}$ is the MTF of the phosphor/fibre combination, MTF_{ccd} is the CCD MTF and p_{fib} is the fibre pitch in the fibre optic faceplate. Errors on experimental values of MTF were estimated to be around 5% at 2lp/mm and 10% at 10lp/mm and 15% at 15lp/mm and higher.

At low spatial frequencies there is poor agreement between theoretical predicted and

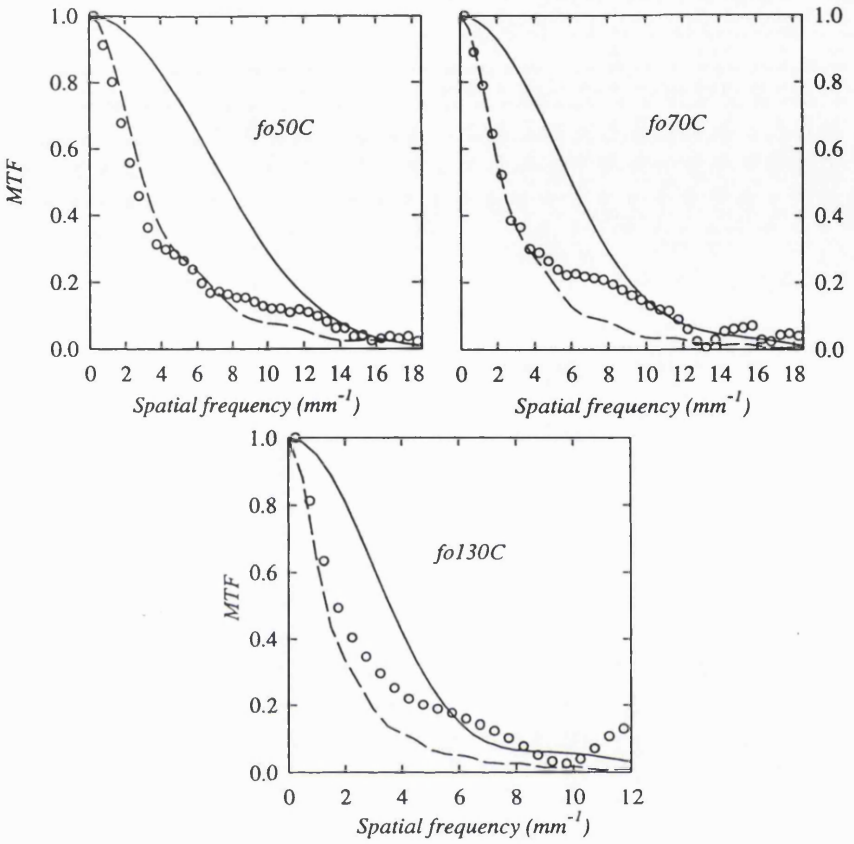

Figure 4.10 MTF's for detector fo50C, fo70C and fo130C. Circles represent experimentally obtained data. Solid line is theoretical MTF, dashed line is the theoretical MTF due to the phosphor layer.

experimental MTFs. The MTF resembles the MTF due to the phosphor layer only. This shows that the finite numerical aperture associated with the fibre optic coupling has little effect upon the MTF of the detector at these spatial frequencies. In the frequency range 6-12 lp/mm the experimental MTF has increased values when compared to the MTF due only to the phosphor layer. Moreover these increased values tend towards the theoretical MTF which includes effects due the finite numerical aperture.

$$MTF_{det} = MTF_{phos//fib} \times MTF_{ccd} \times SINC(\pi\, f\, p_{fib}) \qquad \textbf{Eq. 4.23}$$

Detectors fo70C and fo130C have phosphor layers on a secondary fibre optic stud which is coupled to a fibre optic faceplate. Improvements in MTF for these detectors are

expected if the phosphor layer/fibre optic is coupled directly on the CCD, this would also increase the optical coupling efficiency by a factor of 1.2.

4.2.6.2 Detector fohama

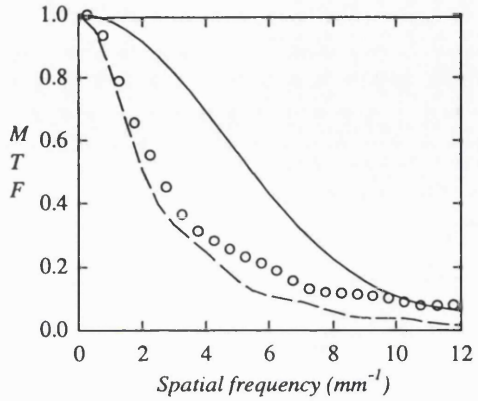

Figure 4.11 MTF's for detector fohama. Circles represent experimentally obtained data. Solid line is theoretical MTF, dashed line is the theoretical MTF for 80μm of CsI(Tl).

Figure 4.11 shows MTF's for detector fohama. The theoretical MTF for the phosphor /fibre combination was calculated with $g=52\ keV^{-1}$, $d_o=20\mu m$, $n_f=1.81$, $n_c=1.48$, $n_p=1.5$, a 28kVp Mo/Mo spectrum and appropriate transmission efficiency to give the same number of electrons per x-ray as experimentally observed. The detector MTF was calculated using Eq. 4.23 as in the previous section. Again (similar to the results obtained for other fibre optic coupled detectors) it can be seen that at lower frequencies there is poor agreement between experimental and theoretically predicted MTF and the MTF closely resembles the MTF of the phosphor layer only. In the frequency range 5-12lp/mm there is an increase in values and they tend towards the MTF including numerical aperture effects.

Nishikawa (1989) has described the effects of using a reflective backing with a phosphor coating and can be summarised as follows.

- The MTF of a transparent phosphor later with reflective backing drops of more rapidly compared to a phosphor layer without reflective backing. The

MTF corresponding to a phosphor layer with a reflective backing can be approximated by modelling the phosphor layer as if it was twice as thick.

- The light yield is increased to as much as a factor of 2.

Results for detector fohama show there is good agreement between the experimental MTF and the phosphor layer MTF. Comparing the x-ray sensitivity of detector fohama with that of the similarly configured detector fo70C (and correcting for differences in thicknesses, ~ 6%), one finds the sensitivity of detector fohama is a factor of ~1.5 greater than detector fo70C. These results show that the intagliated fibre optic faceplate used in conjunction with a reflective layer in the detector fohama increased the light yield from the phosphor layer without compromising the detector MTF.
It is noted that optical coupling efficiency for this device could be improved by a factor of ~1.2 by coupling the phosphor/intagliated fibre optic face plate directly to the CCD

4.2.6.3 Detectors ft70C and ft130C

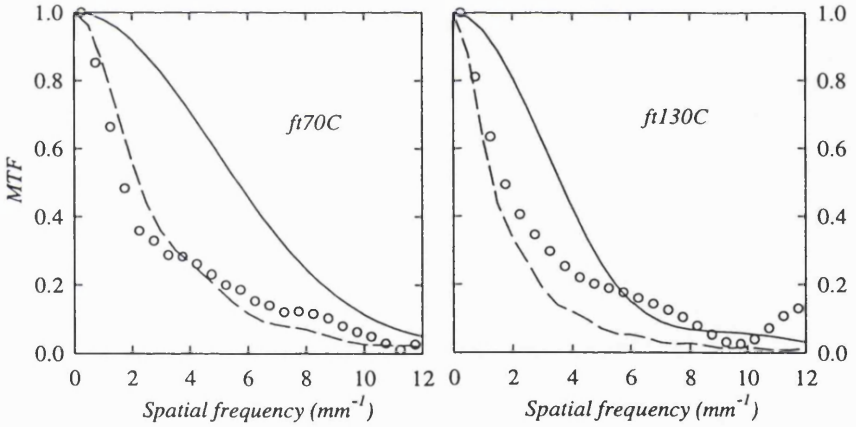

Figure 4.12 MTF's for detector ft70C and detector ft130C. Circles represent experimentally obtained data. Solid line is theoretical MTF, dashed line is the theoretical MTF of the phosphor screen/fibre optic combination..

Figure 4.12 shows MTFs for detectors ft70C and ft130C. The theoretical MTF for the phosphor/fibre optic combination was calculated *with* $g=52\ keV^{-1}$, $d_o=20\mu m$, $n_f=1.81$, $n_c=1.48$, $n_p=1.5$, a 28kVp Mo/Mo spectrum and appropriate transmission efficiencies to give the same number of electrons per x-ray as experimentally observed.

The overall detector MTF was calculated using Eq. 4.23 with p_{fib} = 0.010mm. Again at low spatial frequencies there is poor agreement between theoretically predicted and experimental MTFs and the MTF resembles the MTF due to the phosphor layer. But at spatial frequencies in the range 5-10lp/mm there is an increase in the values tending to those modelled with the effect of fibre optic numerical aperture (this is most apparent for the detector ft130C.

4.2.6.4 Detectors fo50G, fo200G

Figure 4.13 show MTF's for detectors fo50G and fo200G. The theoretical MTF of the phosphor/fibre combination was calculated including effects due to attenuation of the light. Parameters used *were* $g=62keV^{-1}$, $d_0=20\mu m$, $\lambda=0.05mm^{-1}$, a 28kVp Mo/Mo spectrum and appropriate transmission efficiencies to give the same number of electrons per x-ray as experimentally observed. For comparison the MTF was calculated without any attenuation of optical light. The detector MTF was calculated using Eq. 4.23 with $p_{fib}=6\mu m$.

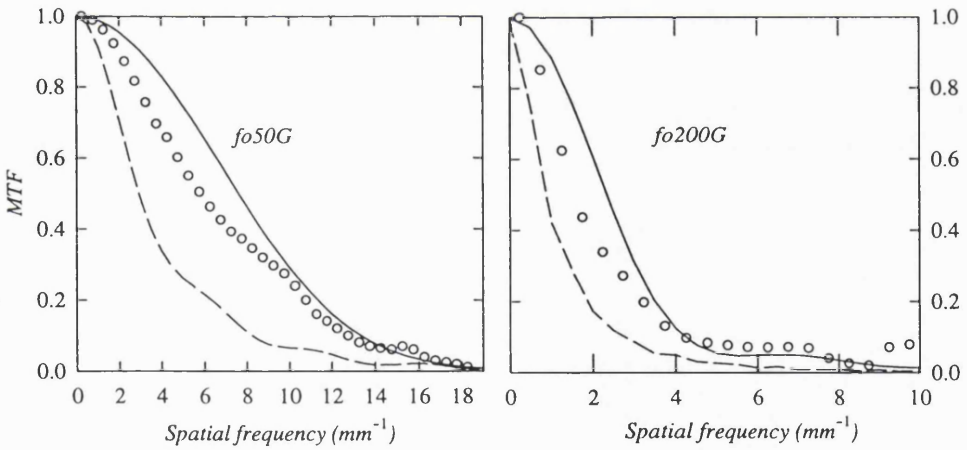

Figure 4.13 MTF's for detector fo50G and fo200G. Circles represent experimentally obtained data. Solid line is theoretical MTF, dashed line is the theoretical MTF without any optical attenuation.

Results for detector fo50G and fo200G show moderate agreement between experimental and theoretically predicted detector MTF's. It can be seen that optical attenuation in the phosphor has the effect of increasing the MTF at all spatial frequencies. Differences between theoretical MTFs can be attributed to the fact that the phosphor also acts as a

scattering medium scattering optical photons, this would have the effect of decreasing MTF values.

4.2.6.5 Detector foMinR

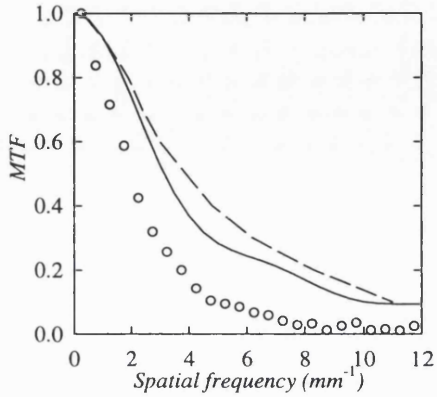

Figure 4.14 MTF's for detector foMinR. Circles represent experimentally obtained data. Solid line is theoretical MTF, dashed line is the theoretical MTF due to the phosphor screen only.

The MTF of detector foMinR is shown in Figure 4.14. The theoretical MTF was obtained with $g=62keV^{-1}$, $d_0=20\mu m$, $d_1=85\mu m$ (Nishikawa 1989), $n_f=1.81$, $n_c=1.48$, $n_p=1.5, \lambda=0.05mm^{-1}$, a 28 kVp Mo/Mo spectrum and appropriate transmission efficiencies to give the same number of electrons per x-ray as experimentally observed. For comparison the theoretical phosphor screen MTF is included (taken from A. Maidment, 1993).

It can be seen that there is poor agreement between experimental and theoretical MTF. The light yield from the screen obtained experimentally is 50% of what is expected. The difference in light yield is attributed to losses/scattering at the screen/ fibre optic interface. The poor agreement between theoretically predicted and experimental MTF's are attributed to blurring effects that occur at this interface. These effects could be reduced by using coupling fluid between the screen and the fibre optic faceplate, ensuring that the fluid does not corrode the screen surface.

4.2.7 Summary of MTF analysis

Two methods of measuring the modulation transfer function of digital radiographic devices have been demonstrated. Both methods have been shown to produce similar results.

A model for calculating theoretical MTF's was constructed. This model included the effects of direct hits in the CCD and the numerical aperture of the fibre optic coupling and attenuation of scintillation photons.

Results for directly coated devices show that direct hits in the CCD have the effect of increasing MTF values at higher spatial frequencies and that this effect is greater for thinner phosphor layers.

Results for fibre optically coupled detectors show that the effects of finite numerical aperture do affect the MTF at high spatial frequencies. There is an increase in values at higher spatial frequency values (compared to the MTF for the phosphor layer only) for all the fibre optically coupled detectors considered.

The intagliated fibre optic faceplate and reflective covering used in detector fohama increases the light yield from the phosphor layer without increasing blurring. This result is reflected in the fact that the MTF of fohama is very similar to that expected for 80μm thickness of CsI(Tl) without any intagliation.

For all CsI(Tl) phosphor based detectors it is concluded that there is no discernible effect from the columnar structure of the phosphor . This conclusion is arrived at by virtue of the fact that the theoretical MTF's were modelled considering the scintillation photons were emitted isotropically and followed un-scattered paths to the output surface of the phosphor, which would not be the case for a phosphor with a columnar structure. This result is similar to one found by Martinez (Ph.D thesis 1994), were the effects due to columnar structure were modelled.

The GdO_2S_2 based phosphor produced better MTF's compared with a none optical attenuating phosphor.

Results for the Min-R coupled detector foMinR were disappointing and were not as good as achieved in other groups (Maidment 1994). This is attributed to the poor optical coupling efficiency in the detector and reduction in quantum detection efficiency A_Q by the use of carbon fibre cassette to hold the screen in contact.

4.3 Limiting spatial resolution

The limiting resolution of the CCD system was determined from images of a type 9 star pattern phantom. All images were taken under the same exposure conditions as used in the MTF measurements.

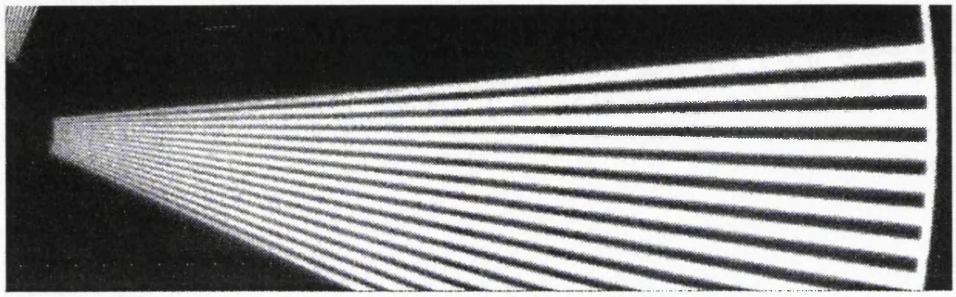

Figure 4.15 Image of star pattern obtained with detector dc120C.

An average of 5 images of the star pattern was obtained. The limiting spatial resolution was calculated by measuring the radial distance from the innermost diameter D, of the bar pattern to the point were all of the 14.5 line pairs could be seen.. The limiting spatial frequency is given by f=1.27×90/D. .Figure 4.15 shows an image of star pattern obtained with detector dc120C.

No variation of limiting spatial resolution was found by changing the orientation of the star pattern. The limiting spatial resolution was estimated from the MTF for each detector by finding the spatial frequency at which the MTF value is 0.05.
Figures for limiting spatial resolution are tabulated in Table 4.1 together with values of spatial frequency at which the MTF is reduced to 0.05 and the Nyquist frequency for each detector.

4.3.1 Directly coated detectors

The highest spatial resolution available on the star pattern was insufficient to measure the limiting spatial resolution of all the directly coated detectors as all spatial frequencies could be seen. The limiting spatial resolution for all directly coated detectors was greater than 17.9 lp/mm.

*The spatial frequency at which the MTF is 5% of its maximum value is accepted as a measure of limiting spatial frequency

It can be observed in that there is generally good agreement between the value of limiting spatial resolution obtained from the star pattern and the MTF value. The value of limiting resolution is very close to the Nyquist frequency which is the theoretical resolution limit.

Table 4.1 limiting resolution, Nyquist frequency and 5% MTF spatial frequency value for CCD based detectors. Errors on limiting resolution obtained from MTF are ~8%.

Detector	*Limiting spatial frequency (MTF) (1/mm).*	*Nyquist frequency (1/mm)*	*Liming spatial frequency (1/mm).*
dc30C	20.5	22.7	>17.9
dc45C	18.5	18.5	>17.9
dc50C	21.0	22.7	>17.9
dc70C	18.5	18.5	>17.9
dc120C	18.5	18.5	>17.9
fo50C	14.5	18.5	15.0±0.5
fo70C	12.0	18.5	12.5±0.5
fo130C	9.0	18.5	9.3±0.5
fo50G	22.5	22.7	>17.9±0.5
fo200G	7.4	18.5	7.0±0.5
fohama	18.0	18.5	>17.9
foMinR	7.0	18.5	9.2±0.5
ft70C	10.2	13.15	9.0±.5
ft130C	7.5	13.15	8.0±0.5

4.3.2 Fibre optic coupled detectors

It can be observed in Table 4.1 that there is generally good agreement between the value of limiting spatial resolution obtained from the star pattern and the MTF value of 0.05. The value of limiting resolution is generally lower than the Nyquist frequency which shows that the spatial resolution is determined by spatial transfer properties of the phosphor layer and fibre optic coupling.

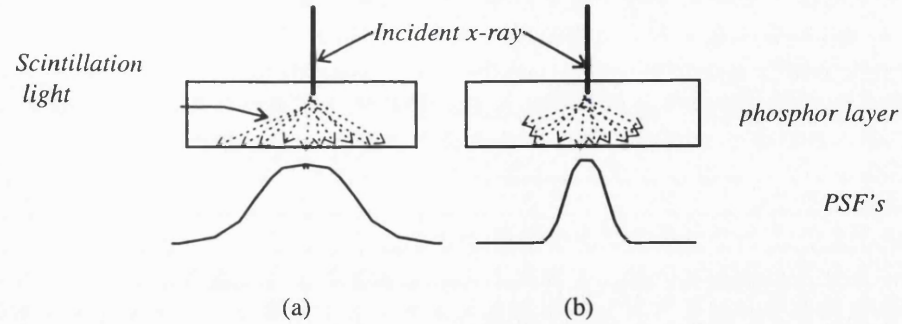

Figure 4.16 scintillation light distribution and associated average PSF for (a) transparent phosphor, (b) light attenuating phosphor.

Comparison's between detectors fo50C and fo50G show that the GdO_2S_2 based detector has a higher limiting spatial resolution (~ >17.9 lp/mm). This is attributed to the light attenuation properties of the opaque phosphor layer which means that there is less light reaching the exit surface of the phosphor as shown in Figure 4.16 which reduces blurring effects.

4.3.3 Discussion of limiting spatial resolution results

A method for determining the limiting spatial resolution of an radiological imaging devices has been described. Results obtained agree well with corresponding values obtained from MTF curves (MTF value of 0.05). Results show that the directly coated detectors have the highest limiting spatial resolution. This is due to the contribution to the signal from direct hits in the CCD which have been modelled in a previous section. At the exposure level at which the measurements were made there must have been enough direct hits in the CCD to achieve some spatial correlation between direct hits.

Results for the fibre optically coupled detectors show that in general higher limiting spatial resolutions are obtained for the thinner phosphor layers as expected.

*where M= number of pixels in the slit and dy is the height of a pixel

4.4 Noise Spectral Analysis

Noise is one of the primary factors contributing to the degradation of digital radiographic images. Pixel rms. noise indicates only the magnitude of the noise and not its texture. In this section the application of Wiener spectral analysis (also known as noise power spectrum NPS) to characterise the magnitude and texture of noise is described.

4.4.1 Wiener spectrum analysis for digital systems

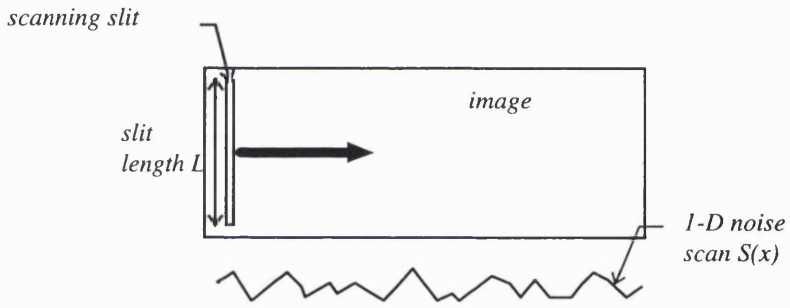

Figure 4.17 use of scanning slit to obtain 1-D noise scan.

The measurement of Wiener spectrum for digital radiographic devices has been performed by a number of investigators (Maidment 1994, Goldman 1992, Giger 1984, Fu 1984) The most common method used was the scanning slit technique. In this method the analysis of a 2-D noise sample is reduced to a 1-D case by scanning the data using a long narrow slit. For discrete images 1-D noise scans may be synthesised by averaging pixels along the slit length shown in Figure 4.17. For a slit scanning in the horizontal direction, the measured spectrum $\hat{W}(f)$ is related to the true spectrum $W(u,v)$ as shown in Eq. 4.24 where $T(u,v)$ is the transfer function of the measuring slit. For a finite slit of width dx and length $L = Mdy$, $T(u,v) = Sinc(dx\,u) \times Sinc(L\,v)$ which gives Eq. 4.25

$$\hat{W}(u) = \int W(u,v)\left|T(u,v)\right|^2 dv$$

Eq. 4.24

Therefore a 1-D central section of the 2-D spectrum can be estimated from the measured spectrum by multiplying $\hat{W}(u)$ by the appropriate correction factors.

$$\hat{W}(u) = \frac{1}{L}\sin c^2(dx\ u)W(u,0)$$

Eq. 4.25

If P(x,y) represents a 2-D noise sample, a series of 1-D noise scans of length *Ndx*, can be obtained by averaging the pixel data in a direction perpendicular to the scan. For a vertical slit length *L=Mdy*, the 1-D noise scan is given by *S(x)* in Eq. 4.26

$$S(x) = \frac{1}{L}\sum_{y=0}^{L-1} P(x,y)$$

Eq. 4.26

The Wiener spectrum estimate is obtained as the discrete Fourier transform of *S(x)* and is given in Eq. 4.27 were <..> denotes an ensemble average over many noise profiles.

$$W(u,0) = \frac{L}{N\,dx\,\mathrm{sinc}^2(dx\ u)}\left\langle \left| \sum_{x=0}^{N-1} S(x)e^{-2\pi u/N}dx \right|^2 \right\rangle$$

Eq. 4.27

4.4.2 Methods and materials for calculating NPS

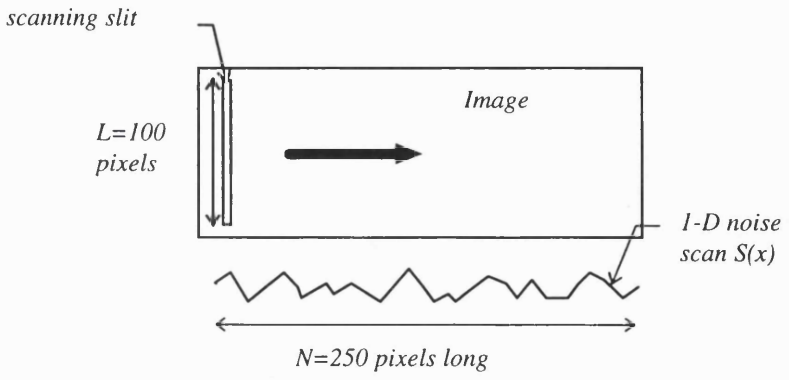

Figure 4.18 Diagram to show configuration for measuring noise profiles

The image data was obtained with the detector area uniformly irradiated. The exposure conditions used were (the same as the ones used in the MTF measurement) .28kVp, Mo-Mo spectrum and mAs value such that a pixel in the CCD is 'half filled'; tube to detector distance was 120cm. All images were corrected for pixel offset and gain. Data were summed in one direction to synthesise the effect of a scanning slit. A slit with a width of 1 pixel and a length of 100 pixels was used. It was found that using slits longer than 100 pixels did not alter the shape of the calculated NPS which indicates that a good estimate of the central section of the 2-D NPS had been obtained. The slit was scanned across the image to produce a 1-D data sample containing noise fluctuations. Each data sample was 250 pixels long which enabled calculation of spectral estimates for spatial frequencies between 0.148 and 18.5 mm^{-1}. For each NPS measurement 20 data samples were obtained and stored to file.

In order to reduce random error in the spectral estimates it is necessary to obtain a large number of noise profiles. This was achieved by using a purposely written computer program which calculated noise profiles from the data samples. Using the computer program 190 noise profiles were obtained from the 20 data samples written to file. The noise profiles were calculated using Eq. 4.28, where $\Delta S(x)$ is the noise profile and $S_n(x)$ is the n^{th} data sample and $S_i(x)$ is the i^{th} data sample. The steps used in the computer program are summarised below.

$$\left[\left[\Delta S(x) = S_n(x) - S_i(x)\right]_{n=2}^{20}\right]_{i=1}^{19}$$

Eq. 4.28

1. Read data sample 1 and data sample 2 from file.
2. Obtain 1^{st} noise profile by subtracting data samples. The subtraction process increases the magnitude of the noise(variance) by a factor of 2. This is corrected for by dividing by 2.0.
3. Read data sample 3 from file. The noise profile is written to file.
4. Subtract data sample 3 from data sample 1 and correct to obtain 2^{nd} noise profile. Write to file.
5. Repeat up to data sample 20. This gives 19 independent noise profiles.

6. Read in data sample 2 and data sample 3. Calculate noise profile. These procedures continue until the 20^{th} data sample is subtracted from the 19^{th}. The total number of noise profiles is given by $\sum_{i=1}^{i=19} n - i = 190$ where n is the number of data samples (n=20).
7. Calculate and sum the discrete Fourier transform of each individual noise profile.
8. Calculate NPS using Eq. 4.27.

The uncertainty in the spectral estimates is of the order of the square root of the number of noise profiles used which gives ~7% for 190 noise profiles. This was reduced further by averaging and resampling each spectrum to give spectral values between $0.25mm^{-1}$ and $18.5mm^{-1}$ in $0.5mm^{-1}$ increments. The presented spectral estimates have a standard error of 3.8%.

4.4.3 Contributions to total noise power spectrum

The total noise power spectrum, $W_T(f)$, can be expressed as the sum of three constituent noise sources (Nishikawa 1990, Maidment 1994) given in Eq. 4.29.

$$W_T(f) = W_Q(f) + W_{SQ}(f) + W_D(f)$$

Eq. 4.29

All NPS are expressed in terms of electrons generated in the CCD image array. $W_Q(f)$ includes factors to describe the spatial frequency distribution of fluctuations in the number of x-rays interacting the screen and the variation in the number of light quanta emitted from the screen per x-ray interaction. $W_{SQ}(f)$ describes the statistical fluctuation in the number of secondary quanta that would occur in the absence of x-ray quantum noise. These secondary quanta are produced independently, and are uncorrelated therefore $W_{SQ}(f)$ is independent of spatial frequency. $W_D(f)$ describes the signal fluctuations inherent to the imaging system, which includes dark current and electronic noise.

4.4.3.1 Measurement of $W_D(f)$ and $W_{SQ}(f)$

The dark noise power spectrum, $W_D(f)$, was measured by taking images with the detector shielded from any irradiation or illumination and using the same method as detailed in section 4.4.2. This was repeated for all detectors.

The secondary quantum noise power spectrum, $W_{SQ}(f)$, was measured by taking images with the detector placed in a uniform light field. The experimental set-up was the same as used for the calibration of the no. of electrons per ADU. Images were corrected for pixel gain and offset and the method detailed in section 4.4.2 was used. $W_{SQ}(f)$ was calculated by subtracting $W_D(f)$ from the measured noise power spectrum. This was repeated for various illumination levels and all detectors. The quantum noise power spectrum, $W_Q(f)$, is calculated using Eq. 4.30.

$$W_Q(f) = W_T(f) - W_{SQ}(f) - W_D(f) \qquad \textbf{Eq. 4.30}$$

4.4.3.2 Results for $W_D(f)$ and $W_{SQ}(f)$

Figure 4.19 shows $W_D(f)$ for detector dc120C at 298K for a dark signal of ~15k electrons per pixel. Errors on the each spectral estimate are 3.8%.

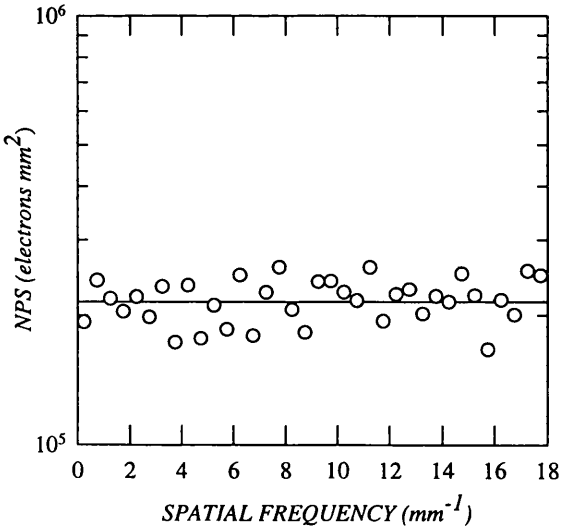

Figure 4.19 $W_D(f)$ for detector dc120C(measured at signal level of 1.5k electrons).

If the only contribution to $W_D(f)$ is from dark signal generation then the spectrum should be frequency independent as fluctuations in dark signal are uncorrelated.
$W_{SQ}(f)$ is shown in Figure 4.20 measured at 298K for a signal of 300k electrons per pixel. Errors on spectral estimates are 7.6%. It can been seen that $W_{SQ}(f)$ is essentially frequency independent. This is expected because fluctuations in secondary quanta are uncorrelated

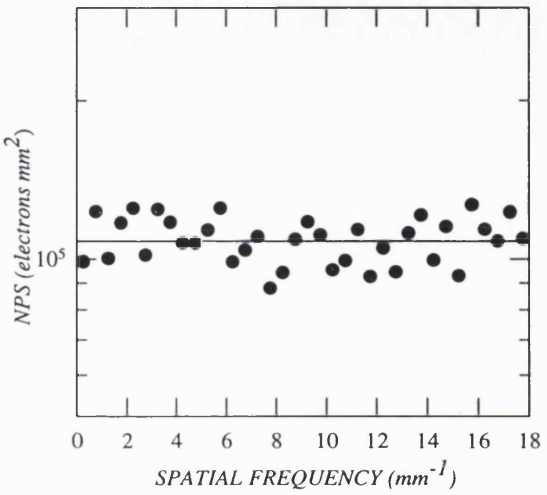

Figure 4.20 $W_{SQ}(f)$ measured for detector dc120C (measured at mean signal level of 300k electrons) solid line is the mean of $W_{SQ}(f)$ over frequencies plotted.

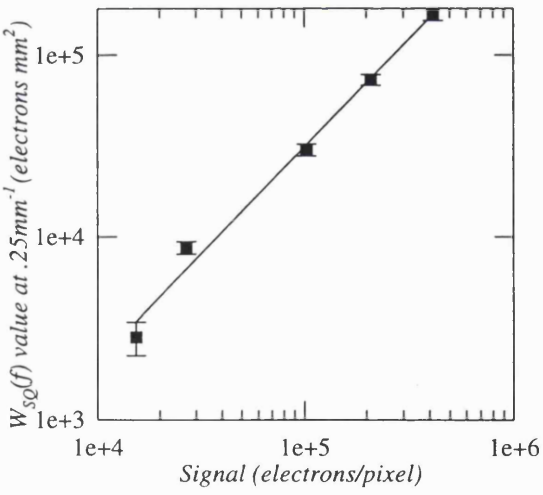

Figure 4.21 Mean value of $W_{SQ}(f)$ as a function of signal level from 'flat field' illumination.

Figure 4.21 shows mean $W_{SQ}(f)$ value as a function of mean signal level in the detector. It can be seen that there is a linear relationship between the mean $W_{SQ}(f)$ value and the mean signal level, this is as expected because the square of the image noise directly proportional to the signal level.

4.4.4 Results for fibre optically coupled detectors

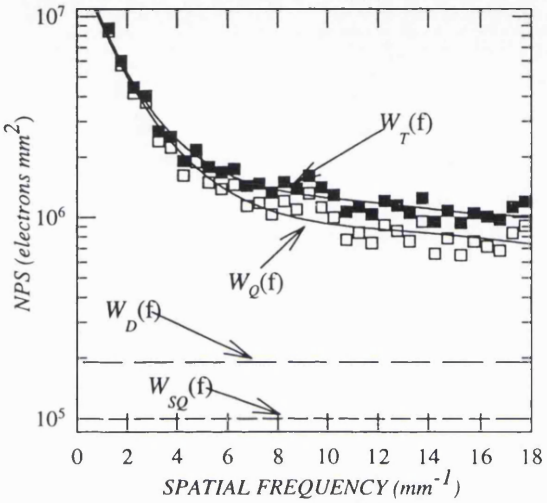

Figure 4.22 Total Noise power spectrum and components for detector fo70C. Solid lines are regressions to the data.

Figure 4.22 shows plots of the total noise power spectrum and its components for detector fo70C. $W_{SQ}(f)$ and $W_D(f)$ are averaged over the frequencies of interest (0-18mm^{-1}). Results show that the quantum noise power spectrum $W_Q(f)$ is the major component for all spatial frequencies. This means that the images from the detector are x-ray quantum noise limited for all spatial frequencies for the absorbed dose in air used, which was 0.7mGy.

The x-ray quantum noise transfer function $NTF_Q(f)$ is the noise analogue of the MTF and describes the spatial frequency dependence of $W_Q(f)$, the x-ray quantum NPS. It is defined in Eq. 4.31.

$$NTF_Q^2(f) = \frac{W_Q(f)}{W_Q(0)}$$

Eq. 4.31

Figure 4.23 shows plots of $NTF_Q(f)$ for detectors fo70C and fo130C. Also included are plots of $MTF^2(f)$ for each detector. At low spatial frequencies, it can be seen that $NTF_Q(f)$ is very similar in shape to $MTF^2(f)$ for both detectors, this is as expected because x-ray quantum noise will have the same spatial frequency distribution as the signal. At higher spatial frequencies, $NTF_Q(f)$ is larger than $MTF^2(f)$ which shows that noise is passed more efficiently than signal. This means signal to noise ratio will be passed less efficiently by the detector at theses spatial frequencies. Similar results were obtained for all fibre optically coupled devices.

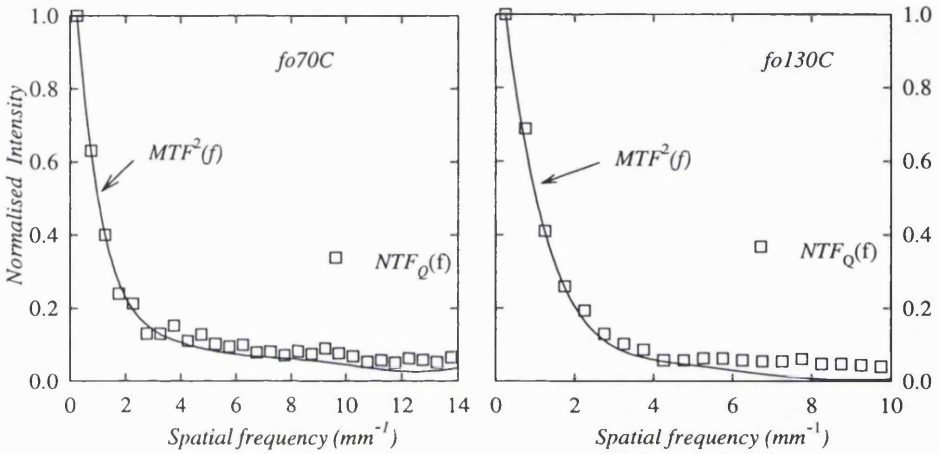

Figure 4.23 plots of $NTF_Q^2(f)$ and $MTF^2(f)$ for detector fo70C and fo130C

4.4.5 Results for direct coated detectors

The total noise power spectrum and its components are shown in Figure 4.24 for detectors dc45C. As can be seen the detectors are x-ray quantum noise limited for all spatial frequencies shown.

The shape of the $NTF_Q(f)$ was modelled for these devices using Eq. 4.32 where $|..|$ denotes re-normalisation, $MTF_{phos}(f)$ is the phosphor MTF and $MTF_{direct}(f)$ is the MTF associated with direct hits in the CCD and σ_X is the rms quantum noise, σ_{epi} is the rms noise due to direct hits The method of calculating σ_X and σ_{epi} is given in chapter 3. This model assumes that all the signal created from a direct hit is collected under a single pixel so the $MTF_{direct}(f)$ is determined by the square sampling aperture of the pixel and is given in Eq. 4.33 where p is the pixel size.

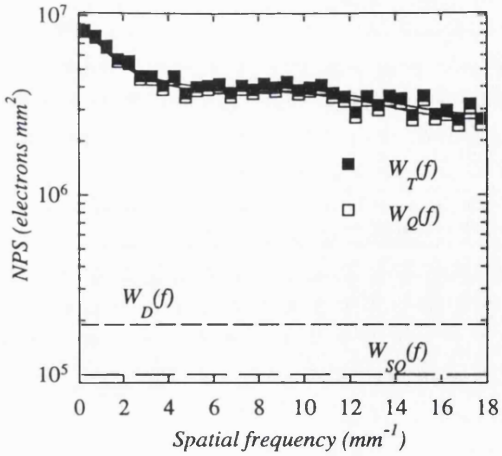

Figure 4.24 Total Noise power spectrum and components for detector dc45C. Solid lines are regressions to the data.

$$Theoretical\ NTF_Q(f) = \left|\sigma_X^2 \times MTF_{phos}^2(f) + \sigma_{epi}^2 \times MTF_{direct}(f)\right|$$

Eq. 4.32

Figure 4.25 shows good agreement between theoretical $NPS_Q(f)$ and those obtained experimentally for all the directly coated CCDs.

$$MTF_{direct}(f) = Sinc(\pi fp)$$

Eq. 4.33

By comparing $NTF_Q(f)$ and $MTF^2(f)$ for these devices (Figure 4.25) it can be seen that the x-ray quantum noise which arises from interactions in the phosphor only dominate up to around 2mm^{-1} the 'extra' noise power arises from fluctuations in the number of direct hits in the CCD.

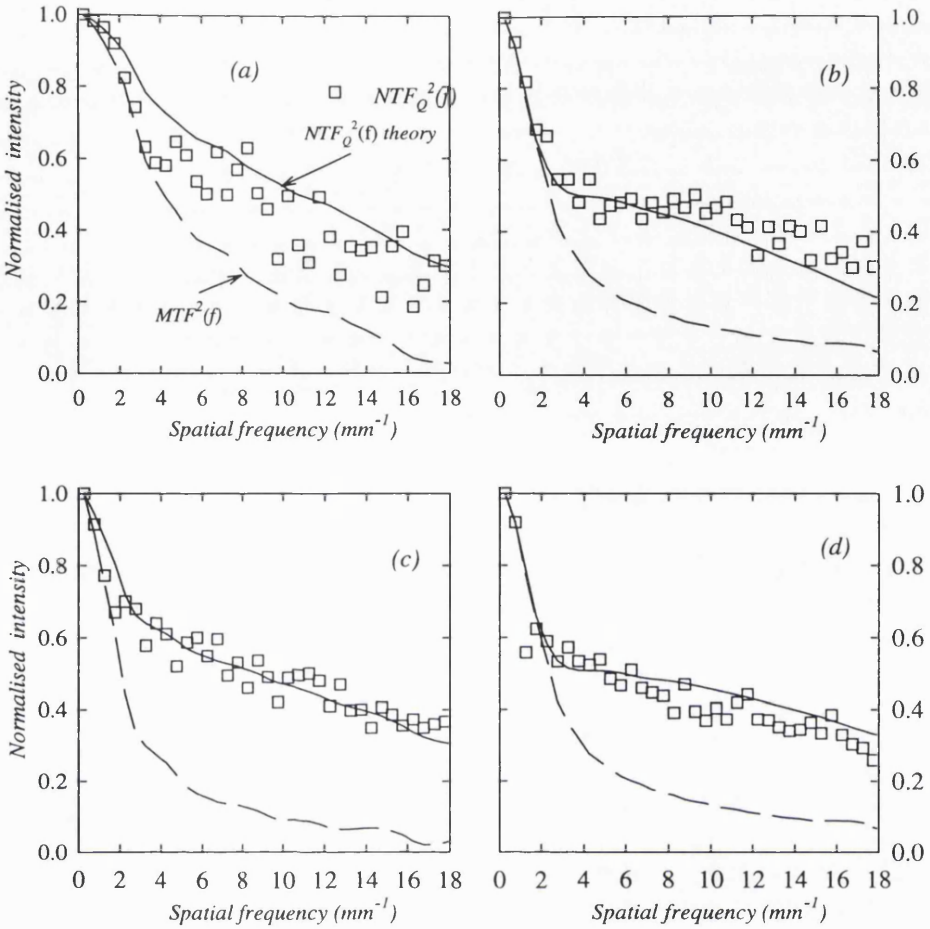

Figure 4.25 plots of $NTF_Q^2(f)$, $MTF^2(f)$ and theoretical $NTF_Q^2(f)$ for detectors (a) dc30C, (b) dc45C, (c) dc50C and (d) dc120C.

4.4.6 Effect of dose upon NPS

The total NPS was measured for two absobed dose in air levels of 11mGy and 0.78mGy, results are shown in Figure 4.26. It can be seen that the magnitude of the total NPS at zero spatial frequency is larger for the NPS measured for the higher dose as expected as the absolute value of x-ray quantum noise increases. This was found with all detectors. The image produced from the detector is said to be X-ray quantum noise limited up to a certain frequency if the magnitude of the X-ray quantum noise is greater than the magnitude of other noise sources. The magnitude of the total NPS is such that for a dose of .785mGy the image produced from the detector is quantum noise limited only up to 10lp/mm. For the higher dose, the image is quantum noise limited up to around 16/lp/mm.

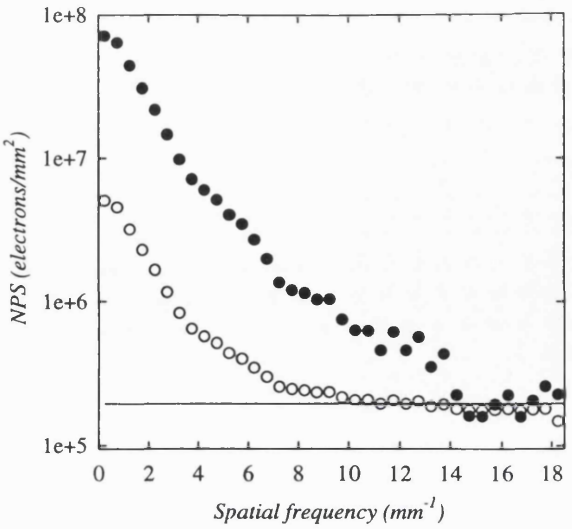

Figure 4.26 Total NPS measured for detector fohama for 11mGy (black circles) and 0.785 mGy (white circles). Solid line is $W_D(f)$ for the detector.

4.4.7 Discussion of results of NPS analysis.

A method for measuring Wiener spectrum has been described and used to measure the noise power spectrum and its components for the detectors under evaluation.

The dark signal NPS is shown to be essentially flat which shows that dark signal noise is uncorrelated. The secondary quantum NPS $W_{SQ}(f)$, is shown to be essentially flat and spatial frequency independent and the mean value of $W_{SQ}(f)$ increases linearly with signal as expected.

The dose for which the total NPS results were obtained was found to limit the spatial frequency to which the images produced were x-ray quantum noise limited.

For fibre optic coupled detectors the images produced are found to be x-ray quantum noise dominated at all spatial frequencies up to the Nyquist limit (for the exposures used). The shape of the Xray quantum noise transfer function $NTF_Q^2(f)$ is very similar to the $MTF^2(f)$ which shows that signal and noise propagate through the detector in a similar fashion.

The images produced from direct coated detectors are found to be x-ray quantum noise dominated at all spatial frequencies up to the Nyquist limit (for the exposures used). However when $NTF_Q(f)$ and $MTF^2(f)$ are compared it can be seen that there is good agreement up to around $2mm^{-1}$ but for spatial frequencies greater than $2mm^{-1}$ the $NTF_Q(f)$ is greater than $MTF^2(f)$. A simple theoretical model for $NTF_Q(f)$ based on the $MTF^2(f)$ was found to agree well with experimental results. The differences between $NTF_Q(f)$ and $MTF^2(f)$ are attributed to noise associated with direct hits in the CCD. For spatial frequencies greater than $2mm^{-1}$ direct hits in the CCD contribute more to noise than to signal. This result means that the use of direct coated detectors for high resolution imaging may be unfeasible.

The effects of direct hits on DQE(f) and imaging performance are described further in the next section and chapter 5

4.5 Detective Quantum Efficiency

In this section the spatial frequency dependent detective quantum efficiency DQE(f) model of Nishikawa (1990) is used to describe the imaging performance of the detectors under evaluation.

The model has been used extensively for describing imaging performance of radiographic systems, R. Nishikawa et al (1989,1990,1992), A. Maidment et al (1994), Yaffe et al (1990).

4.5.1 Definition

Signal to noise ratio in images is directly related to image quality. Detective quantum efficiency describes the way signal to noise ratio is passed through an imaging system and is defined as

$$DQE(f) = \frac{SNR_{out}(f)}{SNR_{in}(f)}$$

Eq. 4.34

where SNR_{out} is the signal to noise ratio in the image and $SNR_{in}(f)$ is the input signal to noise ratio.

Nishikawa (1989) has given the following definitions in terms of experimentally measured system parameters,

$$DQE(f) = A_Q A_S R_C(f) R_N(f)$$

Eq. 4.35

$$R_N(f) = \frac{W_Q(f)}{W_T(f)}$$

Eq. 4.36

where A_Q is the quantum detection efficiency, A_S is the scintillation efficiency, $R_N(f)$ is the ratio of quantum noise power spectrum and the total noise power spectrum and describes

$$R_C(f) = \frac{MTF^2(f)}{NTF_Q^2(f)}$$

Eq. 4.37

4.5.1.1 Quantum detection efficiency A_Q

The quantum detection efficiency A_Q, is equal to the fraction of x-rays incident on the phosphor which interact depositing their whole energy locally (at the site of interaction). An ideal detector would have A_Q=1.0 i.e. all incident x-rays would interact.

$$A_Q = \frac{\sum_{E}^{kVp}\left[1-\exp\left(-\mu_{photo}(E)d\right)\times N(E)\right]}{\sum_{E}^{kVp} N(E)}$$

Eq. 4.38

A_Q was calculated assuming that only photoelectric interactions occur, there is no fluorescence and all the x-ray energy is deposited locally(at the site of interaction). These assumptions are valid for the incident x-ray spectrum used (28kVp Mo:Mo) and the phosphors used. An x-ray spectrum weighted value of A_Q was calculated using Eq. 4.38 where $\mu_{photo}(E)$ is the photoelectric absorption coefficient for an x-ray of energy E, d is the phosphor thickness and $N(E)$ is the relative number of x-rays at energy E in the poly-energetic x-ray spectrum.

Figure 4.27 shows A_Q as a function of phosphor thickness for CsI(Tl) and $GdO_2S_2(Tb)$ calculated for a 28kVp Mo:Mo x-ray spectrum. Values of A_Q were calculated for all the detectors using Eq. 4.38 and results are shown in Table 4.2

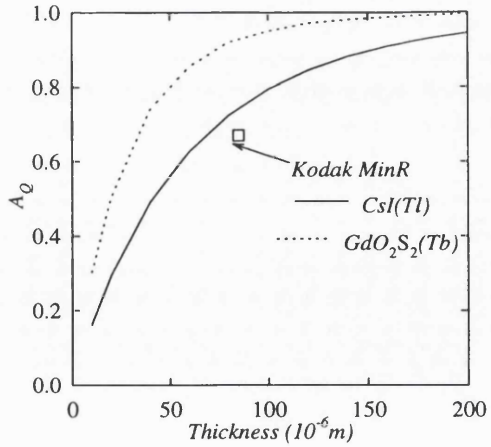

Figure 4.27 quantum detection efficiency A_Q as a function of phosphor thickness for phosphor screens used.

Table 4.2 Values of A_Q

Detector	*Phosphor thickness d (μm)*	A_Q
dc30C	30	.4
dc45C	45	.51
dc50C	50	.57
dc70C	70	.68
dc120C	120	.84
fo50C	50	.57
fo70C	70	.68
fo130C	130	.86
fohama	80	.72
fo50G	50	.80
fo200G	200	.99
foMinR	85	.72
ft70C	70	.68
ft130C	130	.86

4.5.1.2 Scintillation efficiency A_S

The scintillation efficiency A_S, accounts for the degradation in DQE(f) that occurs from the variation in the number of scintillation light quanta emitted from the phosphor per interacting x-ray. It has also been called the Swank factor, Information factor and Statistical factor. An ideal detector would have A_S=1.0.

Consider a beam of monoenergetic x-rays incident upon a phosphor, if all x-rays interacting produced the same number of scintillation quanta then the scintillation

photon spectrum F(n), would look like the one shown in Figure 4.28(a). For a realistic case the scintillation photon spectrum is broad similar to the one shown in Figure 4.28(b). The broadening in the spectrum is due to

(i). Random fluctuations in the number of scintillation quanta being produced per x-ray interaction.

(ii). Differences in the number of scintillation quanta reaching the output surface of the phosphor depending on x-ray interaction depth. This can be quite large in phosphor screens which use light absorbing dyes.

(iii) Using a poly-energetic x-ray source.

Assuming the number of light quanta created from a single absorbed x-ray has a Poisson distribution then A_s is given in Eq. 4.39 where M_j is given in Eq. 4.40 and $M_0 = 1$.

$$A_S = \frac{M_1^2}{M_0 . M_2}$$

Eq. 4.39

$$M_j = \int F(n).n^j dn$$

Eq. 4.40

Swank (1973) has shown that A_S can be split into two components, I_{OPD} due to the optical photon distribution and I_{XED} due to the interacting x-ray energy distribution so that the definition is given in Eq. 4.41.

$$A_S = I_{OPD} . I_{XED}$$

Eq. 4.41

I_{XED} was calculated using Eq. 4.39 for a 28kVp Mo:Mo x-ray spectrum and was found to be equal to 0.98 and was independent of phosphor thickness, this figure is quite high as expected because the incident x-ray spectrum used is virtually monoenergetic.

Since the average number of scintillation quanta produced from a single x-ray interaction is around 900 (for a 17.5 keV x-ray for CsI(Tl)) then I_{OPD} was calculated to be 0.96. Rowlands and Taylor (1983) have obtained values of I_{OPD} =0.95 this lower value could be attributed to a small amount of self absorption in the phosphor. This would produce different numbers of scintillation quanta at the output face depending upon the x-ray interaction depth. For CsI(Tl) phosphor screens A_S was estimated to be 0.93.

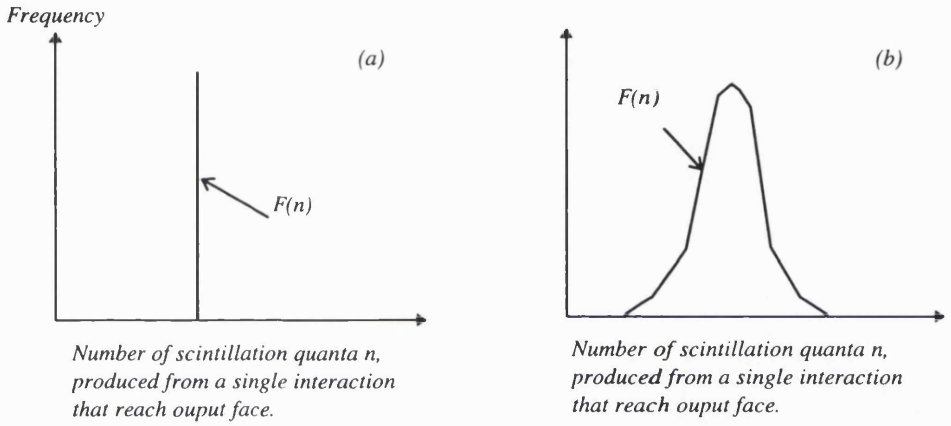

Figure 4.28 spectrum of scintillation quanta for (a) simple case (b) realistic case.

For the GdO_2S_2 based phosphors used values of A_S were estimated to be 0.7 for 50μm thick phosphor and 0.9 for 200μm thick phosphor. These estimations were based on the work of Dick and Motz (1981) who tabulate values of A_S for CsI(Tl) for various thickness'.

For the Kodak Min-R screen, a value of A_S = 0.73 (Dick and Motz (1981)) was used.

4.5.1.3 $R_N(f)$ and $R_C(f)$

For an ideal detector $R_N(f)$ is equal to 1 for all spatial frequencies.

Values of $R_N(f)$ and $R_C(f)$ were calculated using MTFs and NPS's measured in the last sections. Values of $R_N(f)$ close to 1.0 and >0.5 indicate that the detector is x-ray quantum noise limited at spatial frequency f. $R_C(f)$ describes the relative efficiency of

the way signal and noise is propagated through the imaging system and includes spatial frequency dependence of A_S.

4.5.2 Results and discussion for direct coated detectors

Figure 4.29 shows results for $R_N(f)$ and $R_C(f)$ for the directly coated detectors dc30C, dc45C, dc50C and dc120C. The high values of $R_N(f)$ shown in the results for each detector show that all the detectors are quantum noise limited for all frequencies shown. Values of $R_N(f)$ are higher for the 02_06 CCD based detectors (dc30C and dc50C) this is because $W_D(f)$ is lower for these detectors

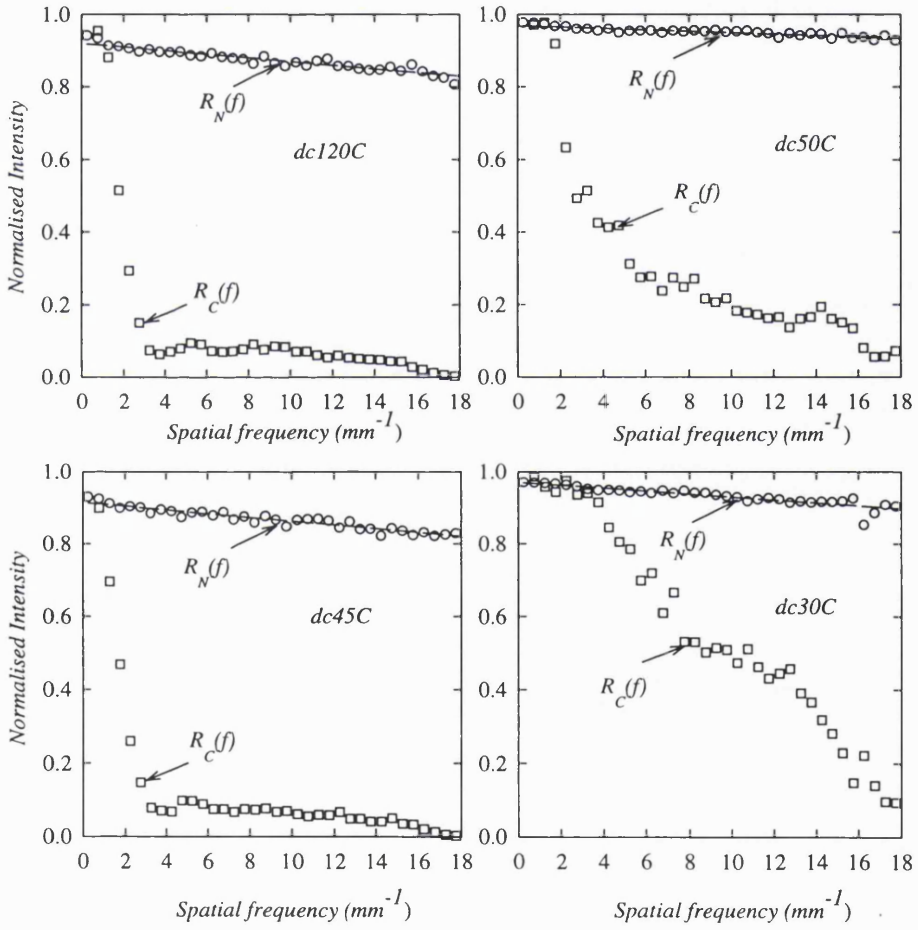

Figure 4.29 $R_N(f)$ and $R_C(f)$ for directly coated detectors

From Figure 4.29 $R_C(f)$ decreases rapidly with increased spatial frequency for all the detectors. This drop off in $R_C(f)$ is primarily due to direct hits in the CCD contributing

more to the noise than to the signal. As the thickness of the phosphor layer decreases and the CCD pixel size decreases, the relative contribution to signal from direct hits in the CCD increases so that $R_C(f)$ will drop of less suddenly with increasing spatial frequency.

Results show $R_C(f)$ decreases in value with increased spatial frequency, for all detectors. This shows that noise is passed more efficiently than the signal for these higher spatial frequencies

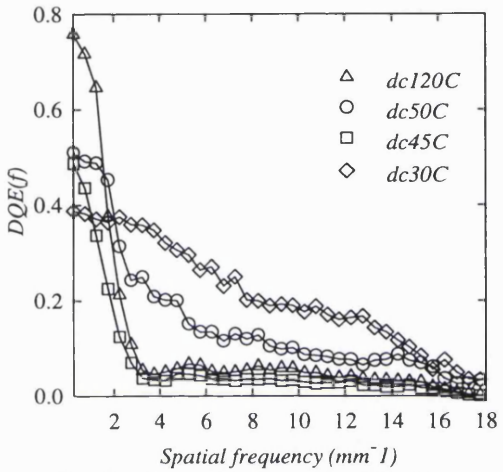

Figure 4.30 DQE(f) curves for directly coated detectors. Solid lines are straight lines between points, shown for clarity.

Plots of DQE(f) for the directly coated detectors are shown in Figure 4.30. Values for DQE(0) are close to the quantum detection efficiency of the detector hence detector dc120C has the largest value of DQE(0). For detectors dc120C and dc45C, as the spatial frequency increases the DQE drops of rapidly, this is caused by the drop in $R_C(f)$. For detectors dc50C and dc30C, the drop of in DQE is less compared to the other two detectors. This is because $R_C(f)$ drops off less for these detectors.

4.5.3 Results for fibre optical coupled detectors

Figure 4.31 shows plots of $R_N(f)$ and $R_C(f)$ for detector fo70C. These plots are typical of the plots obtained with the rest of the fibre optically coupled detectors. The high values of $R_N(f)$ show that the detector is quantum noise limited for all frequencies shown. $R_C(f)$

decreases with increased spatial frequency although the reduction is not as much as with the directly coupled detectors. This shows that the CCD is effectively shielded from direct hits in the CCD.

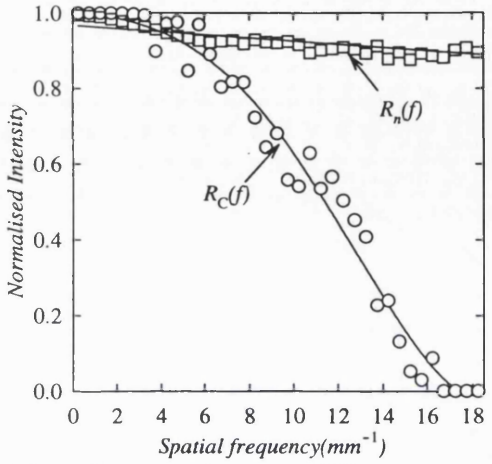

Figure 4.31 Plots of $R_C(f)$ and $R_N(f)$ for detector fo70C.

Figure 4.32 shows that $R_c(f)$ for detector fo50C is greater than that for detector fo50G. This is attributed to the fact that the CsI(Tl) phosphor used in detector fo50C ,unlike GdO_2S_2, is transparent so that each light burst should have a similar shape so there is less spatial variation in A_s.

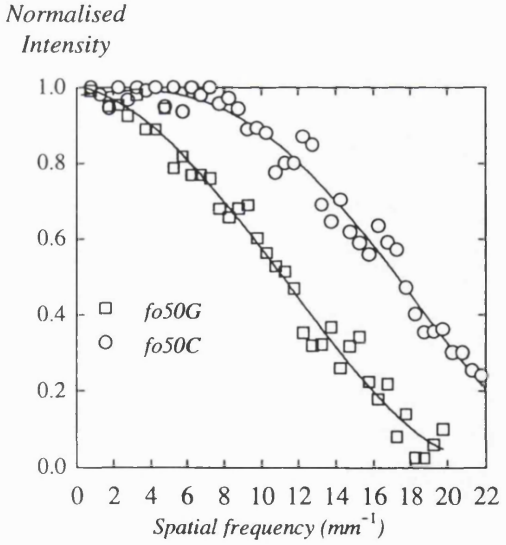

Figure 4.32 Plots of $R_C(f)$ for detectors fo50G and fo50C.

Figure 4.33 shows plots of DQE(f) for fibre optic coupled detectors. Detector fo130C has the largest value of DQE(f) for spatial frequencies < 5lp/mm. Between 5 and

13lp/mm detector fo70C has the largest value of DQE(f). Detector fo50C has the largest value of DQE(f) for spatial frequencies greater than 13lp/mm.

It can be seen that the largest values of DQE(0) are for detectors with the thickest phosphor layers and are close in value to the quantum detection efficiency for each detector. Also the shape of the DQE(f) plot drops off with increased spatial frequency for all the detectors and in general DQE(f) drops of more rapidly for detectors with the thicker phosphor layers.

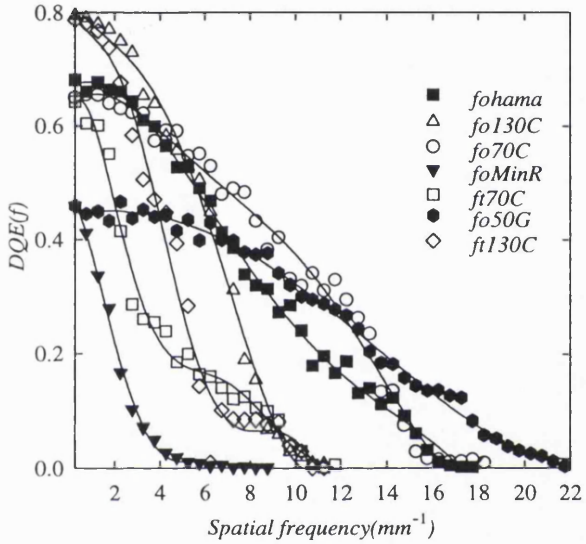

Figure 4.33 DQE(f) curves for fibre optical coupled detectors. Solid lines are regressions to the data.

4.5.4 Effect of absorbed dose upon DQE(f)

The absorbed dose in air at which the total NPS is measured has been shown to affect the spatial frequency at which images produced from the detector are x-ray quantum noise limited. This result is reiterated in Figure 4.34 where $R_N(f)$ drops off more rapidly for the lower dose level shown.

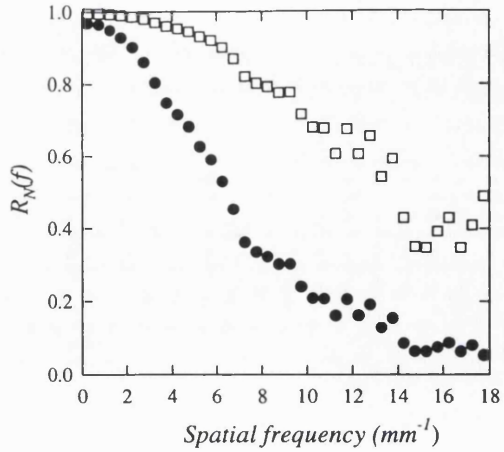

Figure 4.34 $R_{n(}$(f) curves for detector fohama. White squares correspond to a dose of 11mGy, black circles correspond to a dose of 0.787mGy.

Figure 4.35 shows the corresponding DQE curves for the two doses and it is evident that DQE is reduced at higher spatial frequencies for the lower dose.

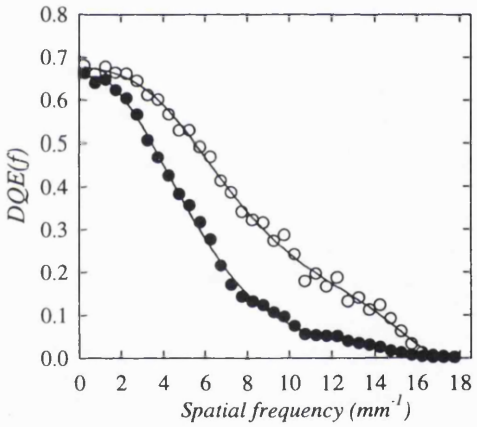

Figure 4.35 DQE(f) curves for detector fohama. White circles correspond to a dose of 11mGy, black circles correspond to a dose of 0.787mGy.

4.5.5 Methods of increasing DQE(f)

Analysis of the DQE(f) of detectors has shown DQE(f) can be maximised by

- Reducing the dark current noise W_D(f), by further cooling the CCD.

This would decrease the level of W_D(f) and would thereby increase R_N(f), the level to which the system was x-ray quantum noise limited, and hence DQE(f).

- Increasing $W_Q(f)$.

This would increase $R_N(f)$ and hence DQE(f). This can be achieved by increasing the gain in the number of optical quanta produced per incident x-ray and increasing the optical transmission efficiency of any fibre optic couplings used.

The use of a reflective coating in detector fohama has shown that $W_Q(f)$ can be increased without any degradation's in MTF.

- Producing higher MTF values.
- Increasing the quantum detection efficiency A_Q. This can be achieved by increasing phosphor screen thickness at the expense of MTF.
- Eliminating direct hits in the CCD.

4.5.6 Summary of DQE(f) results

The model of Nishikawa et al has been used to obtain plots of DQE(f) for the detectors under investigation. Plots of $R_N(f)$ show that the images produced from all detectors are x-ray quantum noise limited for all spatial frequencies for the exposures used.

An ideal detector would have a DQE(f) of 1 for all spatial frequencies of interest, it follows that detectors with high values of DQE(f) will produce images of greater 'quality' than detectors with low values of DQE(f). It has been shown that DQE at low spatial frequencies is determined by the quantum detection efficiency A_Q, of the phosphor layer. However as the phosphor layer thickness is increased to absorb more x-rays and to increase A_Q, DQE(f) drops of more rapidly because of the poorer MTF. This result means that a thinner phosphor layer may have larger values of DQE(f) at higher spatial frequencies than a thick phosphor.

DQE(f) was shown to be dose dependent, $R_N(f)$ drops off more rapidly for lower doses which has the effect of reducing the DQE at higher frequencies.

It is important to discover which values of spatial frequencies need to be maximised in order to improve detection/image quality of specific objects in specific imaging procedures. For example consider the DQE(f) curve for detector dc120C, it is perceived than this detector would be 'good' for imaging large objects - greater than 1mm in diameter say, however as the object becomes smaller the importance of higher spatial frequencies may increase so that a detector with DQE(f) curve similar in shape to detector fo70C (smaller at low spatial frequencies but larger at higher) may produce better detection/image quality. An investigation into how DQE(f) relates to image quality is presented in chapter 5.

4.6 Quantum accounting diagrams.

Quantum accounting diagrams (QAD) are used widely to evaluate imaging systems. These nomograms describe the imaging system in a series of cascaded stages. Each stage may correspond to either an increase in the number of quanta (e.g. conversion from x-ray to optical quanta in a phosphor) or a decrease (e.g. detection probability). The stage with the fewest quanta is called the 'quantum sink' limiting the pixel signal to noise ratio (SNR) to less than the square root of the number of quanta per pixel.

Cunningham et al (1994 a) have introduced a spatial frequency dependent QAD which includes effects due to spatial frequency of secondary quanta. An expression for the DQE of a hypothetical CCD based imaging system was derived based upon the gain, gain Poisson excess (related to the variance) and the MTF of each stage. A direct relationship was then shown to exist between the DQE and values in the QAD.

Their research has shown that secondary quantum sinks that may be present at higher spatial frequencies severely limit a system's ability to resolve high frequency detail. Using a Monte Carlo simulation images were produced from a hypothetical CCD based detector system. They found that for a mean signal level of 50 quanta per pixel the secondary quantum sink results in a visible deterioration of image quality at a specified frequency when the QAD at that frequency is less than approximately five times the primary quantum sink value (Cunningham et al. 1994 b). The application of this work to a CCD based mammography system is given in the below section.

4.6.1 Model of spatial frequency dependent DQE(f)

The spatial frequency dependent DQE of an M stage imaging system (Westmore et al 1994a) is given in Eq. 4.42 where $\varepsilon_{g\,i}$ is the Poisson excess term in the gain of the stage i, $T_i(f)$ is the MTF of stage i, $P_i(f)$ is the spatial frequency QAD and is given in Eq. 4.43 where $<g_j>$ is the mean gain of stage j, $T_j(f)$ is the MTF of stage j and Π denotes the product of mean gains and MTFs for all of the M stages.

$$DQE_{1,M}(f) = \frac{1}{1+\sum_{i=1}^{M}\frac{1+\varepsilon_{gi}|T_i(f)|^2}{P_i(f)}}$$

Eq. 4.42

$$P_i(f) = \prod_{j=1}^{M} < g_j > |T_j(f)|^2$$

Eq. 4.43

4.6.1.1 Poisson excess of the gain

If the variance in the value of g_i, is σ^2_{gi} for a Poisson distribution then $<g_i> = \sigma^2_{gi}$. The Poisson excess describes the relative amount by which the variance of the distribution is in excess of the mean value and is given in Eq. 4.44.

$$\varepsilon_{gi} = \frac{\sigma^2_{gi}}{< g_i >} - 1$$

Eq. 4.44

There are three special cases which are identified to help interpret the meaning of the excess.

- If g_i is truly Poisson distributed then $\sigma^2_{gi} = <g_i>$ and $\varepsilon_{gi} = 0$.
- If g_i is a deterministic gain with zero statistical error $\sigma^2_{gi} = 0$ and $\varepsilon_{gi} = -1$.
- if g_i represents a binary selection process such as a interaction probability or coupling efficiency then $\sigma_{gi}^2 = g_i(1-g_i)$ and $\varepsilon_{gi}=-g_i$.

If g represents a conversion from x-ray quanta to optical quanta in thin screens ε_g is related to the Swank factor A_s, and is given in Eq. 4.45.

$$\varepsilon_g = g(\frac{1}{A_s} - 1) - 1$$

Eq. 4.45

For a full derivation of all these equations the reader is referred to Westmore andCunningham 1994a&b.

* Insert Eq. 4.42

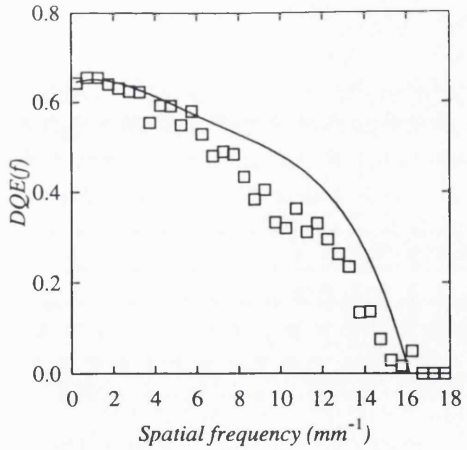

Figure 4.36 Plots of experimental DQE(f) (squares) and theoretical DQE(f) (solid line) obtained from the model of Westmore and Cunningham for detector fo70C.

Figure 4.36 shows experiment DQE(f) with the theoretical DQE(f) obtained using the model described above for detector fo70C. The theoretical curve was obtained by considering the detection processes to be split into 5 stages. These stages together with values of $<g>$ and ε_g are detailed in Table 4.3. The overall detector theoretical DQE(f) was calculated using. It can be seen that there is good agreement between the two plots even though additive detector noise, such as dark current noise is ignored in the theoretical model.

Table 4.3 Stages used in theoretical calculation of DQE(f) for detector fo70C.

STAGE No. DESCRIPTION	*GAIN*	*POISSON EXCESS*	*MTF(f*
0. Xrays Incident			
1. Absorption of x-rays in phosphor	η=0.68	-η	-
2. Emission of photons in phosphor	G=455	47	$T_p(f)$
3. Transmission from phosphor to the CCD	t=0.45	-t	
4. MTF due to CCD aperture function	-	-	$T_c(f)$
5. Detection in the CCD	α=0.31	-α	-

The values obtained from the model represent a theoretical limit of DQE(f), that is the experimental results would be the identical if the detector is x-ray quantum noise limited and the signal is passed through the system as efficiently as noise.

4.6.1.2 $P_i(f)$ the spatial frequency dependent QAD

The spatial frequency dependent QAD of detectors fo70C and ft70C are shown in Figure 4.37 and Figure 4.38 respectively. The 5 stages in the QAD are the same as in Table 4.3. From the results it can be observed that for zero frequency there is a primary quantum sink at the x-ray detection stage for both detectors. For higher spatial frequencies the values in the QAD are considerably less than the zero frequency values, as they decrease with the square of the total system MTF. Secondary quantum sinks exist at stage 5 for both detectors (between 10 and 14 lp/mm and 6 and 8 lp/mm for fo70C and ft70C respectively). This means that the fundamental limitations to image noise (neglecting detector noise) is no longer dominated by fluctuations in the number of x-rays detected at these frequencies.

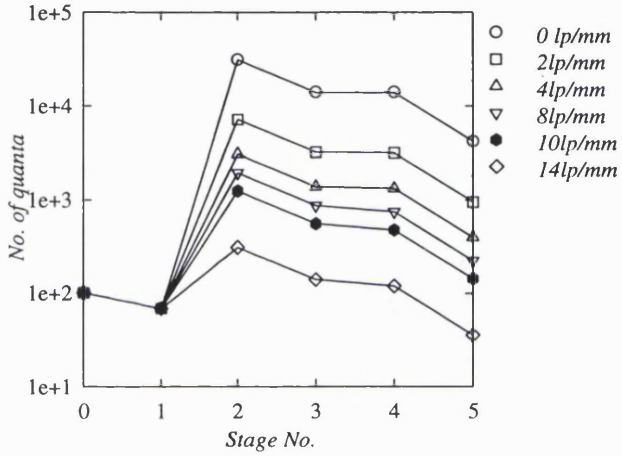

Figure 4.37 spatial frequency dependent QAD of the detector fo70C.

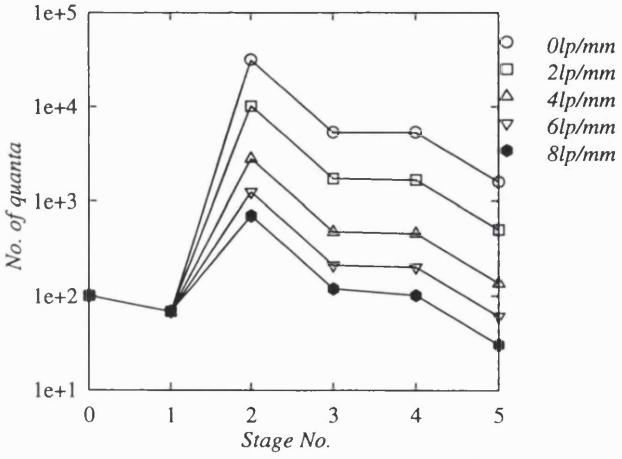

Figure 4.38 spatial frequency dependent QAD for detector ft70C

4.6.2 Summary of QAD results.

Westmore and Cunninghams model for the spatial frequency quantum accounting diagram has been used to evaluate detectors. The model used to investigate the presence of secondary quantum sinks in detectors. Good agreement was found between theoretical DQE(f) and experimental DQE(f) results.

4.7 Conclusions

The effects of direct hits in the CCD have been modelled. These have been found to improve the high frequency response in the MTF measurements, but also increase the noise power at higher spatial frequencies. DQE(f) curves have shown that the effects of directs hits are to reduce DQE(f) at higher spatial frequencies. These results indicate that direct hits need to be removed for imaging tasks which require high values of DQE(f) at high spatial frequencies. The removal of direct hits can be achieved by using a fibre optic faceplate between the phosphor layer and the CCD. This has been shown to practically eliminate all direct hits in the CCD.

The MTF of fibre optically coupled detectors has been shown to be dominated by the contribution to blur from light spread in the phosphor. The rate at which MTF decreases has been shown to be greatest for the thicker phosphor layers. The structure of the phosphor layer used in detector fohama has been shown to produce a MTF curve similar to one that would be produced from a homogeneous phosphor layer structure of the same thickness. It is concluded that the structure improves the light output from the phosphor without increased spatial blurring.

Measurements of NPS have shown that for high dose levels the detectors are x-ray quantum noise limited at all spatial frequencies. For lower doses noise due to fluctuations in dark current may dominate at higher spatial frequencies. The noise due to

secondary quantum fluctuations has been shown to be a factor of 10 smaller than noise due to dark current.

Measurements of DQE(f) have been shown to be dose dependent for the detectors used in this project. This is because for low doses the detector will not produce x-ray quantum noise limited images for all spatial frequencies, or alternatively, noise due to dark current fluctuations are dominant at high spatial frequencies. Analysis of the DQE(f) of detectors has shown DQE(f) can be maximised by

1. Reducing the dark current noise $W_D(f)$, by further cooling the CCD.
2. Increasing $W_Q(f)$. This can be achieved by increasing the gain in the number of optical quanta produced per incident x-ray and increasing the optical transmission efficiency of any fibre optic couplings used.
3. Producing higher MTF values.
4. Increasing the quantum detection efficiency A_Q.
5. Eliminating direct hits in the CCD.

CHAPTER 5

5. Application to mammography

This chapter contains an investigation into the imaging performance of CCD based detectors for mammography. The design of the system using CCDs operated in Time Delayed Integration mode is outlined. Monte Carlo modelling of the system to predict optimum x-ray energies and the effect of collimator slot width on scatter to primary ratio are presented.

Noise levels in the images obtained from the detectors are measured for typical exposures used in mammography and the effects on the detector DQE(f) are investigated.

The results of image quality measurements obtained with the Leeds TORMAX breast phantom are presented and are compared with the DQE(f) curves for the detectors. Finally a prescription for the detector design is discussed.

5.1 Design of system

It is envisaged that the digital mammography system would look like something shown in Figure 5.1. The detection system would scan across the compressed breast with the CCDs operated in TDI (Time Delayed Integration) mode and the x-ray beam would be collimated pre-patient to reduce scattered x-rays. Care would be needed in ensuring that the detector plane extended as close to the chest wall as was possible. The investigation of the scanning effects in a digital mammography system are presented in Court (1995).

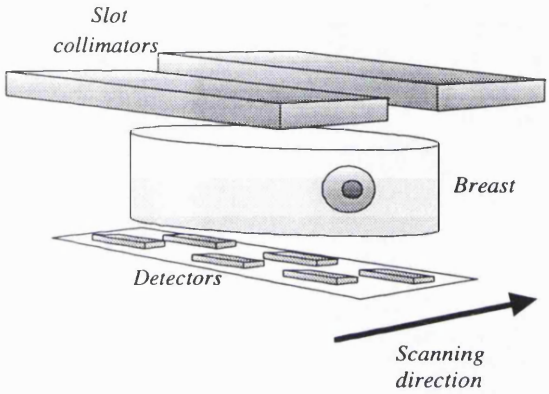

Figure 5.1 diagram of proposed digital mammography system.

The collimators would be made of lead and of sufficient thickness to prevent any x-rays penetrating. With a CCD system the choice of slot width becomes a trade off between the size of the CCD, the amount of available x-ray flux and the required decrease in scatter to primary ratio. The choice of the thickness of the slot has been investigated more deeply by Nishikawa (1989) and Court (1995).

Figure 5.2 shows two options for the alignment of the CCDs to make up the detection system. Figure 5.2(a) shows the CCDs arranged in a mosaic pattern with slight overlap between adjacent CCDs to overcome the dead-space due to packaging and Figure 5.2(b) shows fibre optic coupled CCDs butted together. The imaging area covered by the detection system would need to be at least 24 cm by 18cm. This would mean a minimum of 6 15_11 CCDs would be needed to cover the image area for configuration (a).

In both configurations the CCDs would be operated in Time Delay and Integration mode where all the CCDs are continuously read out whilst they are scanned across the subject. Each configuration has its own merits. The advantages of configuration (b) over (a) include

1. Smaller number of CCDs required -hence less need to be readout as fast.

2. Each image produced will have fewer pixels therefore memory requirements for image acquisition and storage will be smaller. Obviously there is a limit to the largest pixel size which can be used to produce good quality mammography and the pixel size in the final image will depend upon the inherent CCD pixel size and the magnification of the fibre optic coupling. Because there are fewer pixels the scanning time of the system will be smaller.

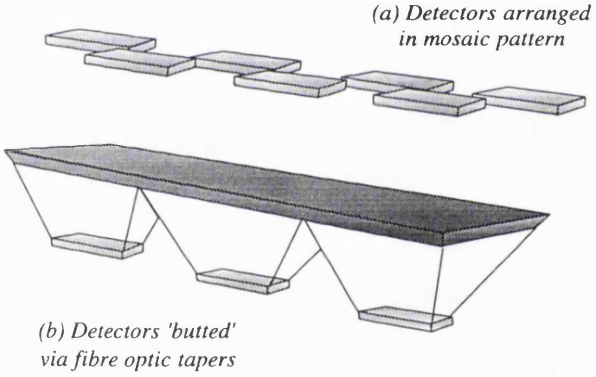

Figure 5.2CCD configurations for digital mammography scanning system.

The disadvantages of system (b) over system (a) include

1. There is a limit to the amount of magnification that can be used. De-magnifying fibre optic tapers have a lower transmission efficiency compared to one to one fibre optic face-plates This reduces $W_Q(f)$ and reduces DQE(f) for detectors with high $W_D(f)$. The limiting spatial resolution is dependent upon the magnification used.

System (a) will produce images of higher quality over system (b) the choice of system becomes a trade off between the relative costs of each system and their relative performances.

5.2 Monte Carlo simulations

Monte Carlo techniques have previously been applied to mammography (Dance 1980, 1981) to calculate radiation dose and optimum x-ray energy for film/screen systems and xeroradiography systems. In this work a similar approach was used to simulate mammography for digital detectors.
The EGS4 code system (Nelson et al 1985) was used to simulate the x-ray interaction processes in the breast and detector for the geometry shown in Figure 5.3.

The size and composition of the female breast varies widely. In this simulation the breast was assumed to be cylindrical in shape with a cross sectional radius of 6cm (this is approximately equal to Dances medium compressed breast). The composition of the breast was 50% fat and 50% water by weight (composition recommended by White et al. 1977). The simulated calcification was cylindrical in shape with a 100μm cross sectional diameter and 100μm height and was composed of calcium hydroxyappatite.

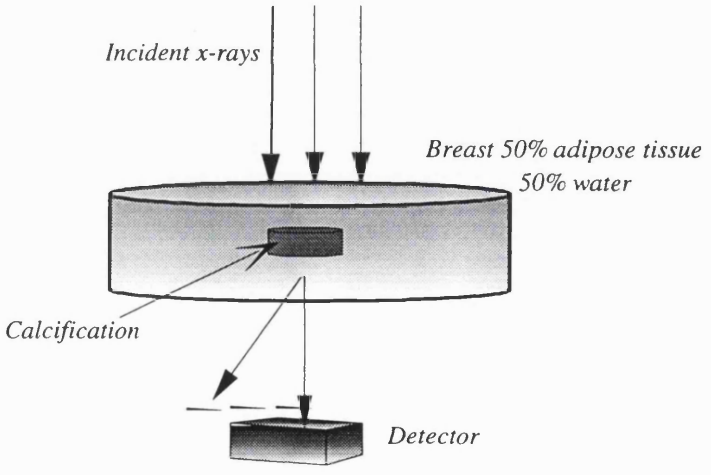

Figure 5.3 diagram of geometry used for the Monte Carlo simulation.

These size were chosen as they represent the smallest calcification that can hoped to be detected with conventional film-screen mammography.

The radiation dose to the breast or breast dose was calculated as the ratio of the energy absorbed (J) in the breast and the mass of the breast (kg) and was quantified in terms of Grays since 1Gy is equal to 1 joule/kg.

The detector consisted of an infinite slab of CsI which was 100μm thick (represents a typical thickness of phosphor) and was split up in to pixels or bins, shown in Figure 5.4. Energy deposited by an interacting x-ray was summed in the appropriate pixel so that an image of the calcification in the breast was eventually formed. The simulation considered a monoenergetic, parallel and uniform beam of x-ray's incident on the breast covering a field area of 1cm by 1 cm. The x-ray energies used in the simulation ranged from 10 keV to 40keV in 2keV intervals.

The breast dose and energy deposited in the detector was calculated. Subsequent generation of scintillation photons in the phosphor layer was ignored and it was assumed that all the energy deposited in the phosphor layer was converted to electrons in the CCD. When the breast dose reached approximately 1mGy the x-rays were stopped and the image obtained was evaluated.

5.2.1 Image quality assessment and evaluation

The process by which an observer arrives at a diagnosis from viewing an image is very complicated. Generally , the steps in this process are detection, localisation and classification. For detection of a lesion, such as a calcification in mammography, the system resolution must be just good enough to resolve the lesion, but the SNR should be as large as possible. Localisation of the lesion with respect to other anatomical features in the image and classification of it as a normal structure or some particular pathology places an increased burden on the resolution (Barrett and Swindell, 1981). This study is

aimed at investigating the effects of varying x-ray energy, pixel size and field width upon the probability of detection or detectability of a calcification.

The detection probability or detectability was quantified in terms of detail signal to noise ratio (dSNR). This was calculated using the following equation

$$\text{detail SNR} = \frac{s - b}{\sigma_s + \sigma_b}$$

Eq. 5.1

where s is the mean pixel value in the calcification shadow, b is the mean pixel value in the background σ_s and σ_b are the standard deviations in the signal and background pixel values respectively. A total of 50 pixels where used to calculate the mean background pixel value. The number of pixels used to calculate the mean signal pixel value depended upon the pixel size used.

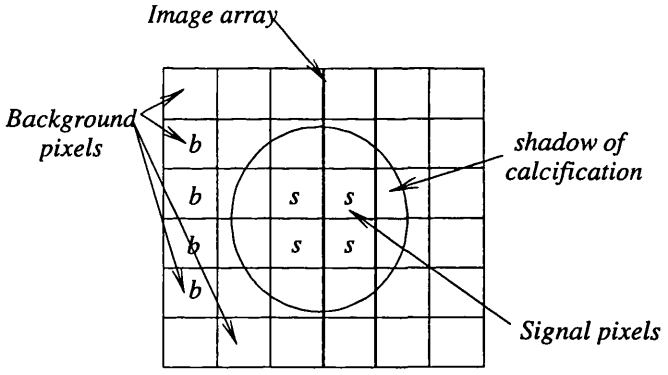

Figure 5.4 image of calcification obtained in the simulation.

In order to reduce the uncertainty in the value of dSNR the simulation was repeated many times (using a different 'seed' value) and a mean value was calculated. Errors on values of dSNR are less than 1%.

The definition of dSNR differs from the standard definition of signal to noise ratio because the noise is calculated by finding the standard deviation of background fluctuations in pixel values and not the standard deviation of background fluctuations

over the area of the object. This is not a problem however because the noise associated with the fluctuations over the object area is proportional to the pixel noise.

The simulation was used to investigate the effects of varying pixel size ,incident x-ray energy, and the effects of varying field width upon dSNR.

5.2.2 Effect of pixel size on dSNR

If the pixel size in the imaging array is of the order of the size of object to be imaged then the dSNR will depend strongly upon the position of the image relative to the detector array. Figure 5.5 shows the two extreme cases for alignment of the image relative to the detector array. For the first case the calcification shadow covers one whole pixel. In the second case the shadow of the calcification equally overlaps four adjacent pixels. The dSNR was calculated in these two extreme cases for pixel sizes ranging from 25μm to 100μm for an incident energy of 21keV and a compressed breast thickness of 4cm. Results shown in Figure 5.6 show that for the first case dSNR increases with increasing pixel size as expected because more x-rays are detected per pixel, increasing the signal and reducing the noise, as the pixel size increases. For the second case there is a maximum dSNR for a pixel size of 50 μm.

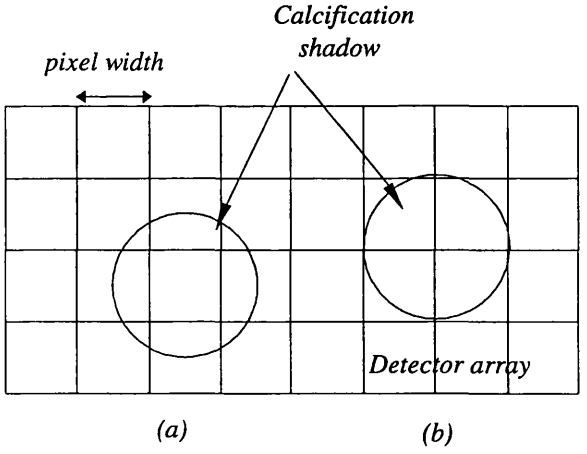

Figure 5.5 alignment of calcification shadow with detector array (a) first case (b) second case.

From this simple simulation it can be deduced that the best pixel size to use for detection is about the size of the object. However things are not quite that simple; as mentioned earlier, it is important in some cases for the observer to classify lesions in order to make a correct diagnosis. The shape and edges of calcifications in the breast carry valuable diagnostic information which may not be present for this pixel size.

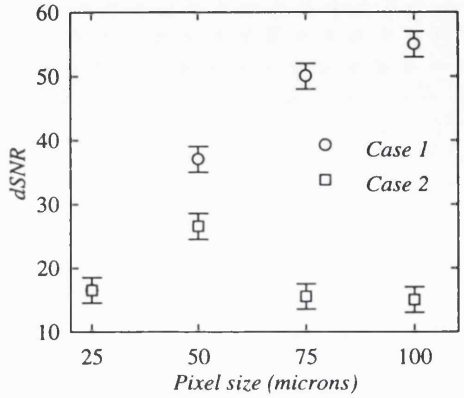

Figure 5.6 dSNR as a function of pixel size for 100μm diameter calcification.

Also practical concerns over system design are important, as pixel size decreases the number of pixels in the whole image of the breast will increase and the memory requirements for image storage/display will also increase.

This simulation assumes that the CCD pixel size is the main limitation to spatial resolution, however results in chapter 4 show that the spread of scintillation photons in the phosphor layer is the main limitation. Nevertheless it may be inferred that in order to maximise the detection probability of the 100μm calcification the detector needs to have an effective sampling aperture of 50μm. This means that the detector should be able to produce images which can resolve spatial frequencies in excess of 10lp/mm.

5.2.3 Variation of dSNR with incident x-ray energy

The effects of varying the incident energy from, 15keV to 40keV in 1keV steps, on values of dSNR are shown in Figure 5.7. Results are presented for three thickness' of compressed breast for a field size of 1cm by 1cm (small enough so that simulation times

were not to large but large enough to obtain the required number of background pixels for calculation of dSNR) and a pixel size of 50μm. Values of dSNR were calculated for the 2nd case alignment shown in Figure 5.5.

Results show that for each thickness of compressed breast dSNR increases with incident energy until a maximum is reached and then decreases at higher energies .The energy corresponding to this maximum is dependent on the thickness of compressed breast.

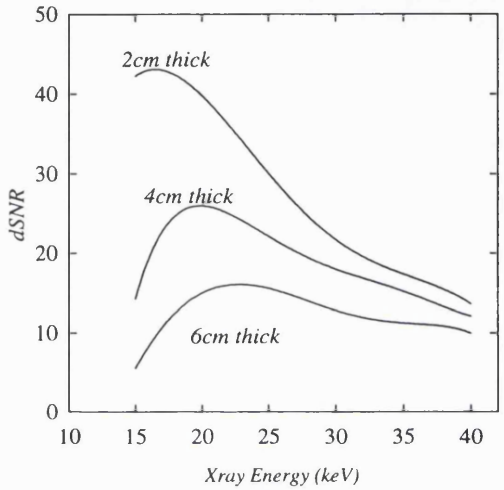

Figure 5.7 Variation of dSNR with incident x-ray energy for 2cm, 4cm and 6cm thick compressed breasts.

For low incident energies, as the incident x-ray energy increases more x-rays penetrate the breast and interact in the detector increasing dSNR. For higher incident energies the decrease in dSNR is due to the decreasing radiological contrast between the calcification and the background tissues and decreasing detector quantum efficiency at these energies..

Maximum dSNR values correspond to about 17-18 keV, 19-20 keV and 22-23 keV for the 2cm , 4cm and 6cm thick compressed breast respectively. These results compare well with results obtained by D. Dance and Day (1981).
The effective energy of a 28kVp molybdenum x-ray spectrum with molybdenum filtration typically used in mammography is about 17.5 keV (primarily due to the predominance of characteristic photons from molybdenum) and is suited for imaging

thinner breasts. However for thicker breasts it is possible that image quality could be improved by increasing the effective energy of the incident x-ray spectrum. This could be achieved by using a target with a higher characteristic photon energies.

Recently Siemens has introduced a x-ray tube for mammography which offers a choice of either molybdenum filtration or rhodium filtration which can be selected depending upon the thickness of the breast.

5.3 Comparison of imaging performance of detectors using a breast phantom

Images of a breast phantom were obtained to directly compare the imaging performance of the detectors and assess their application to digital mammography.

Images were obtained for each detector under standard exposure conditions used in mammography. Care was taken to ensure images were obtained under identical conditions for each detector. The images obtained were evaluated in terms of detail signal to noise ratio (SNR) which provided a method of quantifying the 'quality ' of the image.

5.3.1 Leeds TOR(MAX) Breast phantom

The TORMAX breast phantom consists of a semi-circular test plate of 22cm diameter approximately 1cm thick, which is used in conjunction with an attenuator stack of acrylic plates (three of 1cm thickness and two of 0.5cm thickness) to provide the appropriate absorption, scatter and geometrical unsharpness in test exposures. The test plate contains several different types of detail which provide information about unsharpness, low contrast sensitivity, small-detail visibility and noise in the test image. The layout of the phantom test plate is shown in Figure 5.8.

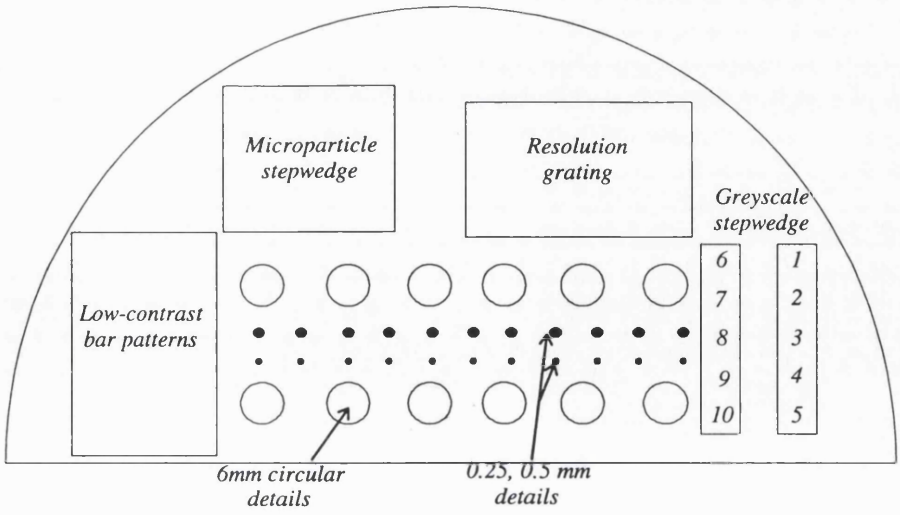

Figure 5.8 Layout of the details in the TOR(MAX) test plate.

The details in the test plate are as follows

1. High-contrast resolution gratings. These provide measurements of unsharpness or resolution limit (up to 20lp/mm) in perpendicular directions

2. Low- contrast bar patterns. These details provide a measurement of the sensitivity of a system in imaging low contrast filamentary structures within the breast.

3. 6 mm circular low-contrast details. These details provide a measurement of the low-contrast sensitivity of a system, which is relevant to the detection of tumourous masses within the breast. Twelve circular details 6mm in diameter form a series of diminishing contrasts tabulated in Table 5.1.

Table 5.1 Nominal contrasts of 6mm details under calibrated X-ray beam conditions of 28kVp.

Detail No.	*Contrast (%)t*	*Detail No.*	*Contrast (%)*
1	8.5	7	1.2
2	5.5	8	0.83
3	3.8	9	0.58
4	2.6	10	0.46
5	2.0	11	0.32
6	1.6	12	0.24

4. 0.5 mm high-contrast details.

Table 5.2 Nominal contrasts of 0.5 and 0.25 mm details

Detail No.	*Contrast (%)*	*Detail No.*	*Contrast (%)*
1	37	7	8.3
2	33	8	5.4
3	24	9	2.7
4	20	10	2.0
5	16	11	1.3
6	11		

5. 0.25 mm high-contrast details. The 0.5 and 0.25 mm details provide a measurement of small detail visibility which is relevant to the detection of punctate calcifications within the breast. Nominal contrasts measured under calibrated X-ray beam conditions (28kVp) are tabulated in Table 5.2.

6. Ten-point grey-scale step-wedge.

7. Micro-particle step-wedge. A step wedge incorporating small irregular shaped particles to produce a pattern of fine detail imaged in areas of different background density, which is relevant to the detection of microcalcifcations in the breast.

The attenuator stack comprises three semi circular acrylic plates, 24cm in diameter and 1cm thick, plus two plates 0.5cm thick, providing attenuating and scattering material. These can be stacked together and aligned by two pegs passing through holes in the plates.

In this investigation the recommended configuration of the phantom was used. This was to place the test plate on top of the attenuator stack so that scatter and geometrical unsharpness were present to maximum effect. A 3.5 cm attenuator stack was used providing X-ray attenuation equivalent to a 5cm compressed breast when combined with the test plate.

5.3.2 Method used

A diagram of the experimental set-up used for obtaining the phantom images is shown in Figure 5.9. Due to the small size of the CCDs it was not possible to image the whole of the phantom and it was necessary to use a scanning stage to move the phantom so that all areas could be imaged. The scanning system comprised two translation units arranged perpendicularly to each other with stepper motors attached. The stepper motors were controlled by a Digiplan unit which interfaced to a PC via the parallel interface. Control of the stepper motors was done using a purpose written computer program. The program allowed the user to move the phantom in 2.5 μm steps in either direction.

With the test plate being opaque it was impossible to know exactly what part of the phantom was being imaged. This problem was solved by taking a conventional screen-film radiograph of the test plate and using it as a reference map for the details.

For the purpose of this investigation three types of detail in the phantom were imaged the 6mm low contrast detail, the 500μm high contrast detail and the 250μm high contrast detail.

5.3.2.1 Slot beam collimator

The slot beam collimator consisted of sheets of lead 0.5mm thick. This thickness was sufficient to attenuate all x-rays incident for the 28kVp spectrum. The collimator was placed before the breast phantom to restrict the field width of the beam. There is no requirement for post patient collimation with scanning detectors as the small width of the detectors provides inherent collimation.

The width of the slot used to collimate the beam could be varied from 2cm to 10cm.

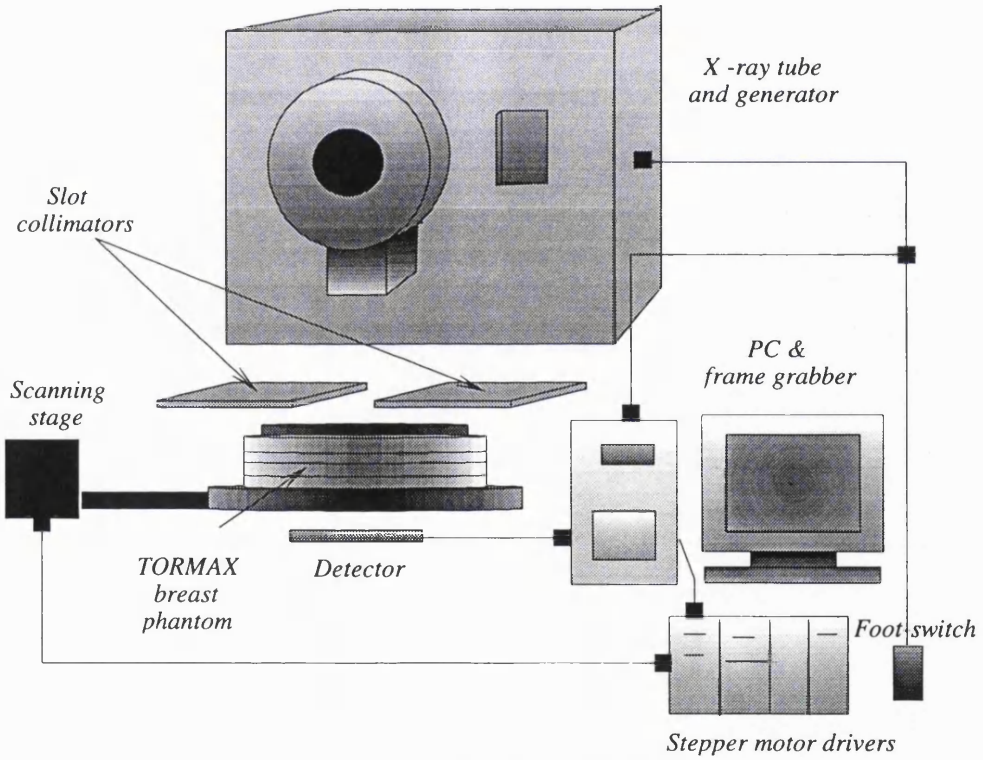

Figure 5.9 Experimental set up for breast phantom measurements.

5.3.2.2 Exposure conditions

All images were obtained with the same exposure conditions a 28kVp Mo:Mo spectrum with 30μm inherent filtration.

The mean breast dose for a standard breast was estimated using the method recommended by the IPSM (1989) from exposure measurements. The mean glandular dose to the standard breast is calculated using the following eqtn

$$\text{mean glandular breast dose} = Kpg \qquad \textbf{Eq. 5.2}$$

where p converts the incident air kerma to the perspex phantom to that for the standard breast and g converts the incident air kerma for the standard breast to mean glandular dose. Both of these values were obtained from data published by D. Dance (1990).

Throughout the measurements the focal spot to detector distance was kept constant at 620mm and the detector was placed as close as possible to the exit surface of the phantom (<3mm away)

5.3.3 Image analysis

Once an image was obtained it was corrected for pixel offset and gain variations. The image was then analysed using a program called XDISPIM. In this program user defined areas of interest (AOI) were defined allowing the calculation of the average pixel value, sum of pixel values, standard deviation and range of pixel values within that AOI. The detail signal was calculated by integrating the pixel values within each AOI and subtracting the average of the background AOI's from the average of the signal AOIs. The detail SNR was calculated using Eq. 5.3

$$dSNR = \frac{\overline{\text{Signal AOI}} - \overline{\text{Background AOI}}}{\text{S.D of Background AOI}}$$

Eq. 5.3

where $\overline{\text{Signal AOI}}$ and $\overline{\text{Background AOI}}$ are the average value of the sums of pixel values within the signal AOIs and background AOIs, S.D of background AOI is the standard deviation of the sums of pixel values within the background AOIs. To reduce the uncertainty it was necessary to sample the background and signal in the image a large number of times. For the 6mm low contrast detail, 6 signal AOIs and 24 background AOIs per image were used (shown in Figure 5.10) to calculate values of detail signal and noise and three images were used. The biggest uncertainty in the calculation of dSNR is the calculation of image noise and this uncertainty was estimated as 11%.

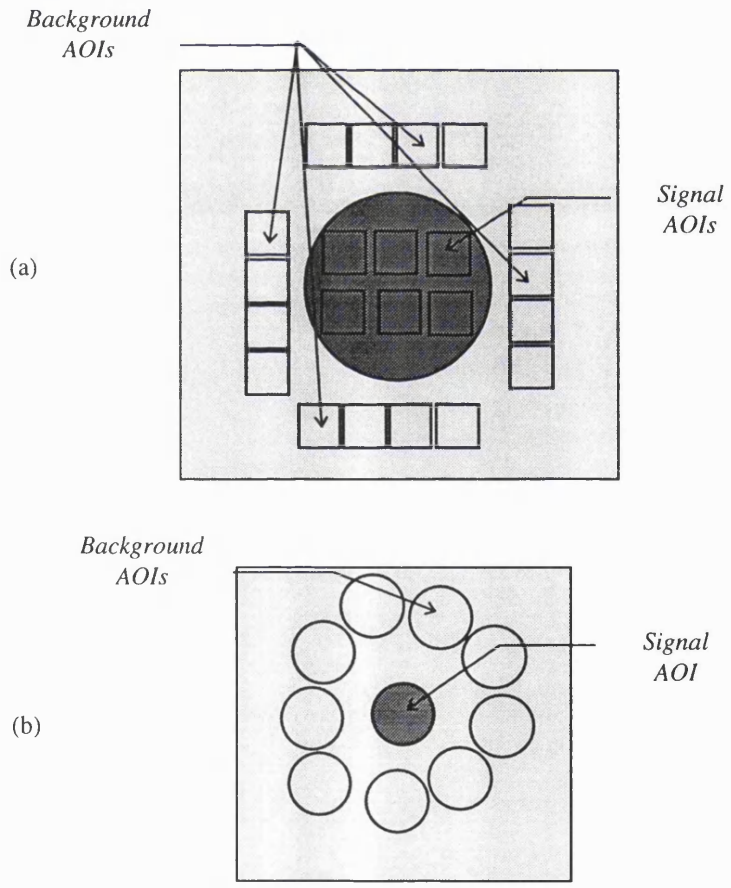

Figure 5.10 diagrams showing AOIs used for SNR calculation in the case of (a) 6mm low contrast detail, (b) 500 and 250μm high contrast details.

For the 500μm and 250μm high contrast details the signal AOI covered the whole of the image of the detail as shown in Figure 5.10. For the lower contrast details images were taken using a large exposure so that the signal AOI could be defined easily, then an image was retaken for the correct exposure, preserving the defined AOI. Again the main uncertainty is the calculation of image noise and this is estimated to be 13%.

5.3.4 Scatter rejection using slot beam collimation

The variation of signal was measured as a function of the slot width used in the imaging system. Images were taken for a constant breast dose of 2.2mGy and the average background intensity was calculated for slot widths ranging from 2cm to 10 cm. Separate measurements of exposure were made simultaneously using an air ionisation chamber (details of which are described in chapter 3) and were used to confirm the stability of the x-ray tube output for each image taken. The geometry for the measurement is shown in Figure 5.11.

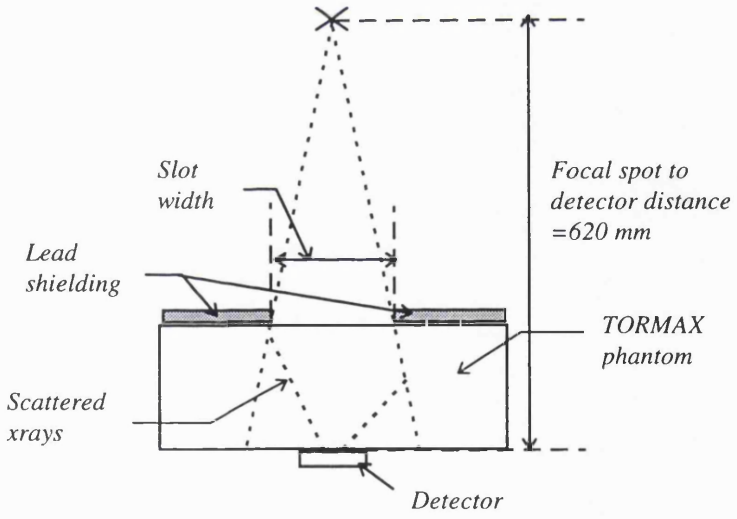

Figure 5.11 geometry for scatter rejection measurements.

Figure 5.12 shows the variation of the mean background signal as a function of slot width. The measured point for a slot width of 22cm represents images obtained without collimation. It can be observed that there is a 33% reduction in background signal as the slot width is reduced from 10cm to 2cm. This reduction in signal is attributed to the

prevention of radiation being scattered into the detector from outside the detector field of view as the slot width is reduced.

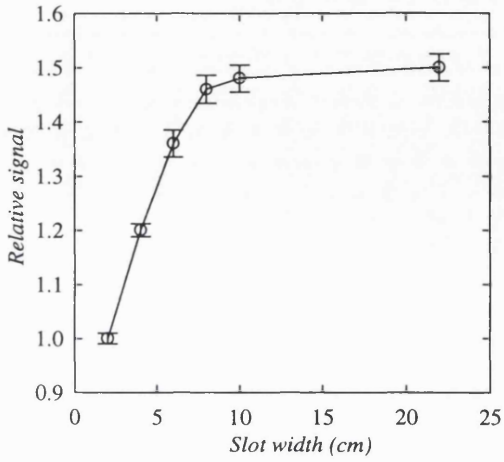

Figure 5.12 Relative mean background signal as a function of slot width for detector fo130C

5.3.5 Variation of SNR with breast dose

Images of the 8.5% contrast, 6mm diameter detail were taken for a set of breast doses ranging for .23mGy to 4.4mGy with a 2cm slot width . These images were used to

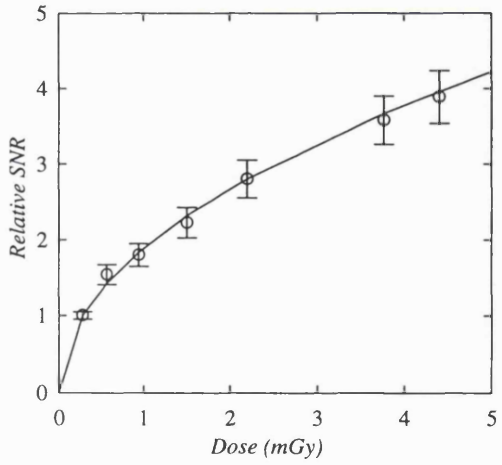

Figure 5.13 Variation of SNR with mean glandular breast dose for 6mm diameter detail with 8.5% contrast (for detector fo130C). Solid line is F=sqrt(dose)

calculate the SNR for each breast dose. The relative increase in SNR with increasing breast dose is shown in Figure 5.13. Also shown is a plot of $f(x)=x^{1/2}$ mapped to the first point on the graph. It can be observed that the measured SNR of the detail increases in a

manner related to the square root of the breast dose, as expected for quantum noise limited images.

5.3.6 Variation of SNR with detail contrast

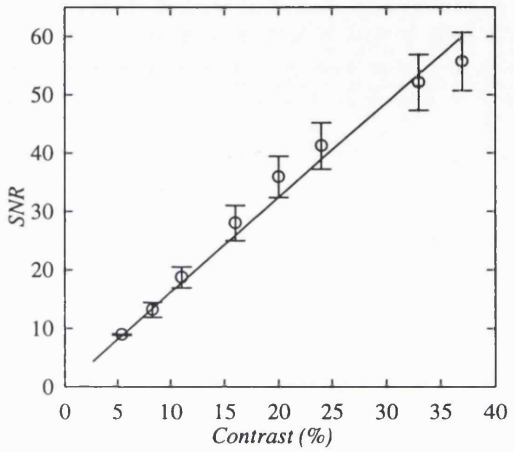

Figure 5.14 Variation of SNR with the contrast of the 500μm diameter detail(for detector fo130C).

Figure 5.14 shows the variation of measured SNR with detail contrast. Images were taken of the 500μm details with contrasts ranging from 5 to 37%. All images were obtained for a breast dose of 2.2mGy and a slot width of 2cm. Results show that SNR varies linearly with the detail contrast which is expected for a quantum noise limited system.

5.3.7 Results and discussion of dSNR analysis for detectors

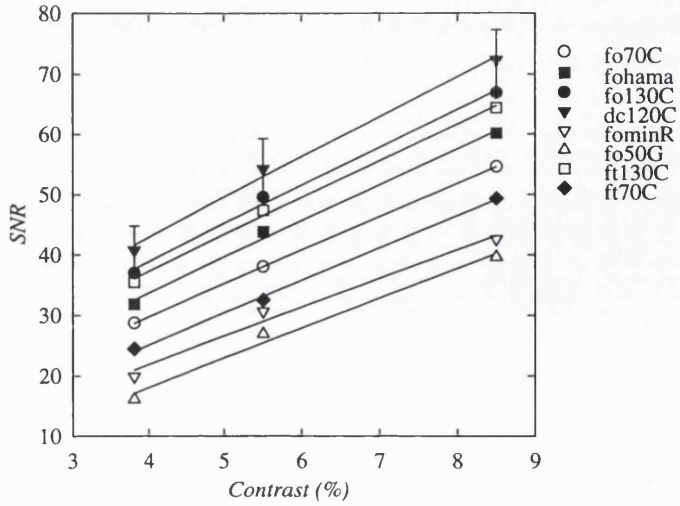

Figure 5.15 SNR measurements of 6mm diameter details for 8 different detectors.

The variation of dSNR with detail contrast for the 6mm diameter details is shown in Figure 5.15. It can be seen that detector dc120C produces images with the highest dSNR and detector fo50G produces images with the lowest dSNR. It was found that in general detectors with the largest values of quantum efficiency A_Q, produce the highest values of dSNR for the 6mm diameter details.

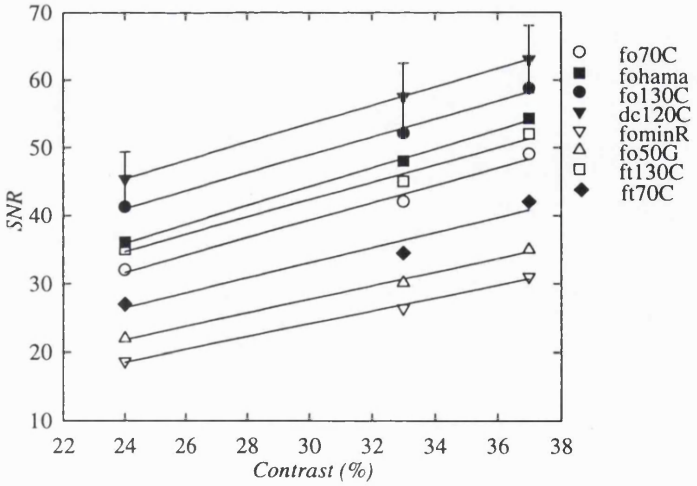

Figure 5.16 SNR measurements of 500μm diameter details for 8 different detectors.

The variation of dSNR with contrast for the 500μm diameter details is shown in Figure 5.16. Again detector dc120C produces images with the highest values of dSNR.

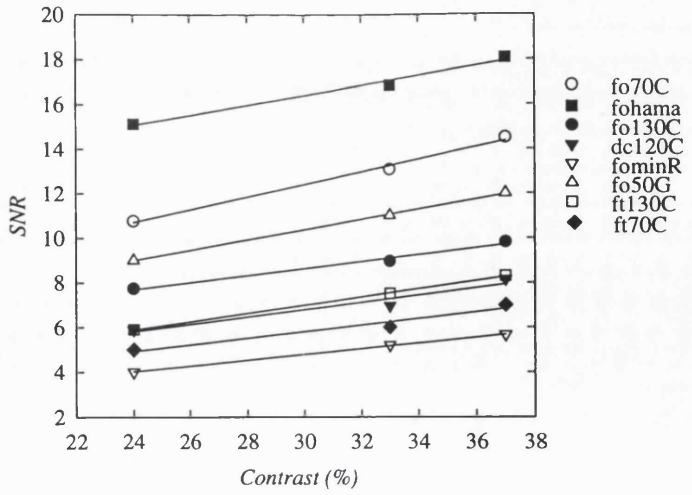

Figure 5.17 SNR measurements of 250μm diameter details for 8 different detectors.

The variation of dSNR with contrast for the 250μm diameter details is shown in Figure 5.17. It can be seen that detector fohama produces images with the highest dSNR.

A comparison between the values of dSNR and DQE(f) for detectors, measured for the same dose, is presented in the next section.

5.3.8 Influence of DQE(f) upon dSNR measurements.

The influence of DQE(f) upon the dSNR measurements was investigated by obtaining DQE(f) curves for the same dose as used for obtaining the phantom images

Figure 5.18 shows DQE(f) and dSNR measurements for detectors fo130C and dc120C. It can be seen that detectors dc120C and fo130C produce images with similar dSNR values for the 6mm and 500μm diameter objects. However detector fo130C produces images with consistently higher dSNR values for the 250μm diameter objects.

Figure 5.18 shows DQE(f) curves for the two detectors which were obtained for the same mean glandular breast dose as the breast phantom images (2.2mGy). It can be seen that the detectors have similar values of DQE(f) up to about 2lp/mm. Above 2lp/mm

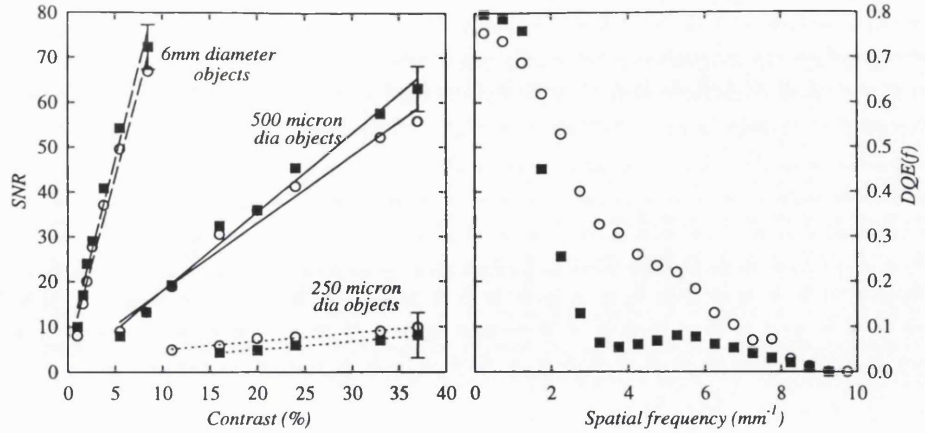

Figure 5.18 comparison of dSNR results and DQE(f) results. Black squares correspond to detector dc120C white circles correspond to detector fo130C.

detector fo130C has greater values of DQE(f). These higher values of DQE(f) may go some way to explaining why detector fo130C produces images with higher values of dSNR for the smallest 250μm objects. The relationship between DQE(f) and the values of dSNR is illustrated more deeply in the next section.

Both detectors have similar configurations but the biggest difference between the two is that detector dc120C has no fibre optic coupling and the phosphor layer is deposited directly upon the CCD. These results show that for objects greater than or equal to 500μm in diameter there is no discernible advantage gained by using a fibre optic coupling in the detector. However for objects below 250μm in diameter it is necessary to use a fibre optic coupling to shield the CCD from direct interactions of x-rays.

Figure 5.19 shows DQE(f) and dSNR measurements for detectors fohama and dc120C. It can be seen that detector dc120C produces images with higher dSNR for the 6mm and 500μm diameter objects compared to detector fohama. This can be attributed to the fact that detector dc120C has a higher quantum detection efficiency (more x-rays contributing to the final image) than detector fo130C.
Detector fohama produces images with higher dSNR for the 250μm diameter objects and can detect more (7 details as opposed to 5 for detector dc120C). This result can be

attributed to the fact that fohama has a higher spatial resolving capability compared to detector dc120C.

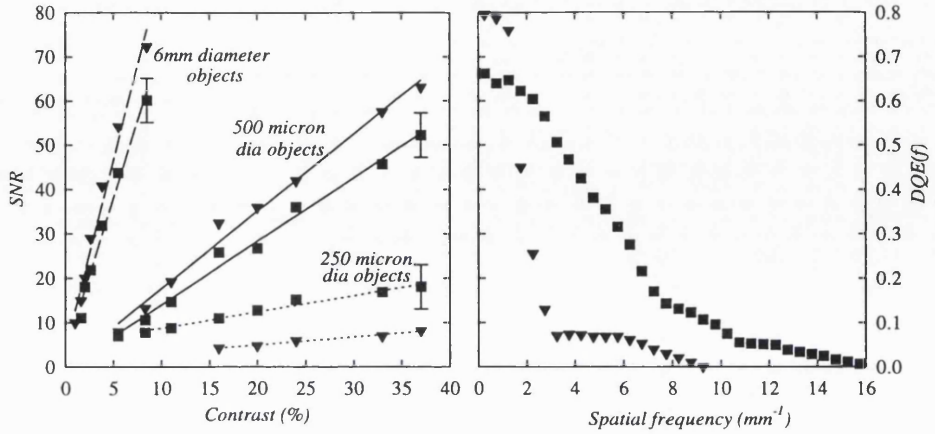

Figure 5.19 comparison of dSNR results and DQE(f) results. Black squares correspond to detector fohama, black triangles correspond to detector dc120C.

Comparing results from dSNR and DQE(f) measurements it may be inferred that-

1.The drop off in DQE(f) above 2lp/mm for detector dc120C inhibits the detectors ability to produce images with high dSNR for the 250μm diameter objects or alternatively high values of DQE(f) above 2lp/mm are necessary to enable detection of 250μm diameter objects (for a mean glandular breast dose of 2.2mGy).

2. DQE(f) values between 0 and 2lp/mm are important for detecting large objects (6mm in diameter).

5.3.9 Comparison with film-screen system

An image of the Leeds TORMAX breast phantom was obtained under standard conditions used in mammography equipment quality assurance testing. The system used was a Siemens Mammomat III unit used in current clinical practice at University College Hospital. A Kodak Min-R2 screen -MRE film combination was used under automatic exposure control (AEC) with a 28kVp Mo/Mo beam to produce a mean glandular breast dose of 1.4mGy.

Quantitative measurements of dSNR were unable to be performed upon the film image, however the number of objects visible upon the film was used to subjectively "score" the image obtained. Table 5.3 shows the scores obtained for the film-screen combination together with 3 CCD based detectors. Errors on these scores are high (estimated at 15%).

Table 5.3 Number of details visible for film screen system and detectors.

	Film screen	*fohama*	*dc120C*	*fo50G*
No. of 6mm diameter objects detected	6	6	7	3
No. of 500μm diameter objects detected	7	7	7	4
No. of 250μm diameter objects detected	5	7	5	3
Mean glandular breast dose (mGy)	1.4	2.2	2.2	2.2

5.3.10 Discussion of results obtained with film/screen system

The film-screen system was able to detect contrasts down to 1.6%, 5.4% and 16% for the 6mm ,500μm and 250μm diameter objects respectively for a dose of 1.4mGy. Results show that

1. Detector dc120C performed just as well if not better than the film-screen combination in detecting all size of objects for a dose of 2.2 mGy.
2. Detector fohama was able to detect 250μm size objects down to 5.4% in contrast.
3. Detector fo50G was only able to detect contrasts down to 3.8%, 20%and 24% for the 6mm, 500μm and 250μm diameter objects.

It is noted that the comparison between results obtained with the screen-film system and the CCD based detectors is not strictly valid because they were obtained for different doses. However, because the image was obtained with AEC (automatic exposure control), it is possible that the scores for the film-screen combination would not change if the dose was increased and these scores represent the 'best' that the film-screen system will ever do.

These results show that for a small increase in mean glandular breast dose the prototype digital mammography system(with detectors fohama and dc120C) performs as well as film-screen combination for detecting large objects (6mm) and performs better at detecting small objects (250μm). Improvements to the system could go some way to producing similar scores for a lower dose comparable with the film-screen combination.

5.4 Improving detector configuration

Results of image quality / detectabilty measurements from previous sections have shown a relationship between high DQE(f) values and SNR. From these results it can be seen that it is necessary to maximise DQE(f) at high spatial frequencies (above 2lp/mm) in order to produce images with high values of SNR for small objects (250 μm in diameter and smaller). Methods of increasing DQE(f) are discussed in chapter 4 and they are summarised below:

- Reducing the dark current noise $W_D(f)$, by further cooling the CCD.
- Increasing $W_Q(f)$. This can be achieved by increasing the gain in the number of optical quanta produced per incident x-ray and increasing the optical transmission efficiency of any fibre optic couplings used.
- Producing higher MTF values.
- Increasing the quantum detection efficiency A_Q.
- Eliminating direct hits in the CCD

A detector configuration can be specified based upon these prescriptions, the specifications are given below.

- detector cooling.

The 15_11 CCD was cooled to 20°C a further reduction in temperature to 5 °C would produce a factor ~2 reduction in dark current production and $2^{0.5}$ reduction in noise without the need for a 'dry' system (a dry system refers to a system which is purged with dry nitrogen to remove any water vapour that is present).

- Intagliated fibre optics

MTF and sensitivity results for detector fohama have shown that by using intagliated fibre optics together with a reflective coating one can increase light output without any degradation in MTF and eliminate direct hits in the CCD. By using a thicker phosphor layer the x-ray quantum efficiency will be increased there by increasing DQE(f). Figure 5.20 shows theoretical DQE(f) curves obtained from Westmore and Cunningham's model (chapter 4), for thickness' ranging from 80 to 120μm for a detector similar to fohama.

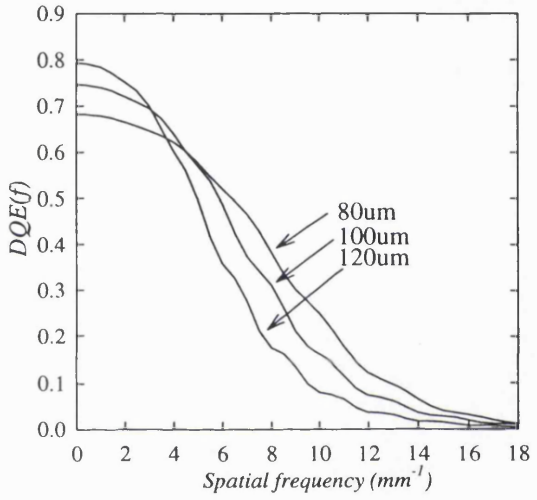

Figure 5.20 DQE(f) curves for detector fohama with 80μm, 100μm and 120μm phosphor thickness'.

It can be seen that phosphors of thickness 100μm and 120μm give rise to an 11% and 17% increase in DQE(f) respectively at zero spatial frequency compared to a phosphor thickness of 80μm (for 28kVp Mo:Mo beam). However at higher spatial frequencies, which have been shown to be important for detecting small objects, DQE(f) is lower for the 100μm and 120μm thickness. For the 100μm thickness, DQE(f) is lower compared to the 80μm curve for frequencies greater then ~5.5lp/mm. It is felt that the optimum phosphor thickness is around 100μm, the higher DQE(f) values at low spatial frequencies obtained with the 100μm thick phosphor will increase the probability of detection of large low contrast objects for a set dose and the DQE(f) is lower for relatively high spatial frequencies. Results presented relate to theoretical models, further

work is needed to quantify the change in imaging performance as the phosphor thickness is increased to 100μm.

Figure 5.21 shows DQE curves for fibre optics with fibre diameters 10 μm 20μm and 40μm with a 1μm cladding. Increasing fibre diameter gives an increase in the transmission efficiency because the packing fraction is increased. A faceplate with 20μm diameter fibres and 1μm cladding has associated with it a 82% compared with a 75% transmission efficiency for 10μm fibres. It can be seen that by increasing the fibre optic fibre diameter to 20μm from 10μm there is only a small degrading effect upon DQE at high spatial frequencies <10lp/mm. Only when the fibre diameter becomes larger than the CCD pixel size is there any appreciable degradation (see curve for 40μm diameter fibre).

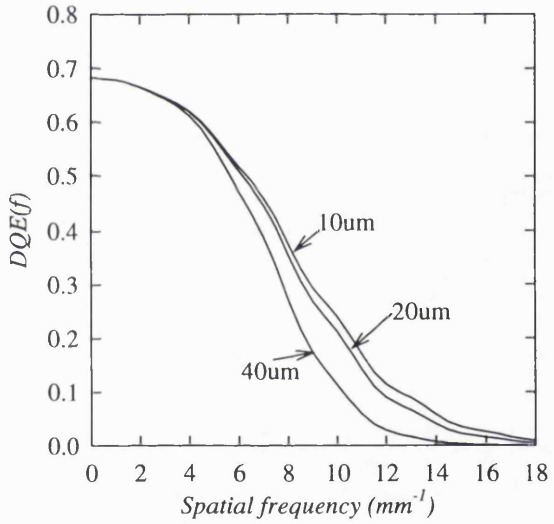

Figure 5.21 DQE(f) curves for detector fohama with 10μm, 20μm and 40μm fibre diameters

- Pixel size

As one goes to smaller pixel dimensions there is an increased burden upon system performance in order to maintain factors such as imaging times, computer memory requirements and display requirements. Figure 5.22 shows DQE(f) curves for pixel sizes ranging from 1μm to 100μm for a detector similar to fohama with 80μm of CsI(Tl).

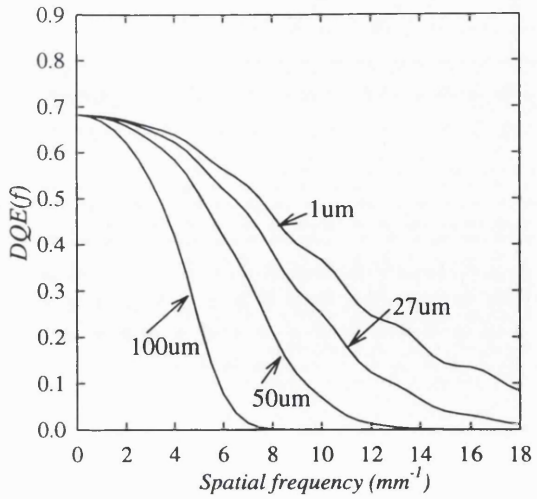

Figure 5.22 DQE(f) curves for detector fohama with 1μm, 27μm and 50μm fand 100μm pixel sizes

The degradation in MTF due to pixel size is small for a pixel size of 1μm. It can be seen as the pixel size is increased the DQE(f) drops off more rapidly at higher spatial frequencies and is reduced by 50% at 4lp/mm for the 100μm pixel size. It is felt that the optimum pixel size is in the range 25-50μm. It is noted that with 25μm pixels the exists an opportunity to sum pixels 'on chip', if necessary to provide larger pixel sizes.

5.5 Conclusions

A Monte Carlo simulation of the mammography system has shown how the optimum x-ray energy for a given size breast can be determined. Results show that for the average breast thickness x-ray energy of around 20keV is required which matches closely the characteristic x-ray energy produced from a molybdenum x-ray target.

A prototype digital mammography system was set up to compare image quality obtained with various detector configurations. Scatter rejection using slot beam collimation was demonstrated.

The Leeds TORMAX breast phantom was used to obtain images of various details under set exposure conditions for a number of detectors. Quantitative evaluation of the

images in terms of dSNR has been described. Values of dSNR were found to vary with the square root of the breast dose and linearly with the detail contrast as expected for quantum noise limited systems.

A comparison between the values of dSNR obtained for each detector shows that in general detectors with the highest values of DQE(f) at low spatial frequency (equivalent to the quantum detection efficiency A_Q) give images with the highest values of dSNR for the 6mm diameter objects. Detector dc120C produces highest value of dSNR for the 6mm object. For the 500μm diameter objects, again detector dc120C produces images with the highest values of dSNR. However for the 250μm diameter object detector fohama produces images with the highest dSNR. There seems to be some correlation between the values of DQE(f) and dSNR and it is asserted that high values of DQE(f) above 2lp/mm are necessary to produce high values of dSNR for the 250μm diameter objects.

A subjective comparison with a film-screen combination has shown that, for a small increase in dose, the digital mammography system can perform as well as the film screen combination for large diameter objects and perform better for small (250μm diameter) objects. With improvements to the system it will be possible to lower the increase in dose or alternatively produce higher quality images for the same dose.

System and detector design have been discussed and optimum values for phosphor thickness, fibre diameter and pixel size have been presented.

CHAPTER 6

6. CCD based Microtomography (μCT) system.

Microtomography (μCT) enables the visualisation of 2-D slices through a specimen with high spatial resolution. This procedure has high potential for inspecting the size and structure of breast lumpectomy specimens and as a tool for non invasive testing. Previously designed microtomography systems use an x-ray image intensifier (XRII) as the detector system. XRII systems have a relatively poor spatial resolving capability. This is overcome by using a micro-focal spot tube with the XRII, which allows very large magnifications to be used (Machin and Webb 1994) as shown in Figure 6.1

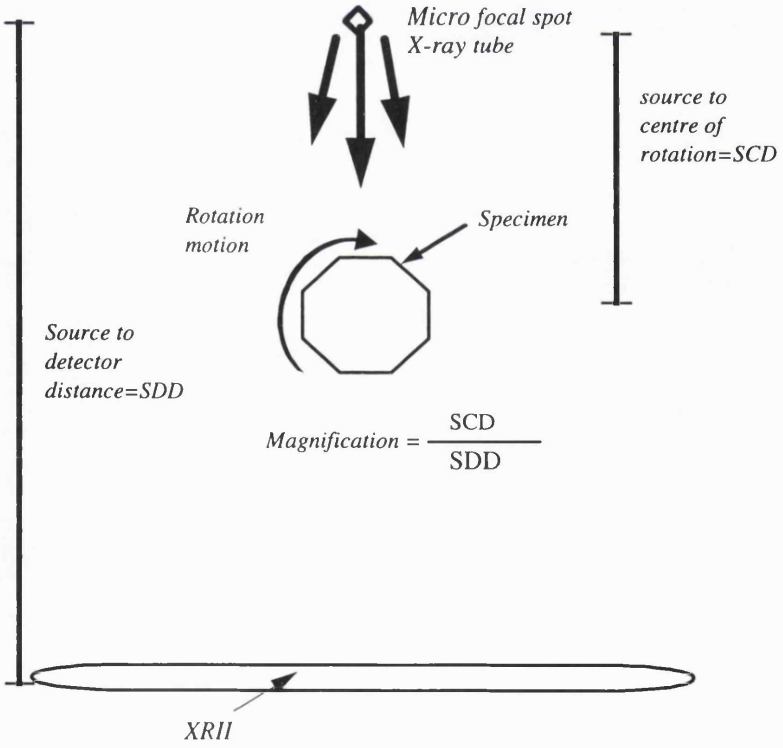

Figure 6.1 Conventional μCT system

A CCD based μCT system was constructed at UCL. Advantages over the previous μCT systems are primarily concerned with the fact that there is no need to use a micro focal spot tube in the system and are summarised below.

- Good inherent detector resolution associated with the CCD, means that there is no need for large magnifications to achieve good spatial resolution.
- with micro focal spot x-ray tubes the beam current available is usually quite low so that there is a limited x-ray flux available. This problem can be overcome by summing consecutive frames from the XRII but at the expense of imaging time.
- With the CCD based system (using the ~400μm focal spot size) the magnification is made equal to 1.0 i.e, x-ray tube is moved a large distance from the object so that it is possible to assume parallel beam geometry, this reduces the complexity of the reconstruction algorithm and reduces the time taken to reconstruct the image.

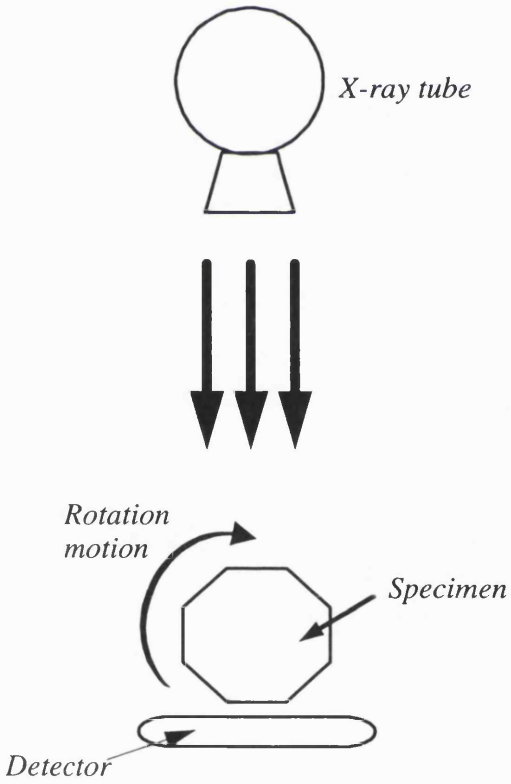

Figure 6.2 diagram of CCD based μCT system.

6.1.1 Image Acquisition and reconstruction

Figure 6.2 shows a diagram of the CCD based μCT system, it consists of a Siemens Mammommat I system and the CCD based x-ray imaging system fitted with detector fohama described in chapter 2. The detector is placed at 100cm away from the focal spot of the tube and the rotating specimen stage is placed very close to the detector. The maximum object size that can be imaged is around 27mm and is limited by the size of the detector.

For each data-set an image of the specimen is obtained for all projection angles between 0 and 180 degrees. A 'flat' or 'open' image, without the specimen present, is also obtained. Figure 6.3 shows a full data-set obtained for '8 wire' computer ribbon cable for 45 projections with an angular spacing of 4.0 degrees.

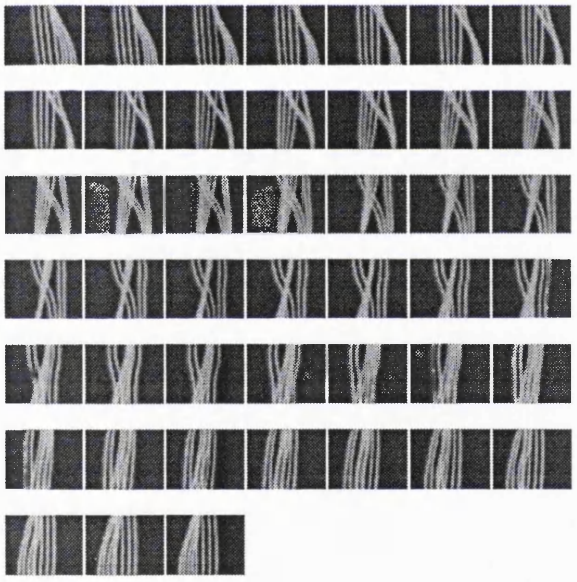

Figure 6.3 CT data-set comprising 45 images of computer ribbon cable, spacing between each wire is ~0.5mm

Once a 'raw data' set has been acquired it is corrected for gain and offset fluctuations as described in chapter 3.

6.1.2 Reconstruction algorithm

A computer program obtained from the University of Southern Carolina was used to reconstruct the image. The program uses a parallel beam filtered back-projection technique. The program was originally designed for single photon emission tomography and as such was only able to process images of dimensions 128×128 pixels. This meant that all the images obtained had to be re-sampled from 1024×256 to the required resolution before reconstructing. This was done by cropping the image to form a square (256×256) image and then averaging pixels to reduce the spatial resolution and the image size by a factor of 2.

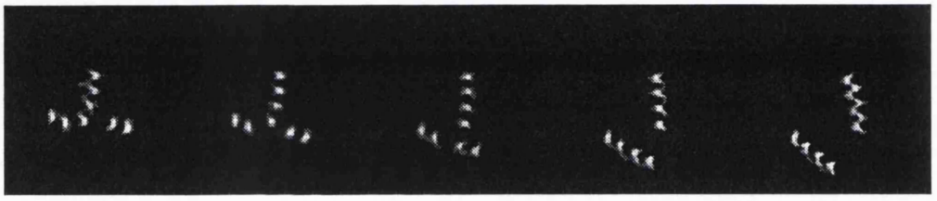

Figure 6.4 5 reconstructed images of computer ribbon cable.

Figure 6.4 show a set of 5 reconstructed images of the ribbon cable taken at various heights in the detector. The wire cores of the ribbon cable and the plastic coatings are resolved. Each wire (~500μm in diameter) corresponds to 8 pixels in the image giving pixels of around 62μm in width and height.

6.2 Conclusions and discussion

A CCD based μCT system has been constructed at UCL. Advantages over μCT systems have been discussed above. The system is capable of producing 2-D transaxial slices of objects up to 27mm wide. Images produced by the system indicate pixel sizes of around 60μm are obtained.

The use of specially written reconstruction routines for filtered backprojection should overcome the problem of resampling currently encountered giving pixel-size and limiting spatial resolution measurements for the system identical to those described in chapter 4.

Higher spatial resolutions can be obtained by using the CCD based μCT system together with a micro-focal spot tube. Work under progress at Surrey university uses a CCD system similar to the one described previously, with a micro focal spot tube (~10μm focal spot size). This allows object magnification to be used to increase spatial resolution further.

CHAPTER 7

7. CONCLUSIONS

The design, testing and evaluation of a CCD based digital imaging system has been discussed in this thesis. The application of the system for digital mammography was discussed in chapter 5. Subjective analysis of images shows that the system can out perform standard screen film systems in terms of object detection for a small increase in dose. Further improvements to the system discussed in chapter 4 will act to try to produce the same image quality for equivalent doses used in conventional mammography.

A relationship between DQE(f) and image quality has been presented. It was found that detectors with high DQE(f) values above 2lp/mm have an increased probability of detecting objects of 250μm in diameter. Methods of increasing DQE(f) are discussed in chapter 5 together with a description of system design.

Direct hits in the CCD has been shown to increase MTF response at high spatial frequencies However the noise contributions from direct hits for directly coated detectors have been shown to reduce DQE(f). This reduction in DQE(f) has the effect of reducing the detectors ability to detect small objects. The use of fibre optic coupling between the phosphor screen and the CCD has been shown to remove direct hits in the CCD.

A prescription for improving the detector design is discussed in chapter 5 and involves increasing DQE(f).Methods of increasing DQE(f) are discussed in chapter 4.

The use of intagliated fibre optics have shown advantages over using conventional intensifying screens. Optimum phosphor thickness, CCD pixel size and fibre diameter are discussed in chapter 5.

The use of CCDs for digital mammography still presents a few fundamental limitations such as their relatively small size and the need to eliminate direct hits. The replacement of CCDs with a hydrogenated amorphous silicon (a-Si:H) detector may overcome these limitations. When starting this research there were a number of problems associated with (a-Si:H) detectors including the large pixel sizes ~100μm and poor pixel fill factor. Recent developments in amorphous silicon detector technology at Surrey University have led to the production of a-Si:H arrays with 100% fill factor and with the possibility of producing pixels down to 35μm in width. These detectors can also be produced in large panel arrays sufficient to cover the whole area of interest in mammography or the area necessary to cover the scanning slot in a scanning system.

Another advantage is that these detectors use a layer of amorphous silicon only ~1μm thick and can achieve optical quantum efficiencies of around 100% greater compared to 10μm of crystalline silicon (as a consequence of the direct band gap associated with a-Si:H)(see Street 1990). Another consequence is the probability of a direct hit is reduced with these detectors so that there may be no need for a fibre optic coupling between the phosphor screen and the detector. This would increase the effective DQE(f) for these devices.

The effects of readout noise and other noise sources needs to be fully quantified for these detectors, however there is no doubting the great potential for the use of a-Si:H detectors for the replacement of CCDs in a digital mammography system.

Microtomography has great potential for providing diagnostic information from breast lesions and for use as a non destructive testing tool. The use of the system for microtomography and its advantages are discussed in chapter 6. This work is being

continued at Surrey University where a similar CCD based system coupled with a micro-focal spot x-ray tube can produce images with 10μm spatial resolution

The following table is a summary of the results obtained for phantom measurements

Table 7.1 Summary of results obtained with phantom measurements

Detector id.	*Quantum detection efficiency*	*SNR of 8.5 % contrast, 6mm dia. detail*	*SNR of 33% contrast, 500μm dia. detail*	*SNR of 33% contrast, 250μm dia. detail*
dc120C	0.84	72	58	6.5
fo130C	0.86	68	52	9.0
fo70C	0.68	55	42	13
foMinR	0.79	42	26	5.3
fohama	0.72	60	49	17
fo50G	0.80	40	31	11.
ft130C	0.86	65	47	7.8
ft70C	0.68	50	35	6.0

APPENDIX 1

APPENDIX 1.Calculation of CCD quantum efficiency

The spectrum weighted quantum efficiency of the CCD can be calculated using the following equation where $\eta_{ccd}(\lambda)$ is the CCD spectral response at wavelength λ and $\phi_{phos}(\lambda)$ is the normalised emission spectrum for the phosphor at wavelength λ.

$$\overline{\eta_{ccd}} = \frac{\sum_{\lambda} \eta_{ccd}(\lambda)\phi_{phos}(\lambda}{\sum_{\lambda} \phi_{phos}(\lambda)}$$

Shown in Figure 1 is a plot of spectral response of a 15_11 CCD together with emission spectra of CsI(Tl) and $GdO_2S_2(Tb)$ (Knoll 1989).

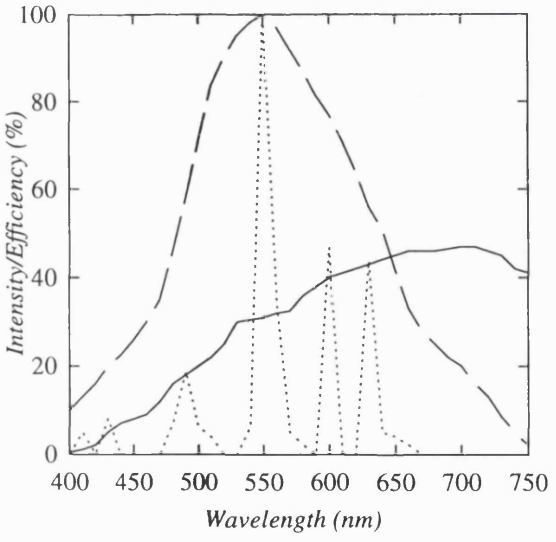

Figure 1 solid line is the spectral response of 15_11 CCD, dashed line is the emission spectrum of CsI(Tl) and dotted line is the emission spectrum of $GdO_2S_2(Tb)$.

To maximise the sensitivity of phosphor coupled CCDs it is necessary to match the maximum output of the phosphor to the maximum spectral response of the CCD. From Figure 1 it can be seen that the spectral response of the CCD has a maximum of around 45% at 700nm, CsI(Tl) has a broad emission spectrum which peaks at around 550nm. Using the above equation a value for the spectrum weighted quantum efficiency of the device was calculated $\eta_{ccd} = 0.31$.

The emission spectrum of $GdO_2S_2(Tb)$ is made up of a number of narrow 'spikes' the largest of which is at 550nm. A figure of $\eta_{ccd} = 0.32$ was obtained using the above equation for $GdO_2S_2(Tb)$.

APPENDIX 2

APPENDIX 2 Calculation of incident x-ray flux per exposure

The average no. of incident x-rays per unit exposure per unit area N_X is calculated using the equation given below, where $\Phi_x(E)$ is the normalised x-ray photon fluence at energy E, kV_p is the kilovoltage peak of the x-ray beam and C(E) is the photon fluence to kerma in air conversion factor at energy E (Johns and Cunningham, 1983). Fig1shows a plot of 1/C(E) in the energy range 0 to 28 keV, from Birch et al (1979).

$$N_x = 1 \Big/ \int_0^{kVp} C(E)\Phi_x(E)dE$$

For example, the average no of x-rays per Rontgen per mm^2 for typical exposure conditions (28kVp Mo tube 39μm Mo filtration) used with the CCD system was

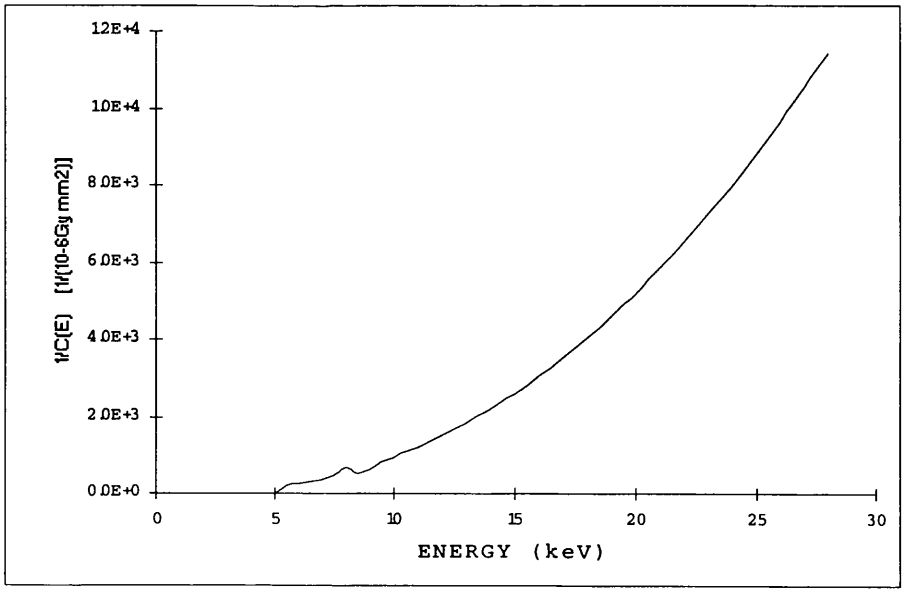

Figure 1 Air kerma to photon fluence conversion factors as a function of x-ray energy.

$(38.0\pm.4)\times10^6$ photons/R/mm^2. For the 15_11 CCD with 27μm×27μm pixels this is equivalent to 27709±166.5 photons/R/pixel.

REFERENCES

Adinolfi,M; Angelini,C (1992): Progress on high resolution tracking with scintillating fibres:a new detector based on capillaries filled with liquid scintillator. Nucl. Instr. and Meth. A315, 177-181.

G T Barnes; I A Brezovich (1978): The intensity of scattered radiation in mammography. Radiology 126, 243-247.

Barnes G; Brezovich I (1978): The Intensity of Scattered radiatio in mammography. Radiology 126, 243-247.

Barnes G; Chakraborty D (1982): Radiographic Mottle and patient exposure in mammography. Radiology 145, 815-821.

Barrett H; Swindell W (1981): Radiological Imaging. Vol. 1&2. Academic Press, New York.

W Bebcivelli; E Bertolucci; U Bottigli; A Del Guerra; W Nelson (1991): Use of EGS4 for the evaluation of the performance of a silicon detector for x-ray digital radiography. Nucl. Instr. and Meth. A305, 574-580.

Benyon J.; Lamb D.(1980): Charge coupled devices and their applications. McGraw-Hill, Maidenhead.

Biberman L (Ed) Recent phsycophysical experiments and the display signal to noise ratio concept. Perception of displayed information. Plenum, New York.

R Birch; Marshall M; Ardran G M (1979): Catalogue of spectral data for diagnostic x-rays. The Hospital Physicists Association, London.

Burke,B (1991): Dynamic suppression of Interface-state dark current in buried channel CCDs. IEE Transactions on electron devices 38(2), 285.

Chakraborty D P; Eckbert M P (1995): Quantitative verses subjective evaluation of mammography accrediation phantom images. Med. Phys. 22, 133-144.

Court,L(1995) Design and optimisation of a CCD based digital mammography system PhD Thesis, University of London.

Court,L; Ho,I (1994): Design and optimisation of a digital radiographic system with emphasis on TDI CCD scanning mammography. SPIE Phys. of Med. Imag. 2163, 1024.

Cowen A R; Coleman J; Workman A (1989): Leeds mammographic test objects instrction manual. The Radiological Imaging Group, Leeds.

Cunningham,I,A (1987): A method for MTF determination from edge profiles with correction for finite element differentiation. Med. Phys. 14(4), 533-537.

Cunningham,I,A; Reid,B,K (1992): Signal and noise in modulation transfer function determinations using the slit,wire and edge techniques. Med. Phys. 19(4), 1037.

Cunningham,I,A; Westmore,M,S (1994): A spatial frequency dependent quantum accounting diagram and detective quantum efficiency model of signal and noise propagation in cascaded imaging systems. Med. Phys. 21 Pre-print, .

Cunningham,I,A; Westmore,M,S (1994): Visual impact of the non-zero spatial frequency quantum sink. SPIE Phys. of Med. Imag. 2163, 274-283.

Dainty J C; Shaw R (1974): Image Science. Academic Press, Maidenhead.

Dance,D; Day,G (1984): The computation of scatter in mammography by Monte Carlo methods. Phys. Med. Biol. 29(3), 237-247.

Dance D R (1980): The Monte Carlo calculation of integral radiation dose in xeromammography. Phys. Med. Biol. 25, 25-37.

Dance D R (1990): Monte Carlo calculation of conversion factors for the estimation of mean breast dose. Phys. Med. Biol. 9, 1211-1219.

Dance D R (1994): Radiographic films and screens Medical radiation detectors. IOP Publishing, Bristol.

Dance D R; Day G J (Eds.) (1981): Simmulation of mammography by Monte Carlo calculation-Proceedings on patient exposure to radiation in medical x-ray diagnosis-possibilities for dose reduction. Commission of the European Communities, Luxembourg.

Dick C; Motz,J (1981): Image information transfer properties of x-ray fluorescent screens. Med. Phys. 8(3), 337-346.

EEV Ltd (1993): CCD1511 Series Scientific Image Sensor. EEV Ltd, Chelmsford, Essex.

EEV Ltd (1993): CCD0206 Series Scientific Image Sensor. EEV Ltd, Chelmsford, Essex.

Fahrig,R; Maidment,D,A; Yaffe,M,J (1992): Optimization of peak kilovoltage and spectral shape for digital mammography. SPIE Phys. of Med. Imag. 1651, 74-83.

Fitzgerald M; Dance D; Fisher K; Lawlinski C; Ramsdale M (1989): The commissioning and routine testing of mammographic x-ray systems. 2nd Ed. ed. Institute of Physical Sciences in Medicine Report 59, .

Forrest P (1987): Breast Cancer screening: report to the Ministers of Health of England,Wales,Scotland and Northern Ireland. HMSO, .

Fu,T,y; Roehrig,H (1984): Noise power spectrum, MTF and DQE of photoelectronic radiographic systems. SPIE Application of optical instrumentation in medicine 454, 377.

Fujita,H (1992): A simple method for determining the modulation transfer function in digital mammography. IEEE Trans. Med. Imag. 11(1), 34-39.

Fujita,H; Doi,K (1985): MTFs of II-TV digital imaging systems. Med. Phys. 12(6), 713.

Giger,M,L (1984): Modulation Transfer function. Med. Phys. 11(3), 287.

Giger,M,L; Doi,K (1984): Noise Wiener Spectrum. Med. Phys. 11(6), 797.

Giger M; Doi K; Fujita H (1986): Noise Wiener spectra of II-TV digital imaging systems. Med. Phys. 13, 131-138.

Goldman,L,W (1992): Fluoroscopic performance tests using a portable computer/frame grabber: Wiener spectra measurements. Med. Phys. 19(1), 45.

Hammerstein G et al. (1979): Absorbed radiation dose in mammography. Radiology 130, 485-491.

Holdsworth D; Gerson R; Fenster A (1990): A time delay integration charge coupled device camera for slot scanned digital radiography. Med. Phys. 17, 876.

Hopkinson G (1983): Charge diffusion effects in CCD x-ray detectors 1: theory. Nucl. Instr. and Meth. 216, 423-429.

Hopkinson G (1987): Analytical modelling of charge diffusion effects in CCD imagers. Opt. Eng. 26, 766-772.

Ito,M (1987): CsI(Na) Scintillation plate with high spatial resolution. IEEE Transactions on Nuclear science NS34 No1., 401.

Janesick J; Elliot T; Collins S (1987): Charge coupled device advances for x-ray scientific applications. Opt. Eng. 26, 156-166.

Jiang Y; Nishikawa R; Giger M; Doi K; Schmidt R; Vyborny C (1992): Method of extracting signal area and signal thickness of microcalcifications from digital mammograms. SPIE Phys. of Med. Imag. 1778, 28-38.

Johns,P,C; Yaffe,M,J (1985): Theoretical optimization of dual energy x-ray imaging with application to mammography. Med. Phys. 12(3), 289.

Johns H; Cunningham J (1983): The physics of radiology. 4th Ed. ed. Charles C Thomas, Illinois.

Knoll G (1989): Radiation detection and measurement. 2nd Ed ed. John Wiley, New York.

Lefebvre F; Benali H; Gilles R; Kahn E; Paola R (1995): A fractal approach to the segmentation of microcalcifications in digital mammograms. Med. Phys. 22, 381-390.

Liu,H; Karrelas,A (1992): Optical properties of fiber tapers and their impact on the performance of a fiber optically coupled CCD x-ray imaging system. SPIE Phys. of Med. Imag. 1894, 136.

K Machin; S Webb (1994): Cone -beam x-ray microtomography of small specimens. Phys. Med. Biol. 39, 1639-1657.

Maidment,A,D; Yaffe,M,J (1993): Imaging performance of a prototype scanned slot digital mammography system. SPIE Phys. of Med. Imag. 1896, 93.

Maidment,A,D; Yaffe,M,J (1994): Analysis of the spatial frequency dependent DQE of optically coupled digital mammography detectors. Med. Phys. 21(6), 721.

Maidment A; Fahrig R; Yaffe M (1993): Dynamic range requirements in digital mammography. Med. Phys. 20, 1621-1633.

Maidment A; Yaffe M (1990): Scanned slot digital mammography. SPIE Phys. of Med. Imag. 1231, 316-326.

Marchand,E,W (1964): From line to point spread function: The general case. J. Opt. Soc. Am 54,915, 352.

Martinez-Davalos A (1994): An investigation of the imaging performance of new digital x-ray detectors. Ph.D. Dissertation, The University of London.

Metz C; Wagner R; Doi K; Brown D; Nishikawa R; Myers K (1995): Toward consensus of quantitative assessment of medical imaging systems. Med. Phys. 22, 1057-1061.

Mills R; Path M; Davis R; Stacey A (1976): The detection and significance of calcifications in the breast: a radiological and pathological study. BJR 49, 12-26.

Motz,J,W; Danos,M (1978): Image information content and patient exposure. Med. Phys. 5(1), 8.

Motz J; Danos M (1978): Image information content and patient exposure. Med. Phys. 5, 8-22.

Nelson W; Rodgers D; Hirayama H (1985): The EGS4 code system. Stanford Linear Accelerator Center Report SLAC-265, .

Nishikawa,R,M; Yaffe,M,J (1985): signal to noise properties of mammographic film screen systems. Med. Phys. 12(1), 32.

Nishikawa,R,M; Yaffe,M,J (1987): Scanned-projection digital mammography. Med. Phys. 14(5), 717.

Nishikawa,R,M; Yaffe,M,J (1990): Model of the spatial frequency dependent detective quantum efficiency of phosphor screens. Med. Phys. 17(5), 894.

Nishikawa,R,M; Yaffe,M,J (1990): Effect of various noise sources on the detective quantum efficiency of phosphor screens. Med. Phys. 17(5), 887.

Nishikawa R; Jiang Y; Giger M; Doi K; Schmidt R; Vyborny C; Zhang W; Ema T; Papaioannou J; Wolverton D; Bick U; Nagel R; Mao Y (1994): Performance of automated CAD schemes for the detection and classification of clustered microcalcifications. Presented at the Second International Workshop on Digital Mammography, York U.K.

Nishikawa R; Yaffe,M (1989): Effect of finite phosphor thickness on detective quantum efficiency. Med. Phys. 16(5), 773-780.

Rabbani,M; Shaw,R (1987): Detective quantum efficiency of imaging systems with amplifyng and scattering mechanisms. J. Opt. Soc. Am 4(5), 895.

Reichenbach,S,E; Park,S,K (1991): Characterising digital image acquisition devices. Opt. Eng. 30(2), 170.

Rose,A (1971): Vision:Human and Electronic. Plenum, New York.

Rowlands J; Taylor,K (1983): Absorption and noise in Caesium iodide x-ray image intensifiers. Med. Phys. 10(6), 786-795.

Saks,N,S (1980): A technique for suppressing dark current generated by interface states in buried channel CCD imagers. IEE Transactions on electron devices edl1(7), 131.

Shao,H; Miller,D,W (1991): Scintillating fibre optics and their applications in radiographic systems. IEEE Transactions on Nuclear science 38(2), 845.

Sickles E (1986): Breast Calcifications: Mammographic evaluation. Radiology 160, 289-293.

Sones,R,A (1984): A method to measure the MTF of digital x-ray systems. Med. Phys. 11(2), 166.

Stevels,A,L (1974): Vapour-deposited CsI:Na layers,II screens for application in x-ray imaging devices. Philips j. Res. 29, 363-382.

R.A. Street (1991): Hydrogenated amourphous silicon. Cambridge University Press, Cambridge.

Sturm R; Morgan R (1949): Screen intensification systems and their limitations. The American journal of Roentgenology and radium therapy 5, 617-635.

Suckling J; Dance,D; Moskovic E; Lewis,D; Blacker,S (1995): Segmentation of mammograms using multiple linked self-organising neural networks. Med. Phys. 22, 145-152.

Swank,R,K (1973): Absorption and noise in x-ray phosphors. J. App. Phys 44(9), 4199.

Swank,R,K (1973): Calculation of modulation transfer functions of X-ray fluorescent screens. Applied optics 12(8), 1865.

Tapiovaara,M; Wagner,R,F (1985): SNR and DQE analysis of broad spectrum x-ray imaging. Phys. Med. Biol. 30(6), 519.

Torren,J; Bisschop,J (1994): Complete characterisation of dark current in frame transfer image sensors. Philips j. Res. 48, 207-231.

Zeman,H,D (1993): High accuracy X-ray imaging: screen, lens and CCD. SPIE Phys. of Med. Imag. 1896, 225.